University of Alberta

The Numerical Identification of the fMRI Hemodynamic Response Using ICA

by

Todd John Michael Penney ©

A thesis submitted to the Faculty of Graduate Studies and Research
in partial fulfillment of the requirements for the degree of

Master of Science

Department of Electrical and Computer Engineering

Department of Biomedical Engineering

Edmonton, Alberta
Fall 2008

Library and
Archives Canada

Published Heritage
Branch

395 Wellington Street
Ottawa ON K1A 0N4
Canada

Bibliothèque et
Archives Canada

Direction du
Patrimoine de l'édition

395, rue Wellington
Ottawa ON K1A 0N4
Canada

Your file Votre référence
ISBN: 978-0-494-47388-7
Our file Notre référence
ISBN: 978-0-494-47388-7

NOTICE:
The author has granted a non-exclusive license allowing Library and Archives Canada to reproduce, publish, archive, preserve, conserve, communicate to the public by telecommunication or on the Internet, loan, distribute and sell theses worldwide, for commercial or non-commercial purposes, in microform, paper, electronic and/or any other formats.

The author retains copyright ownership and moral rights in this thesis. Neither the thesis nor substantial extracts from it may be printed or otherwise reproduced without the author's permission.

AVIS:
L'auteur a accordé une licence non exclusive permettant à la Bibliothèque et Archives Canada de reproduire, publier, archiver, sauvegarder, conserver, transmettre au public par télécommunication ou par l'Internet, prêter, distribuer et vendre des thèses partout dans le monde, à des fins commerciales ou autres, sur support microforme, papier, électronique et/ou autres formats.

L'auteur conserve la propriété du droit d'auteur et des droits moraux qui protège cette thèse. Ni la thèse ni des extraits substantiels de celle-ci ne doivent être imprimés ou autrement reproduits sans son autorisation.

In compliance with the Canadian Privacy Act some supporting forms may have been removed from this thesis.

While these forms may be included in the document page count, their removal does not represent any loss of content from the thesis.

Conformément à la loi canadienne sur la protection de la vie privée, quelques formulaires secondaires ont été enlevés de cette thèse.

Bien que ces formulaires aient inclus dans la pagination, il n'y aura aucun contenu manquant.

Canada

Abstract

In this work, electroencephalography and functional magnetic resonance imaging (fMRI) were performed together to obtain electroencephalograms (EEGs) and fMR images from an epileptic patient. A procedure known as independent component analysis (ICA) was applied to the fMR images in order to develop an improved method of identifying brain regions where the patient's seizures occur.

Before the EEG-fMRI study was performed, a preliminary fMRI scan was performed on a healthy subject. The fMR images acquired from the preliminary scan were used to explore the effectiveness of applying ICA to fMR images.

The results from both studies indicate that more work needs to be done to improve the quality of hemodynamic response signal models used for statistically testing fMRI measurements. However, the results also indicate that ICA is an effective tool that can be used to help identify epileptogenic regions of a patient's brain.

Acknowledgments

I would like to thank my primary supervisor Dr. Zoltan Koles for his support and encouragement on this project. He provided a lot of helpful advice and allowed me the freedom to take a lot of ownership over the project. He also provided the opportunity for me to attend some interesting conferences to present my work. For those opportunities, I am very grateful.

I would like to thank my co-supervisor Dr. Alan Wilman, who provided encouraging advice and assistance with imaging concepts I needed help understanding.

I would like to thank the members of the Koles Lab for their advice and encouragement throughout the project. It was great to share my days with them and to work with them in a friendly environment. These people are Michael Cook, John Russell, Natasha Kuzbik, Aisha Yahya and Dr. Daniel Withey.

I would like to thank the fMRI group at the Seaman Family Magnetic Resonance Imaging Centre at the Foothills Hospital in Calgary, Alberta, Canada. This imaging group is affiliated with the University of Calgary. Namely, I would like to thank Dr. Paolo Federico, Dr. Bradley Goodyear, Dan Pittman and Jodi Edwards for their help with this project. The group provided me with advice and assistance in understanding some image analysis concepts to help guide me through. The group allowed me to visit them at the centre so I could be involved in patient imaging and image analysis. The group also provided the imaging data that was analyzed in this work. Lastly, I was invited by Dr. Federico to present my work at a conference and I would like to thank him for that opportunity.

I would like to thank Dr. Mani Vaidyanathan and Dr. Florin Dolcos. Both of these fellows provided me with a lot of encouragement to keep me motivated during my project. They both helped me stay positive, which is something I appreciate very much.

I would like to thank some very special friends of mine who provided me with a lot of support during my project. A special thank you goes out to Jayna Gilchrist, Krista Frohlich, Ben Burke and Leslie Robertson. Their encouragement helped me stay motivated and focused on my research.

Last and most importantly, I would like to thank my family. My mother Bess and my father Stewart, my brother Tyler and his wife Treena, my brother Tim and his girlfriend Lillian Shavalier, my aunt Norma May and uncle Bob May, my cousin Ryan May, my aunt Margaret Savage and uncle Larry Savage. Their love, support and encouragement was crucial in helping me work through this project.

Table of Contents

Chapter 1: Introduction 1
- *1.1 Motivation* 1
- *1.2 Background* 2
  - *1.2.1 Epilepsy* 2
  - *1.2.2 Functional Magnetic Resonance Imaging* 3
    - *1.2.2.1 Magnetic Resonance Imaging* 3
      - *1.2.2.1.1 The Acquisition of Magnetic Resonance Images* 3
      - *1.2.2.1.2 MRI Contrast Mechanisms* 7
    - *1.2.2.2 Blood-Oxygenation-Level-Dependent (BOLD) fMRI* 10
      - *1.2.2.2.1 The Hemodynamic Response* 10
      - *1.2.2.2.2 The Measurement of the Hemodynamic Response* 10
      - *1.2.2.2.3 Block Design and Event-Related Paradigms* 14
    - *1.2.2.3 MRI versus fMRI* 16
  - *1.2.3 The Statistical Analysis of fMRI Data* 18
    - *1.2.3.1 The General Linear Model* 18
    - *1.2.3.2 Regressors in the GLM* 19
    - *1.2.3.3 Statistical Tests* 23
    - *1.2.3.4 Software Available for Performing Statistical Tests* 29
  - *1.2.4 Independent Component Analysis* 29
    - *1.2.4.1 The Cocktail Party Problem* 29
    - *1.2.4.2 Statistical Independence* 30
    - *1.2.4.3 The Mathematical Model of ICA* 31
    - *1.2.4.4 Types of ICA* 33
  - *1.2.5 ICA versus Statistical Analysis Using the GLM* 34
  - *1.2.6 The Electrical Activity of the Brain* 36
    - *1.2.6.1 Electroencephalography* 36
    - *1.2.6.2 Electroencephalography and fMRI* 37
  - *1.2.7 Scope of the Work* 38
  - *1.2.8 Thesis Organization* 42

Chapter 2: Methods 43
- *2.1 The Acquisition of fMRI Data* 43
- *2.2 The Analysis of fMRI Data* 49
  - *2.2.1 Preprocessing* 50
    - *2.2.1.1 Slice Timing Adjustment* 50
    - *2.2.1.2 Motion Correction* 53
    - *2.2.1.3 Brain Voxel Extraction* 56
    - *2.2.1.4 Spatial Smoothing* 57
    - *2.2.1.5 Temporal Filtering* 61
  - *2.2.2 Parameter Estimation by Multiple Linear Regression* 63
  - *2.2.3 Statistical Inference* 67
- *2.3 The Assessment of GLMs* 73
  - *2.3.1 Statistics Used to Compare HR Model Performance* 73
    - *2.3.1.1 Concurrence Ratio* 73

2.3.1.2 Durbin-Watson Statistic 74
2.3.1.3 F-Statistic (to Assess HR Model Performance) 76
2.3.1.4 Adjusted Coefficient of Multiple Determination 77
2.4 Combined EEG-fMRI Scanning 78
2.4.1 Continuous versus Spike-Triggered EEG-fMRI Scanning 78
2.4.2 Artifacts in Combined EEG-fMRI Scanning 80
2.5 The Application of ICA to fMRI Measurements 82
2.5.1 Preprocessing 82
2.5.2 Principal Component Analysis versus Independent Component Analysis 84
2.5.3 The Calculation of Independent Components 90
2.6 fMRI Studies 94
2.6.1 Study 1: Block Design Paradigm 94
2.6.1.1 The Task 94
2.6.1.2 Imaging Sequence 95
2.6.1.3 Image Preprocessing 96
2.6.1.4 fMRI Measurement ICA 97
2.6.1.5 fMRI Measurement Statistical Analyses 106
2.6.1.6 HR Model Comparisons 108
2.6.2 Study 2: Event-Related Paradigm 108
2.6.2.1 The Events 108
2.6.2.2 Imaging Sequence 109
2.6.2.3 The EEG 110
2.6.2.4 Image Preprocessing 110
2.6.2.5 fMRI Measurement ICA 111
2.6.2.6 Impulse Response Preparations 114
2.6.2.7 fMRI Measurement Statistical Analyses 119
2.6.2.8 HR Model Comparisons 121

Chapter 3: Results 123
3.1 Study 1: Block Design Paradigm 123
3.1.1 Regressor Preparations 123
3.1.2 fMRI Measurement Statistical Analyses 132
3.1.3 HR Model Comparisons 135
3.2 Study 2: Event-Related Paradigm 136
3.2.1 Regressor Preparations 136
3.2.2 fMRI Measurement Statistical Analyses 151
3.2.3 HR Model Comparisons 161

Chapter 4: Discussion 163
4.1 Study 1: Block Design Paradigm 163
4.1.1 Regressors 163
4.1.2 Activation Maps 168
4.1.3 Performance of the HR Models 170
4.2 Study 2: Event-Related Paradigm 172
4.2.1 Regressors 172
4.2.2 Activation Maps 177

4.2.3 Performance of the HR Models 180

Chapter 5: Conclusions and Future Work 183
5.1 Conclusions from Studies 1 and 2 183
5.2 Future Directions 186

References 189

List of Tables

Table 3.1 Comparison of HR Models (Study 1).. 136
Table 3.2 Spatio-Temporal Component Derivation Results............... 139
Table 3.3 Comparison of HR Models (Study 2)............................... 162

List of Figures

Figure 1.1 Two Nuclear Magnetic Moments Rotating About the z-axis in the Presence of a Strong Static Magnetic Field........................ 4
Figure 1.2 Net Magnetization Vector.. 6
Figure 1.3 MR Image Slices of a Human Brain: Coronal, Sagittal and Axial 12
Figure 1.4 Block Design Paradigm.. 15
Figure 1.5 Event-Related Paradigm.. 15
Figure 1.6 Image of One Slice of a Subject's Brain Acquired Using MRI..... 17
Figure 1.7 Image of One Slice of a Subject's Brain Acquired Using fMRI.... 17
Figure 1.8 Example of a Gamma pdf... 21
Figure 1.9 Canonical HRF.. 23
Figure 1.10 Example t-distribution.. 28
Figure 2.1 Gradient Echo-Planar Imaging Sequence.............................. 44
Figure 2.2 G_z Gradient Strength Variation Along the z-axis.................... 47
Figure 2.3 G_y Gradient Strength Variation Along the y-axis..................... 49
Figure 2.4 Slice Timing Difference Between Two Slices........................ 51
Figure 2.5 fMRI Slice that Shows Pixels Containing Non-Brain Tissue....... 56
Figure 2.6 fMRI Slice in which Non-Brain Tissue is Removed................. 57
Figure 2.7 fMRI Slice Before Spatial Smoothing................................ 60
Figure 2.8 fMRI Slice After Spatial Smoothing.................................. 60
Figure 2.9 Two Time Courses of Residuals Plotted Against One Another.... 86
Figure 2.10 Mixed Signal 1.. 87
Figure 2.11 Mixed Signal 2.. 88
Figure 2.12 Principal Component Vectors in Mixed Signal Space............... 89
Figure 2.13 Independent Component Vectors in Mixed Signal Space........... 89
Figure 2.14 Finger Flexion Block Design Paradigm.............................. 95
Figure 2.15 International 10-20 System of Electrode Placements............... 109
Figure 2.16 Canonical Hemodynamic Impulse Response Power Spectrum..... 117
Figure 2.17 133-point Hamming Window.. 119
Figure 3.1 Spatial Independent Component Brain Map (Unaveraged fMRI Data).. 124
Figure 3.2 ROA+ BOLD Signal Time Course for Task-Related Spatial Independent Component (Unaveraged fMRI Data)................... 125
Figure 3.3 Spatial Independent Component Brain Map (Averaged fMRI Data).. 126
Figure 3.4 ROA+ BOLD Signal Time Course for Task-Related Spatial Independent Component (Averaged fMRI Data)...................... 127
Figure 3.5 Spatial ICA-Derived Regressor.. 127
Figure 3.6 Brain Map of Spatial Weights for the Task-Related Temporal Independent Component (Unaveraged fMRI Data)................. 128
Figure 3.7 Task-Related Temporal Component Time Course (Unaveraged fMRI Data)... 129

Figure 3.8 Brain Map of Spatial Weights for the Task-Related Temporal Independent Component (Averaged fMRI Data)...................... 129
Figure 3.9 Task-Related Temporal Component Time Course (Averaged fMRI Data).. 130
Figure 3.10 Temporal ICA-Derived Regressor.................................. 131
Figure 3.11 Canonical Hemodynamic Response Regressor....................... 131
Figure 3.12 Activation Map Computed Using Student's t-test with the Spatial ICA-Derived Regressor.. 133
Figure 3.13 Activation Map Computed Using Student's t-test with the Temporal ICA-Derived Regressor.. 134
Figure 3.14 Activation Map Computed Using Student's t-test with the Canonical Hemodynamic Response Regressor.......................... 135
Figure 3.15 Interictal Event-Related Spatial Independent Component Brian Map from Run 1.. 137
Figure 3.16 Interictal Event-Related Spatial Independent Component Brian Map from Run 2.. 138
Figure 3.17 Interictal Event-Related Spatial Independent Component Brian Map from Run 3.. 138
Figure 3.18 Spatio-Temporal ICA-Derived Hemodynamic Response, Canonical Response and Interictal Event Pulse Train Signal Superimposed on One Another (Run 1)................................ 140
Figure 3.19 Spatio-Temporal ICA-Derived Hemodynamic Response, Canonical Response and Interictal Event Pulse Train Signal Superimposed on One Another (Run 2)................................ 141
Figure 3.20 Spatio-Temporal ICA-Derived Hemodynamic Response, Canonical Response and Interictal Event Pulse Train Signal Superimposed on One Another (Run 3)................................ 141
Figure 3.21 Wiener Filter Magnitude Spectrum for Run 1........................ 142
Figure 3.22 Magnitude Response of Canonical Hemodynamic Impulse Response.. 143
Figure 3.23 Magnitude Response of Spatio-Temporal ICA-Derived Impulse Response (Run 1).. 143
Figure 3.24 Magnitude Response of Spatio-Temporal ICA-Derived Impulse Response (Run 2).. 144
Figure 3.25 Magnitude Response of Spatio-Temporal ICA-Derived Impulse Response (Run 3).. 144
Figure 3.26 Spatio-Temporal ICA-Derived Impulse Responses from Run 1 (Unsmoothed Frequency Response)...................................... 145
Figure 3.27 Smoothed Magnitude Spectrum of Spatio-Temporal ICA-Derived Impulse Response (Run 1)...................................... 146
Figure 3.28 Smoothed Magnitude Spectrum of Spatio-Temporal ICA-Derived Impulse Response (Run 2)...................................... 146
Figure 3.29 Smoothed Magnitude Spectrum of Spatio-Temporal ICA-Derived Impulse Response (Run 3)...................................... 147
Figure 3.30 Spatio-Temporal ICA-Derived Impulse Response from Run 1 (Smoothed Frequency Spectrum).. 148

Figure 3.31 Spatio-Temporal ICA-Derived Impulse Response from Run 2 (Smoothed Frequency Spectrum)... 148
Figure 3.32 Spatio-Temporal ICA-Derived Impulse Response from Run 3 (Smoothed Frequency Spectrum)... 149
Figure 3.33 Spatio-Temporal ICA-Derived Hemodynamic Response Superimposed on Spatio-Temporal Component Time Course (Run 1).. 150
Figure 3.34 Spatio-Temporal ICA-Derived Hemodynamic Response Superimposed on Spatio-Temporal Component Time Course (Run 2).. 150
Figure 3.35 Spatio-Temporal ICA-Derived Hemodynamic Response Superimposed on Spatio-Temporal Component Time Course (Run 3).. 151
Figure 3.36 Brain Map Showing Active Voxels Determined by t-test Using Canonical Hemodynamic Response Regressor (Run 1).............. 152
Figure 3.37 Brain Map Showing Active Voxels Determined by t-test Using Spatio-Temporal ICA-Derived Hemodynamic Response Regressor (Run 1).. 153
Figure 3.38 Brain Map Showing Active Voxels Determined by t-test Using Inverted Canonical Hemodynamic Response Regressor (Run 1)... 154
Figure 3.39 Brain Map Showing Active Voxels Determined by t-test Using Canonical Hemodynamic Response Regressor (Run 2).............. 155
Figure 3.40 Brain Map Showing Active Voxels Determined by t-test Using Spatio-Temporal ICA-Derived Hemodynamic Response Regressor (Run 2).. 156
Figure 3.41 Brain Map Showing Active Voxels Determined by t-test Using Inverted Canonical Hemodynamic Response Regressor (Run 2)... 157
Figure 3.42 Brain Map Showing Active Voxels Determined by t-test Using Canonical Hemodynamic Response Regressor (Run 3).............. 158
Figure 3.43 Brain Map Showing Active Voxels Determined by t-test Using Spatio-Temporal ICA-Derived Hemodynamic Response Regressor (Run 3).. 159
Figure 3.44 Brain Map Showing Active Voxels Determined by t-test Using Inverted Canonical Hemodynamic Response Regressor (Run 3)... 160

Glossary of Acronyms

AR(1)	first order autoregressive model
BOLD	Blood-Oxygenation-Level-Dependent
CR	Concurrence Ratio
CSF	cerebrospinal fluid
DW	Durbin-Watson (statistic)
EC	Euler Characteristic
EEG	electroencephalogram
fMRI	functional magnetic resonance imaging
FSL	fMRI of the brain Software Laboratory
FWE	family-wise error (rate)
FWHM	Full Width at Half Maximum
GIFT	Group ICA of fMRI Toolbox (software)
GLM	General Linear Model
GLS	generalized least-squares
GRE-EPI	gradient echo-planar imaging (sequence)
GRF	Gaussian Random Field (Theory)
HR	hemodynamic response
HRF	hemodynamic response function
ICA	Independent Component Analysis
iid	independent and identically distributed
MRI	magnetic resonance imaging
OLS	ordinary least-squares

PCA	Principal Component Analysis
pdf	probability density function
p-value	probability-value
R_a^2	adjusted coefficient of multiple determination
ReML	Restricted Maximum Likelihood
RF	radiofrequency (pulse)
ROA+	positive region of activation
SNR	signal-to-noise ratio
SPM	Statistical Parametric Mapping (software)
SSE	sum of squared errors
SSR	sum of squared regressor values
SST	total sum-of-squares
svd	singular value decomposition
TE	time-to-echo (echo time)
TR	repetition time or repeat time

Chapter 1

Introduction

The objective of this work has been the development of an improved method for localizing the region(s) of the brain responsible for the onset of seizure activity in patients suffering from partial epilepsy. The objective was achieved by the application of an analytical process called Independent Component Analysis (ICA) to measurements obtained using an imaging technology called functional magnetic resonance imaging (fMRI).

1.1 Motivation

An improved localization method was developed in this work to contribute to improving treatments that are available to patients with partial epilepsy. Surgical treatment involves the localization and excision of regions of abnormal tissue (lesions) responsible for a patient's epilepsy. Accurate localization of the lesion(s) improves the probability of a positive outcome for epilepsy patients for whom surgical intervention is the only hope of a cure. It was the opportunity to do this that provided the motivation for this work.

1.2 Background

1.2.1 Epilepsy

Epilepsy is a serious neurological disorder that affects about one per cent of the population in North America [1]. The disorder has several causes such as head trauma, congenital malformations, brain tumours and many others [1, 2].

People suffering from epilepsy periodically experience seizures. Seizures are attributed to sudden and excessive synchronous discharges from abnormal populations of neurons in localized areas of grey matter in the brain [1, 2]. During a seizure, a patient will elicit symptoms that depend on the affected brain regions. These symptoms include loss of consciousness, convulsions, inability to respond to external stimuli, blank staring and several others [2, 3].

Seizures can be classified many ways, but their broad classification into focal (partial) seizures and generalized seizures is important for this work. Focal seizures begin in specific localized regions of grey matter in the brain, called the epileptic foci, and result in symptoms that are linked to the affected brain regions [2]. On the other hand, generalized seizures have no local origin of onset and affect both hemispheres of the brain [2, 4]. Since the seizure onset region can be localized, patients with partial epilepsy that experience focal seizures were the focus of this work [2, 4, 5]

Epilepsy is most often treated with medication [2]. Unfortunately, the medication may not control the seizures or it may become ineffective over time [2, 6]. In these cases, surgery may be a possible alternative course of treatment.

1.2.2 Functional Magnetic Resonance Imaging

Functional magnetic resonance imaging is a form of magnetic resonance imaging (MRI) which can be used to acquire brain images that provide information about function in addition to information about anatomy. fMRI was discovered in the early 1990s and it continues to be a popular area of research [7, 8]. fMRI is used to study neural activity that occurs in stroke, motor control, cognition, epilepsy and other areas [9, 10].

1.2.2.1 Magnetic Resonance Imaging

MRI is an imaging modality that is mainly used to obtain images of soft tissue inside the body. It is used to generate images for both clinical applications and research. It is a very useful imaging modality to study anatomy because images with fine spatial resolution in any orientation can be acquired [11].

1.2.2.1.1 The Acquisition of Magnetic Resonance Images

Magnetic resonance images are acquired by manipulating magnetic fields that are applied to the body [12].

When subjects are imaged, they lie on a bed within an MR scanner in which a strong static magnetic field, called the $\mathbf{B_0}$ field, is present [9]. Typical static magnetic field magnitudes for human MRI are 1.5 Tesla (T), 3.0 T and 4.7 T. By convention, the direction of the static magnetic field is labeled the +z direction as shown in Figure 1.1 [12]. The z-axis is called the longitudinal axis [11].

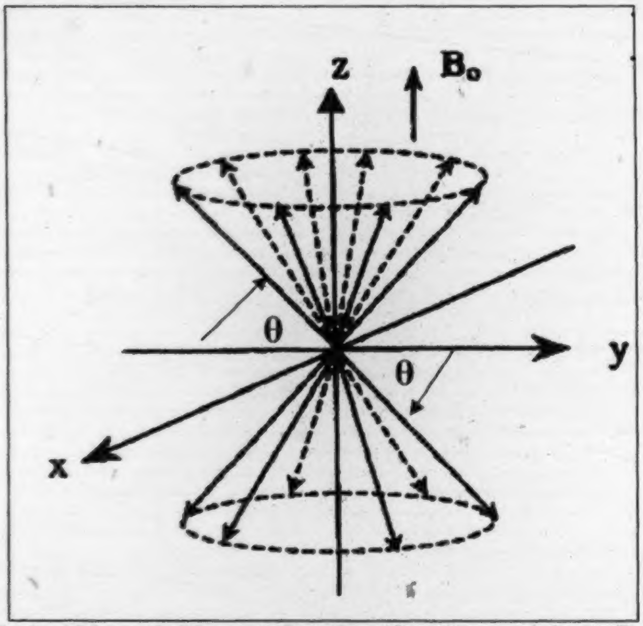

Figure 1.1 Two Nuclear Magnetic Moments Rotating About the z-axis in the Presence of a Strong Static Magnetic Field

Strong static magnetic fields have an effect on certain atomic nuclei within the body. Hydrogen atoms, which are abundant in the body as a part of water molecules and organic compounds, possess nuclear magnetic moments that are affected by strong static magnetic fields [12]. In the presence of a strong static field, hydrogen nuclear magnetic moments will align at an angle to the +z-axis or they will align at the same angle to the -z-axis. Figure 1.1 shows two nuclear magnetic moments, one black arrow aligned at angle θ to the +z-axis and one black arrow aligned at angle θ to the -z-axis. While in these positions, the static magnetic field exerts a torque on the nuclear magnetic moments, causing them to precess (rotate) about the +z-axis or -z axis as shown in Figure 1.1. Thus, each magnetic moment sweeps out a cone. The rate at which the magnetic moments precess about the z-axis is called the Larmor frequency. Equation (1.1) is the Larmor frequency equation.

$$\omega_0 = \gamma B_0 \quad (1.1)$$

The ω_0 variable is the radial frequency of the magnetic moments. The γ symbol represents the gyromagnetic ratio, which has units of MHz/Tesla. The gyromagnetic ratio is a constant and its value varies for different atomic elements that produce nuclear magnetic moments. Since gyromagnetic ratios vary between elements, magnetic moments from different elements will precess at different Larmor frequencies in the presence of the same static magnetic field. Lastly, B_0 in equation (1.1) is the static magnetic field magnitude.

Nuclear magnetic moments are vectors which sum together to produce a net magnetization vector that points in the +z-direction [12]. Regarding this point, many nuclear magnetic moments are aligned at the same angle θ to the +z-axis or -z-axis, however, the moments point in different directions as they lie at an angle to the z-axis. What can be deduced by observing Figure 1.1 is that each magnetic moment can be resolved into components along the x, y and z-axes. The resultant magnetization vector along the x-axis, which is obtained by summing the x-components from each magnetic moment, is nearly zero. This is because any components that lie along the +x-axis are cancelled by an equal number of components that lie along the -x-axis. The resultant magnetization vector along the y-axis is negligible for an analogous reason. With regard to the resultant magnetization vector along the z-axis, a larger proportion of the magnetic moments are aligned at an angle θ to the +z-axis because this is a lower energy state. Thus, there will be a larger number of components pointing in the +z-direction than in the -z-direction. The excess of components pointing in the +z-direction will produce a measurable magnetization vector along the +z-axis. The net magnetization vector is shown in Figure 1.2.

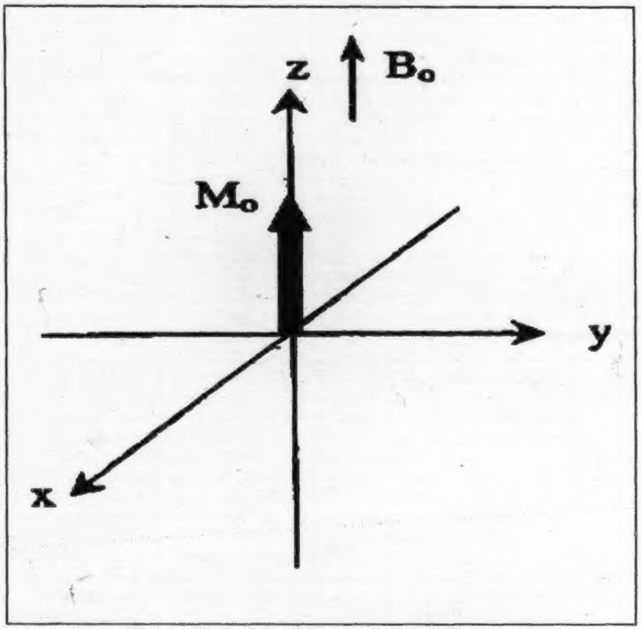

Figure 1.2. Net Magnetization Vector

Once a magnetization vector has been prepared in the body region being imaged, it is tipped into a plane that is perpendicular to the longitudinal axis direction using a radio frequency (RF) pulse [12]. This plane is called the transverse plane or x-y plane. The tipping occurs because the RF pulse generates a short-lived magnetic field that applies a torque to the magnetization vector. The field produced by the RF pulse is called a $\mathbf{B_1}$ field. The $\mathbf{B_1}$ field must rotate in the transverse plane about the z-axis with a frequency equal to the Larmor frequency of the atomic nuclei of interest. When the $\mathbf{B_1}$ field rotates at the Larmor frequency, a strong torque is applied to the magnetization vector. This torque forces the vector to rotate into the transverse plane [11, 12]. When the Larmor frequency and the $\mathbf{B_1}$ field frequency are equal, the $\mathbf{B_1}$ field is said to be in resonance with the Larmor frequency.

After the RF pulse is removed, the magnetization vector that was tipped into the transverse plane will begin to precess back toward the +z-axis to return to its original state [11]. Consequently, an electric current will be induced in a metal coil of wire that is placed around the part of the body being imaged [12]. This electric current is measured and used to produce magnetic resonance images. In addition, the magnetization vector that is being regenerated along the +z-axis may be tipped into the transverse plane again by another RF pulse to obtain another image of the same tissue.

During the signal measurement period, the magnetization vector in the transverse plane is also spatially encoded by magnetic fields called gradients [12]. Spatial encoding is used to vary the static magnetic field strength along three dimensions so that the precise spatial location of a measured magnetization vector is known. Gradient fields are added to or subtracted from the static magnetic field magnitude in a linear fashion along the x, y or z-axes. Since it is known how the static magnetic field varies along each axis, the data collected can be properly processed to determine the signal strength at different locations in the body. Compared to static magnetic fields, gradient field magnitudes are much smaller [9]. Typical gradient magnetic field magnitudes are between 25-40 mT/metre.

1.2.2.1.2 MRI Contrast Mechanisms

In MRI, there are several mechanisms available to obtain contrast between different tissues in MR images. Two contrast mechanisms that are commonly used in MRI and fMRI are based on a phenomenon called relaxation [12, 13].

The first mechanism is called longitudinal relaxation, which occurs when the magnetization vector recovers along the +z-axis [11]. The vector will eventually increase to the magnitude it had before it was perturbed by an RF pulse [12]. Longitudinal relaxation occurs because the nuclear magnetic moments of the perturbed hydrogen atoms interact with the surrounding environment, which includes the static magnetic field [9]. This causes the magnetic moments to "relax" back to their original state at an exponential rate that has a time constant T_1. Thus, longitudinal relaxation can also be referred to as T_1 relaxation. The images acquired when longitudinal relaxation is exploited are called T_1-weighted images.

The T_1 time constant varies for different tissue types, so imaging sequences are designed to take advantage of this fact to generate images with sharp contrast between tissues [9]. For example, cerebrospinal fluid (CSF) has a much longer T_1 than grey matter in the brain. An imaging sequence can be designed to tip the magnetization vectors originating from CSF and grey matter into the transverse plane. After a period of time, a larger proportion of magnetic moments from grey matter will have relaxed. At this point, if the magnetization is tipped again and measured, the resulting signal will have a larger contribution from grey matter than from CSF. Hence, there will be significant contrast between grey matter and CSF in the image.

The other important form of relaxation, known as transverse relaxation, occurs when the magnetization vector magnitude decreases after it has been tipped into the transverse plane [12]. This occurs for several reasons, such as imperfections (inhomogeneities) in the static magnetic field and differences in the magnetic field that different tissues experience [9, 12]. These influences cause the magnetization in the transverse plane to diminish over time [11]. Just as in longitudinal relaxation, transverse relaxation is an exponential process with a time constant T_2* [12]. The images acquired when transverse relaxation is exploited are called T_2^*-weighted images.

Fortunately, static field inhomogeneities may be corrected using an RF pulse called a spin-echo [12]. A consequence of using a spin-echo is that it will increase the time it takes the transverse magnetization to diminish to zero. When spin-echoes are used, only random time-dependent interactions, such as the interactions of hydrogen nuclei with other hydrogen nuclei in the surrounding environment, cause the magnetization to decay over time [11, 12]. Thus, the magnetization decreases exponentially with a time constant of T_2, which is longer than T_2* [12]. The tradeoff when using a spin-echo is that it requires a longer imaging time [11].

Much like the T_1 time constant, T_2 and T_2* varies for different tissues [12]. After the magnetization vector is tipped, the magnetization vector contribution from the tissue with the shorter transverse relaxation time will decrease faster than the contribution from the tissue with the longer relaxation time [9]. When the signal is measured, the tissue with a longer transverse relaxation time will make up a larger proportion of the signal than the tissue with the shorter transverse relaxation time. For example, a magnetization vector may be composed of magnetic moment contributions from hydrogen nuclei in fat and skeletal muscle. Fat tissue has a longer T_2 (T_2*) than skeletal muscle, so a T_2-weighted image of these tissues will show contrast between fat and skeletal muscle [14].

Transverse relaxation, particularly T_2^*, is the contrast mechanism that is commonly exploited in fMRI [13]. Transverse relaxation occurs quickly, so fMRI sequences must be fast to capture functional information. During an fMRI sequence, there is usually not enough time to include a spin-echo or to run multiple RF pulses to obtain T_1 contrast. However, T_1-weighted MR images are often acquired from subjects in addition to fMR images to provide the necessary detailed information about each subject's anatomy.

1.2.2.2 Blood-Oxygenation-Level-Dependent (BOLD) fMRI

The most common type of fMRI is blood-oxygenation-level-dependent (BOLD) fMRI [9]. It is called BOLD fMRI because it is used to measure differences in blood oxygenation and blood flow to obtain information about brain function.

1.2.2.2.1 The Hemodynamic Response

Neural activity in the brain that occurs when a subject performs a task or experiences a stimulus usually causes an increase in blood flow and blood oxygenation in a localized region [9, 15]. This region may be a few millimetres from the site of the neural activity. This change in blood flow and blood oxygenation is called the hemodynamic response [9, 16]. The hemodynamic response occurs because energy-requiring metabolic events, such as glial cell processes and synaptic activities, take place when neurons transmit action potentials [9]. A supply of oxygen and glucose is delivered by the blood to be used as raw materials for energy production.

1.2.2.2.2 The Measurement of the Hemodynamic Response

The hemodynamic response is measured during a BOLD fMRI scan [17]. When a hemodynamic response occurs, an increased amount of oxygenated blood is often delivered to a localized region near the site of neural activity [9]. The oxygenated blood is actually in excess because the proportion of oxygen extracted from the increased blood volume is reduced compared to the proportion of oxygen extracted from the blood under resting (baseline) blood flow conditions. Thus, there is a decrease in the proportion of deoxyhemoglobin in the blood during a hemodynamic response. This results in a measurable increase in the signal measured by BOLD fMRI [9, 18].

The change in signal strength occurs because oxyhemoglobin and deoxyhemoglobin have magnetic properties that affect BOLD fMRI signal measurements [9]. Oxyhemoglobin is diamagnetic, which means it repels the magnetic field applied to it. As a result, local magnetic field distortions decrease. This causes a slight increase in the signal measured during a BOLD fMRI scan. On the other hand, deoxyhemoglobin exhibits a paramagnetic effect by allowing the applied magnetic field to be attracted into the deoxyhemoglobin molecule. This effect increases distortions in the magnetic field surrounding a deoxyhemoglobin molecule, which slightly decreases the measured BOLD fMRI signal. Coincidentally, BOLD fMRI signals only indicate the presence or absence of deoxyhemoglobin [18]. A BOLD signal does not indicate the proportion of oxyhemoglobin present because molecules other than oxygen, such as carbon monoxide, can bind to hemoglobin and decrease the concentration of deoxyhemoglobin without increasing the concentration of oxyhemoglobin [17].

In an fMRI scan, thousands of BOLD measurements are taken. The brain tissue is divided into small three-dimensional volume elements, known as voxels, by the fMR imaging sequence [19]. A voxel's dimensions vary from study to study, but its length and width in the plane of the image are usually 2-4 mm while its thickness is usually larger at about 5-10 mm. A series of adjacent voxels form one slice of a brain image [12]. Several adjacent slices form one whole brain image called a brain volume [20]. fMR images, as well as MR images, are viewed slice-by-slice. Slices may be viewed in different orientations in fMR images and MR images. Slice orientations may be axial (top to bottom of the head), sagittal (left to right of the head) and coronal (front to back of the head) [12, 21]. Slices from T_1-weighted anatomical MR images of the brain in each of these orientations are shown in Figure 1.3.

Figure 1.3. MR Image Slices of a Human Brain: Coronal Direction (Top Left), Sagittal Direction (Top Right) and Axial or Transverse Direction (Bottom)

BOLD signal samples are measured from each voxel in the entire brain volume multiple times over the course of the scan. Thus, signal samples from one voxel make up a time sequence (time course); since there are thousands of voxels, then there are thousands of BOLD time courses that are measured and prepared for subsequent analyses.

Many of the measured BOLD time courses may contain a hemodynamic response that corresponds to the neural activity of interest. Usually, a positive BOLD response follows shortly after the neural activity has occurred [17]. It is called a positive BOLD response because the measured time course increases in magnitude for a short time after the neural activity takes place. This increase in signal strength is a result of decreased deoxyhemoglobin concentration in a region occupied by the voxel from where the BOLD signal was measured. Positive BOLD response measurements indicate that the hemodynamic response is sluggish [16]. This is because the measured BOLD hemodynamic responses usually do not start for about 1-2 seconds after neural activity begins [17]. The positive BOLD response increases until it reaches a peak about 5-8 seconds after the neural activity begins and then decreases back to the baseline level 7-13 seconds later. Positive BOLD responses that correspond to significant neural events have an amplitude increase of approximately 0.5-3 % relative to the baseline BOLD signal level measured from a patient using a 1.5 T scanner [17, 22, 23]. The amplitude increases even more when BOLD signals are measured using a scanner with a stronger static magnetic field [24].

Positive BOLD responses occur often during fMRI, but negative BOLD responses corresponding to neural activity of interest have been recorded as well [25, 26]. The physiology of positive BOLD responses is understood better than that of negative BOLD responses because the former has been investigated more thoroughly [25]. One idea that has been proposed to explain negative BOLD responses is that there is a decrease in metabolic activity. This decrease in metabolic activity occurs because synaptic events take place that inhibit action potential propagation [25, 26]. The decrease in metabolic activity has a low energy demand, so an increase in blood flow is not required. Thus, deoxyhemoglobin concentration increases which results in a decreased BOLD signal. An important point to note is that the energy demand is still low even when the energy required to inhibit neurons from propagating action potentials is considered [26]. Whatever the cause, negative BOLD responses have been observed in fMRI studies that investigate many types of neural activity, including activity which is involved in sensorimotor tasks and epilepsy [25, 27].

1.2.2.2.3 Block Design and Event-Related Paradigms

There are two paradigms that are used during fMRI to evoke neural activity in a subject. The first is the block design paradigm and the second is the event-related paradigm.

When a block design paradigm is used, a subject alternates between intervals of performing an activity and resting [13]. The rest periods and activity periods have a constant duration. However, the rest period duration may or may not be equal to the activity period duration. A typical block design paradigm is a finger flexion motor control study. In this type of fMRI study, subjects tap their forefingers and thumbs together for a period of time (ten seconds or more) and then rest for a period of time [28]. The activity period and rest period are repeated several times during the fMRI scan [29]. During each activity interval and rest interval, BOLD signal samples are measured from every voxel. The time that elapses when the subjects complete one task period and the rest period that immediately follows is called a cycle (trial) in the imaging procedure. An illustration of the block paradigm is shown in Figure 1.4.

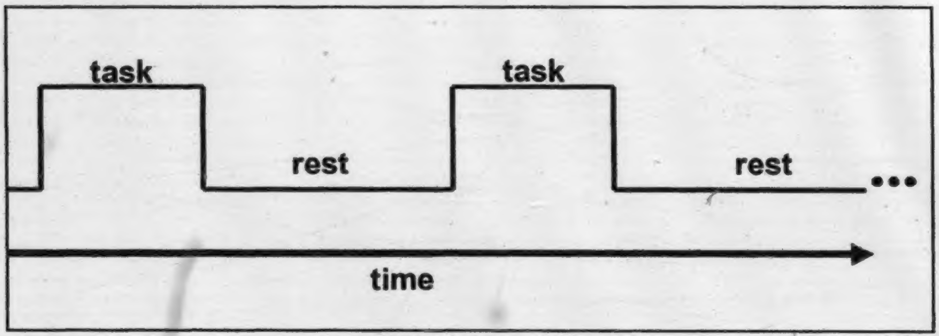

Figure 1.4. Block Design Paradigm

Block design paradigms are represented by the square wave shown in Figure 1.4 [11]. The task portion of the paradigm is represented by the positive phase of the square wave, while the rest portion is represented by the negative phase of the square wave [11, 30].

When an event-related paradigm is used, subjects experience brief stimuli or perform short tasks at random or predetermined points during the scan [6, 13, 31]. An example of this type of paradigm has been used to study neural activity involved in processing auditory stimuli [31]. During the scans, subjects hear brief tones of different frequencies at random points in time. The event related paradigm is depicted in Figure 1.5 [29, 31].

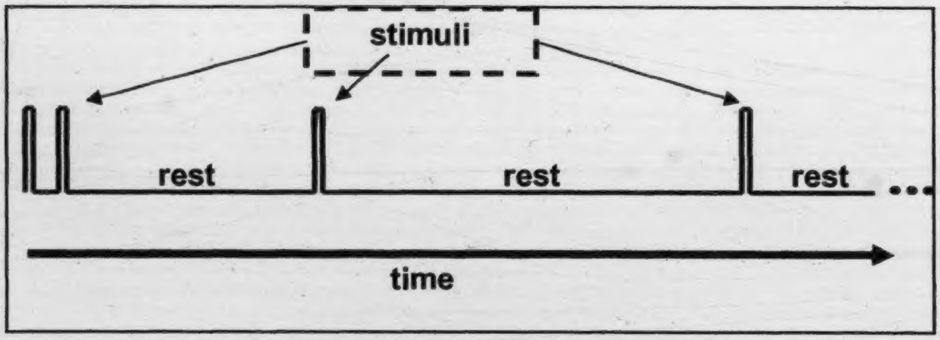

Figure 1.5. Event-Related Paradigm

The events are shown as short duration rectangular pulses in Figure 1.5 [29, 32]. The events may also be represented with Dirac Delta functions [32, 33]. The rest periods, represented by the baseline values of the rectangular pulses, usually have random durations [13].

1.2.2.3 MRI versus fMRI

MR and fMR images are obtained for different reasons. Magnetic resonance images have a very fine spatial resolution because they are examined for anatomical abnormalities [11]. On the other hand, fMR images are examined to find information about brain function. Subjects undergoing fMRI scans often have MRI scans as well. This is so the subjects' fMR images can be registered to their anatomical MR images. During the registration process, fMR image voxels are registered (matched) to corresponding locations on anatomical MR images that have a fine spatial resolution. Registration is performed to allow the results of the fMRI statistical analyses to be localized onto the anatomical MR images. Registration allows for a more accurate assessment of the potential regions of neural activity [20]. An axial MR image of one slice of a subject's brain is shown in Figure 1.6. An image of a slice (axial orientation) positioned at about the same location in the same subject is shown in Figure 1.7, except this image was acquired using fMRI. These images are shown to illustrate the finer spatial resolution that anatomical MR images have over fMR images. The physical dimensions of both images are 240 mm x 240 mm. However, the image in Figure 1.6 is 256 pixels x 256 pixels and the image in Figure 1.7 is 128 pixels x 128 pixels. Anatomical details are much clearer in the MR image than the fMR image.

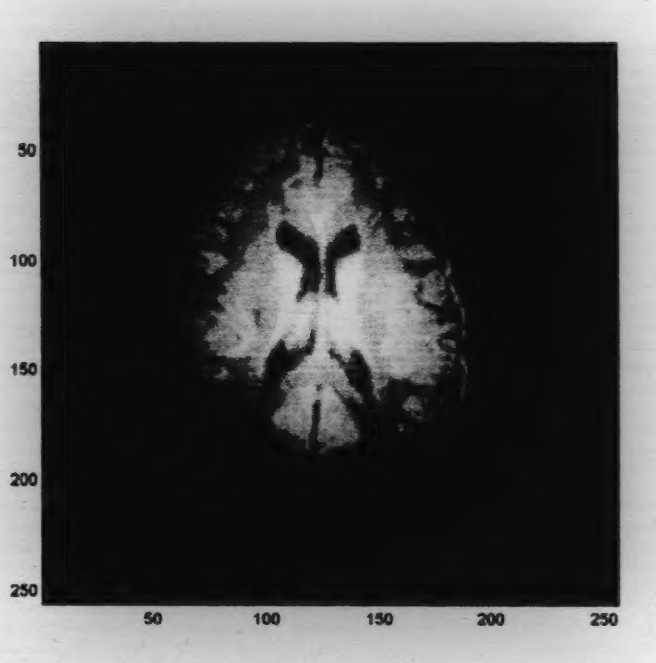
50
100
150
200
250
50
100
150
200
250

Figure 1.6. Image of One Slice of a Subject's Brain Acquired Using MRI

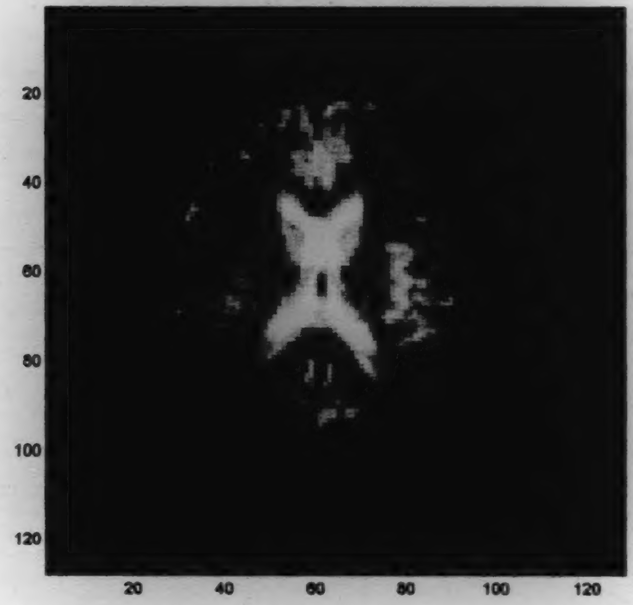
20
40
60
80
100
120
20
40
60
80
100
120

Figure 1.7. Image of One Slice of a Subject's Brain Acquired Using fMRI

1.2.3 The Statistical Analysis of fMRI Data

After the fMR images have been collected, they are examined using a statistical analysis to determine the brain regions that show a significant BOLD signal change when a subject performs a task or experiences a stimulus [32]. There are several types of statistical analyses that may be performed, but the most common is a statistical parametric test that is based on the General Linear Model [34, 35].

1.2.3.1 The General Linear Model

The General Linear Model (GLM) is a linear system of equations that is used to account for the measurements that are made during an fMRI scan [30, 34]. The assumption that is made when using a GLM is that the fMRI measurements can be represented by a linear combination of estimated time courses [34]. Equation (1.2) represents the GLM.

$$\mathbf{Y} = \mathbf{G}\boldsymbol{\beta} + \boldsymbol{\varepsilon} \qquad (1.2)$$

The **Y** matrix is called the data matrix because it contains the BOLD time courses measured from every voxel during an fMRI scan [33]. Each row in the **Y** matrix is a time sample and each column is a voxel.

The **G** matrix is called the design matrix [30]. This matrix contains several signals that are designed to account for different phenomena that may contribute to the measured signals in the data matrix [20, 30, 34]. For example, one or more signals may be designed to represent the BOLD response that is expected shortly after the subject experiences a stimulus or performs a task [34]. In addition, the design matrix may contain signals that are used to account for artifacts, such as noise or head motion [20]. These effects must be accounted for in the design matrix, otherwise they could cause the statistical analysis to produce erroneous results [36]. Signals that account for artifacts in the design matrix are called confounds [15, 37]. Each signal in the **G** matrix is also referred to as a regressor, explanatory variable or covariate [30, 34]. The regressors form the columns of the **G** matrix and time samples form the rows of the **G** matrix [30].

The **β** matrix is known as the parameter matrix [30]. This matrix is filled with coefficients that "fit" the regressors in the **G** matrix to each BOLD signal in the **Y** matrix. Hence, when the **G** and **β** matrices are multiplied together, the resulting product matrix will contain several time courses. Each time course will approximate a corresponding signal in the **Y** matrix as closely as possible. Each row of the **β** matrix contains the weight of a regressor at each voxel. Each entry in the **β** matrix is estimated during a parameter estimation step.

The **ε** matrix in the GLM is called the residual matrix [30]. This matrix contains values that are the arithmetic differences between the measured signals in the **Y** matrix and the estimated signals calculated from the product of the **β** and **G** matrices. Thus, each element in **ε** is the error at each time instant and voxel. The number of rows in the residual matrix corresponds to the number of time samples and the number of columns corresponds to the number of voxels.

1.2.3.2 Regressors in the GLM

Designing regressors to place in the **G** matrix is a difficult task. This is because, in most statistical analyses involving the GLM, several regressors are included to account for a variety of effects that may appear in the fMRI measurements [15].

The regressors that are intended to model the BOLD signal changes that occur shortly after the neural activity of interest are the important parts of the **G** matrix. These regressors are created by considering the relationship between neural activity and a resulting hemodynamic response [15, 32]. Neural activity is considered to be an input signal to a linear, time-invariant system. The system, in the case of fMRI, is a voxel. The input signal is a square wave (boxcar) (Figure 1.4) if a block design paradigm is used or a pulse signal (Figure 1.5) if an event-related paradigm is used. The times in which the neural activity is initiated correspond to the times in which the signals begin a positive phase in Figure 1.4 and Figure 1.5. A voxel is assumed to receive the input signal and, in turn, produce an output BOLD response signal that is a delayed and blurred version of the input signal [15, 30, 36]. A voxel is assumed to behave this way to illustrate the physiological fact that the BOLD hemodynamic response does not begin for 1-2 seconds after the neural activity is initiated (the delay) and lasts for several seconds before settling back to the baseline level (the blur).

Since the input-output behaviour of a voxel is considered a linear, time-invariant system, regressors that are intended to model a BOLD hemodynamic response to neural activity are developed by convolving the input signal with an impulse response function that represents a voxel's actions on the input [15]. The impulse response function of a voxel is called the hemodynamic response function (HRF). The input signal in fMRI is often called the stimulus function. The convolution operation is depicted by equation (1.3) [36].

$$y(t) = hrf(t) * s(t) = \int_{\tau=0}^{\infty} hrf(\tau)s(t-\tau)d\tau \quad (1.3)$$

The hrf(t) variable is the hemodynamic response function and the s(t) variable is the stimulus function. The output variable y(t) is the BOLD hemodynamic response which is measured during an fMRI scan.

Several HRFs have been designed and used in past fMRI studies. Some examples of HRFs are the Gamma and Poisson probability density functions [15]. An example of a Gamma probability density function (pdf) is shown in Figure 1.8. This Gamma pdf is shown as it would be used as a regressor, not as a true pdf. This is why the vertical axis is labeled as normalized magnitude (instead of probability values) and the horizontal axis is labeled as time (instead of possible outcomes of a random variable).

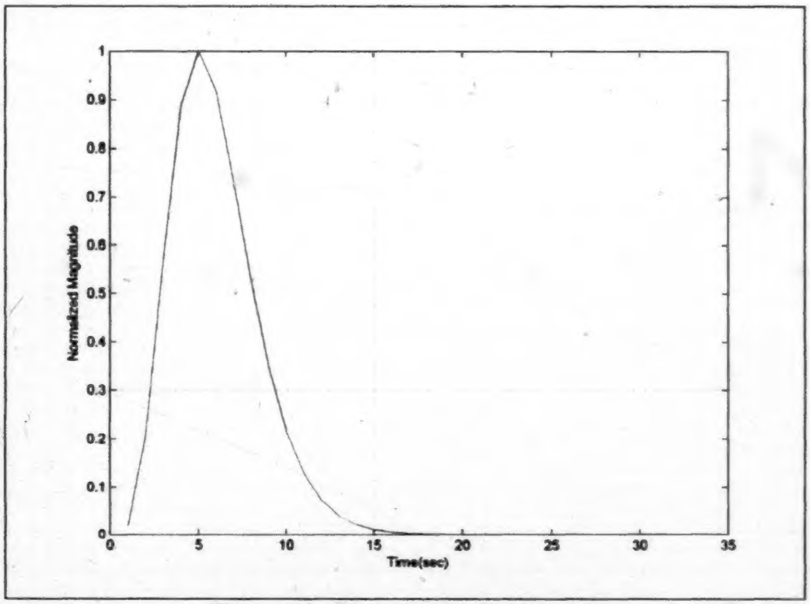

Figure 1.8. Example of a Gamma pdf

More recently, the canonical HRF has become a very popular HRF [4, 15]. It has been used in fMRI studies of many different types of neural activity, including studies of motor control and epileptic neural activity [4, 10, 38]. Interesting localization results have been discovered using the canonical HRF. The canonical HRF is actually the arithmetic difference between 2 different Gamma pdfs [4, 39]. The canonical HRF was designed in a study conducted by Friston and colleagues in 1998 [36, 40]. Equation (1.4) below describes the canonical HRF [39].

$$\mathrm{C(t)} = \frac{1}{\Gamma(\alpha=6)}t^{5}e^{-t} - \frac{1}{\Gamma(\alpha=16)}t^{15}e^{-t}; \quad \mathrm{t} > 0 \qquad (1.4)$$

Each term on either side of the subtraction sign in equation (1.4) is an example of a Gamma pdf. The first term is actually the Gamma pdf shown in Figure 1.8. The Γ variable in equation (1.4) is the Gamma function (not to be confused with the Gamma pdf) evaluated with the shape parameter α. The variable t in equation (1.4) is time. The Gamma function is shown by the formula in equation (1.5) [41, 42].

$$\Gamma(\alpha) = \int_{t=0}^{\infty} \mathrm{t}^{\alpha-1}e^{-t}dt \qquad (1.5)$$

The canonical HRF computed by evaluating equation (1.4) is displayed in Figure 1.9.

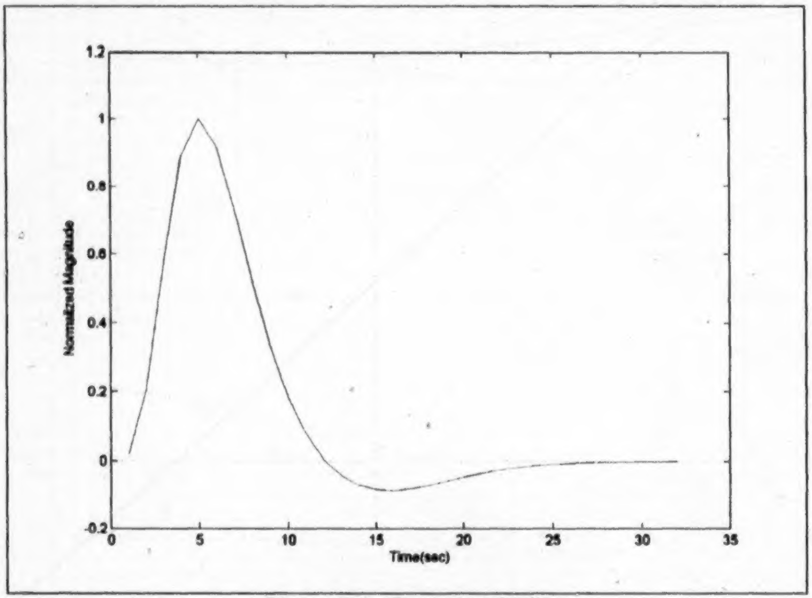

Figure 1.9. Canonical HRF

Other regressors that are placed in the design matrix to account for confounding effects are typically not convolved with any function [15]. These regressors may be cosine or sine functions that are included to account for low frequency noise in the fMRI measurements [43]. Regressors that account for head motion that occurred during the fMRI scan may also be used [44]. In addition, polynomial functions may be inserted into the design matrix to account for other confounds [43]. Lastly, a signal with constant amplitude of one is always placed in the design matrix [30, 45]. This signal accounts for the non-zero baseline BOLD signals (BOLD signals with a non-zero mean) that are measured during the fMRI scan.

1.2.3.3 Statistical Tests

A statistical test is performed on fMRI measurements to find localized brain regions in which there is a high probability that significant BOLD responses occurred when the subjects were exposed to a particular stimulus or task [15, 30]. Regions identified by statistical tests in which task-related or stimulus-related BOLD responses occurred are called active regions. Moreover, every voxel within an active region is an active voxel. Statistical tests are performed immediately after the values in the **β** matrix are estimated. The parameter estimates (estimated values of the **β** matrix) are the values used in the statistical tests to determine the locations of active regions.

One common statistical test in fMRI is the two sample Student's t-test. The t-test is used to determine if there is a significant difference in means between two populations [11, 46]. When the t-test is used on fMRI measurements, it is assumed that each measured BOLD signal belongs to one of two populations: active periods or rest periods that occur during an fMRI scan [11]. If there is no significant difference between the means of the BOLD signals that are measured from these two populations, then the neural activity did not produce any significant BOLD hemodynamic responses.

A statistical hypothesis is implemented during a t-test that states that the parameter estimates all occurred by chance and that there were no significant BOLD hemodynamic responses to the neural activity [15, 36]. The parameter estimates are treated as the means of the rest period signal and active period signal populations. This is because a parameter estimate is an average "fit" for a particular regressor at a particular voxel. The hypothesis that there were no significant BOLD responses to the task or stimulus is called the null hypothesis. Important parameter estimates (i.e. **β** matrix estimates corresponding to the regressor(s) that represent the assumed BOLD responses to a task or stimulus) that have a very low probability of occurring by chance according to a t-test will result in the corresponding voxels to be active. Parameter estimates with low probabilities of occurring by chance cause the null hypothesis to be rejected in favor of an alternate hypothesis. The alternate hypothesis states that there were significant BOLD responses measured following neural activity.

Student's t-tests are usually used when one regressor's parameter estimates are tested against the baseline level or the difference between parameter estimates of two regressors is tested [47]. The regressors being tested represent BOLD responses that occurred during different tasks or stimuli that subjects were exposed to during an fMRI scan. When performing a t-test, all parameter estimates are assumed to be distributed according to a Student's t-distribution. This probability distribution is the expected distribution of the parameter estimates if there were no significant BOLD responses.

Each parameter estimate is substituted into a formula to calculate a t-statistic (or t-value) that corresponds to a value along the horizontal axis of a Student's t-distribution [47]. Equation (1.6) is the formula for the t-statistic. The t-statistic will correspond to a probability value (p-value) along the vertical axis of the t-distribution. A p-value indicates the probability that the corresponding parameter estimate occurred by chance.

$$t = \frac{\mathbf{c}^T \hat{\beta}}{\sqrt{\widehat{\mathrm{var}}(\mathbf{c}^T \hat{\boldsymbol{\beta}})}} \qquad (1.6)$$

In equation (1.6), $\hat{\beta}$ is the parameter estimate for a single regressor at one voxel. In the denominator is the estimated standard deviation of the parameter estimates for one regressor across all voxels. The term in the denominator is sometimes called the standard error of the parameter estimates. The vector **c** is the called a contrast vector. The contrast vector is transposed in equation (1.6) as indicated by the 'T'. This vector selects the regressors that will be used in the t-test. For example, in an fMRI statistical test in which the $\hat{\boldsymbol{\beta}}$ matrix contains three regressors, there may be interest in seeing the difference in active regions between the first regressor and baseline activity. In this case, the contrast vector would be $\mathbf{c}^T = [1\ 0\ 0]$. It is important to note in this case that parameter estimates of baseline BOLD signal activity (mean of the rest period signal population) are zero. In another example, there may be interest in seeing the difference in active regions between the first and third regressors. In this case, the contrast vector would be $\mathbf{c}^T = [1\ 0\ {-1}]$.

F-tests are slightly more complicated than t-tests; they are usually performed when there is an interest in examining the effect of a linear combination of regressors [47]. If an F-test is performed, the parameter estimates are assumed to be distributed according to an F-distribution.

Parameter estimates are substituted into a formula to calculate F-statistics (or F-values) to use in an F-test [47]. The F-statistic calculated for each parameter estimate indicates the parameter estimate's position along the horizontal axis of an F-distribution. The F-value will correspond to a p-value on the F-distribution. The p-value indicates the probability that the parameter estimate occurred by chance. The formula for an F-statistic is given by equation (1.7).

$$F = \frac{\hat{\beta}^{T}\mathbf{c}(\hat{\mathrm{var}}(\mathbf{c}^{T}\hat{\beta}))^{-1}\mathbf{c}^{T}\hat{\beta}}{\nu_2} \qquad (1.7)$$

Terms in the F-statistic equation are the same as the terms in the t-statistic equation except the variable υ_2, which is a degrees-of-freedom term. Degrees-of-freedom will be explained shortly. In addition, **c** is now a matrix instead of a vector. With regard to the example scenario presented earlier in which there were three regressors, there may be interest in identifying the active regions that correspond to the first two regressors. In this case the contrast matrix would be $\mathbf{c}^T = \begin{bmatrix} 1 & 0 & 0 \\ 0 & 1 & 0 \end{bmatrix}$

There is not just one t-distribution or one F-distribution that is used in a t-test or F-test on fMRI measurements, respectively. The shape of a t-distribution or F-distribution changes depending on variables called degrees-of-freedom [47]. In fMRI studies, degrees-of-freedom are affected by the number of BOLD signal time samples and the number of regressors. t-distributions are affected by one degrees-of-freedom variable and F-distributions are affected by two degrees-of-freedom variables. Equation (1.8) shows the t-distribution degrees-of-freedom [33].

$$\nu = T - p \qquad (1.8)$$

The T variable is the number of BOLD signal time samples (brain volumes) acquired. The p variable is the number of regressors in the design matrix. Equations (1.9)(a) and (1.9)(b) show the two formulas for the degrees-of-freedom of the F-test [48].

$$\begin{matrix} \nu_1 = p - 1 & (a) \\ \nu_2 = T - p. & (b) \end{matrix} \qquad (1.9)$$

The variables in equations (1.9)(a) and (1.9)(b) are the same variables in equation (1.8). As the degrees-of-freedom increase, the shape of a t-distribution or F-distribution approaches the shape of a normal (Gaussian) distribution.

To complete a statistical test, a threshold must be chosen for the t-statistic or F-statistic p-values to identify active voxels [11]. This threshold is implemented so that any calculated p-value equal to or lower than the threshold indicates that the corresponding parameter estimate value likely did not occur by chance. Thus, the voxel that possesses this parameter estimate has a high probability of being active. This procedure is illustrated in Figure 1.10 on a hypothetical t-distribution. Common thresholds chosen in fMRI studies are $p \leq 0.05$ or $p \leq 0.01$.

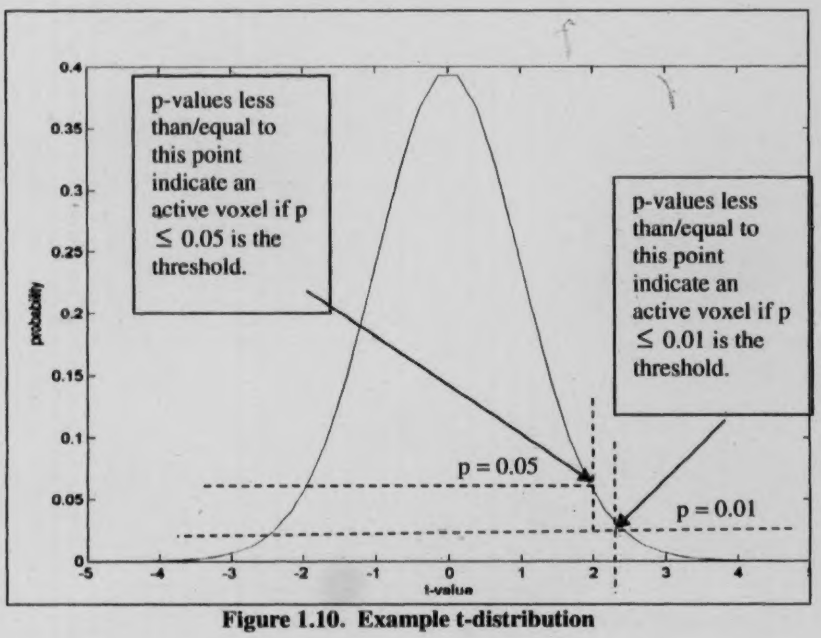

p-values less than/equal to this point indicate an active voxel if $p \leq 0.05$ is the threshold.

p-values less than/equal to this point indicate an active voxel if $p \leq 0.01$ is the threshold.

Figure 1.10. Example t-distribution

1.2.3.4 Software Available for Performing Statistical Tests

There are numerous software programs available for performing statistical analyses on fMRI measurements using the GLM.

One very popular software program is called Statistical Parametric Mapping (SPM) (Wellcome Department of Imaging Neuroscience, London, UK). SPM is a software program that runs in the MATLAB programming environment. All stages of the analysis from image preprocessing to viewing statistical test results on brain images may be performed with SPM.

Another well known software program for performing statistical analyses on fMRI measurements is fMRI of the Brain Software Laboratory (FSL) (fMRIB Analysis Group, Oxford, UK). Much like SPM, all stages of the analysis can be performed with FSL. However, FSL does not run in the MATLAB environment.

1.2.4 Independent Component Analysis

In several fields, such as telecommunications and biomedical signal processing, signals are measured to study various phenomena. A common problem with the signal measurements is that they may be composed of a mixture of important underlying signals that are unknown [49]. Independent Component Analysis (ICA) is a signal analysis method that is used to recover the underlying signals.

1.2.4.1 The Cocktail Party Problem

ICA can be explained with a simple example known as the cocktail party problem [49]. In this problem, several people are speaking simultaneously in one room.

Several microphones are scattered throughout the room. Each microphone records one sound signal that is produced from a mixture of speech signals from everyone in the room. The signal recorded by each microphone is called a mixed signal and the speech signal from each person is called a source signal. The source signals are recovered from the mixed signals to solve the problem. ICA is a method that can be used to solve the cocktail party problem.

To apply ICA to the cocktail party problem (and other related problems), a few assumptions are made [49]. First, it is assumed that speech signals mix together in a linear fashion. Thus, each mixed signal is a weighted sum of speech signals. It is also assumed that each speech signal is statistically independent from all other speech signals. This is a reasonable assumption because each speech signal is completely separate from all the other speech signals. Statistical independence is exploited so that ICA may be applied to determine all of the underlying speech signals. The speech signals that are calculated using ICA are called independent components.

1.2.4.2 Statistical Independence

Statistical independence is an important property in ICA. To exploit statistical independence and apply ICA, source signals and mixed signals are assumed to be random variables [49]. Random variables that are statistically independent satisfy equation (1.10) [35].

$$p(s_1, s_2, \ldots, s_N) = \prod_{i=1}^{N} p(s_i) \qquad (1.10)$$

The s variables in equation (1.10) are random variables and N is the number of random variables. The variable $p(s_1, s_2, ..., s_N)$ is the joint pdf of the random variables s_1 through s_N. Lastly, $p(s_i)$ is the pdf of each separate random variable s_1 through s_N. Equation (1.10) states that if the random variables are statistically independent, the product of the random variable pdfs is equal to the joint pdf of the random variables. Source signals that are computed using ICA would approximately satisfy equation (1.10) [49].

1.2.4.3 The Mathematical Model of ICA

The mathematical model of ICA is the linear system of equations shown in equation (1.11) [49].

$$\mathbf{x} = \mathbf{A}\mathbf{s} \qquad (1.11)$$

The **x** matrix contains the signal measurements and is called the data matrix. The matrix **A** contains real coefficients that describe how the source signals are mixed together to produce the measured signals in **x**. Thus, matrix **A** is called the mixing matrix. Lastly, the matrix **s** contains the independent components. The dimensions of the matrices depend on the type of ICA that is being performed. Equation (1.11) indicates that each mixed signal is a weighted sum of source signals.

There are some important points about the independent components calculated using the mathematical model of ICA.

The first point is that each independent component must have unit variance [49]. The actual variance of a source signal is unknown since any scalar multiplier of a component in **s** can be cancelled by dividing the corresponding set of mixing coefficients in **A** by the same scalar multiplier. Thus, the amplitudes of the source signals are fixed by constraining the solution of equation (1.11) to produce source signals with a variance of one.

Another point is that once the independent components are calculated, only one component at most may be a Gaussian random variable [49]. A Gaussian random variable is a random variable with a Gaussian distribution. Only one component may be Gaussian because several ICA algorithms (methods of performing ICA) use non-Gaussianity as a measure of statistical independence. Non-Gaussianity is a measure of statistical independence because of the implications of a theorem known as the Central Limit Theorem. The Central Limit Theorem is exploited by ICA algorithms. The theorem states that the pdf of a sum of independent random variables becomes more Gaussian with more independent random variables included in the sum. Since mixed signals are assumed to be weighted sums of independent random variables, the Central Limit Theorem applies in ICA. In most ICA algorithms, components are computed one at a time, so the final component is simply calculated so that it satisfies equation (1.11). Hence, the final component may be more Gaussian than all the other components.

In order for all the independent components to be computed properly, the number of mixed signals must be equal to or greater than the number of independent components [50]. Otherwise, one of the source signals will contain a mixture of the remaining independent components. This situation may cause problems in most studies that use ICA because the number of independent source signals is often unknown.

1.2.4.4 Types of ICA

ICA may be used to analyze BOLD signals measured during fMRI [51]. If ICA is chosen as a method of analyzing fMRI data, there are different types of ICA that may be applied. BOLD signals are measured from different physical locations over a period of time, so spatial independence or temporal independence can be considered.

Temporal ICA is one type of ICA that may be performed on BOLD fMRI measurements [51]. An ICA algorithm will perform temporal ICA on the data if the columns in the data matrix form the BOLD signal time samples and if the rows form the voxels. When temporal ICA is used, the resulting independent components in the s matrix are time courses. When the algorithm is finished, each row of s will contain one independent component and each column will be a time sample of an independent component. When using temporal ICA, the maximum number of independent components that can be calculated is equal to the number of voxels. Each component time course will be statistically independent from all other component time courses. This can be proven by verifying equation (1.10); if component pdfs and a joint pdf were calculated using the component time samples, it can be shown that equation (1.10) would be approximately satisfied.

Another type of ICA that may be applied to BOLD fMRI measurements is spatial ICA [51]. An ICA algorithm will perform spatial ICA on the fMRI data if the columns of the data matrix form the voxels and if the rows form the BOLD signal time samples. Thus, the data matrix used in spatial ICA is the transpose of the data matrix used in temporal ICA. In spatial ICA, each independent component in the s matrix can be considered as a component brain map. Component brain maps are brain volume images that can be viewed slice-by-slice. Each voxel within the volume is assigned a weight that is calculated by the ICA algorithm [35, 52]. The weight magnitude indicates how much of an effect the corresponding component had on the BOLD signal measurement at a particular voxel [52]. Weights that have a much higher or much lower weight than the average spatial weight of the corresponding component are color-coded so they can be clearly identified. For example, weights that are two standard deviations above or below the average spatial weight may be considered significant. When spatial ICA of the BOLD signals is complete, each row of **s** forms an independent component and each column refers to a voxel [51]. When using spatial ICA, the maximum number of independent components that can be calculated is equal to the number of time samples [35]. Each component brain map shows a distribution of weights that will be statistically independent from other component brain maps with a different spatial weight distribution. Voxels with very high or very low spatial weights in one component map should have little overlap with voxels that have very high or very low weights in another component map. Lastly, in a fashion similar to temporal ICA, if component pdfs and a joint pdf were calculated using the component spatial weights, it could be shown that equation (1.10) would be approximately satisfied.

1.2.5 ICA versus Statistical Analysis Using the GLM

ICA and a statistical analysis using the GLM have important similarities and differences that are considered when both techniques are used to analyze the same fMRI data sets.

An important similarity between ICA and the GLM is that the ICA mathematical model and the GLM are both linear systems of equations [53]. The fMRI measurements are assumed to be a weighted sum of underlying signals in both types of analyses.

One important difference between ICA and a statistical analysis using the GLM is that ICA is a data-driven analysis method and a statistical analysis using the GLM is a hypothesis-driven analysis method [53]. Data-driven methods are focused on the intrinsic properties of the data. When data-driven methods are applied, there are no particular BOLD response signals that are assumed to be present in the measurements. The results from a data-driven analysis will reveal BOLD fMRI signals that can be examined for specific physiological effects. On the other hand, one or more BOLD fMRI signals are assumed to be present in the fMRI data when applying hypothesis-driven methods. A statistical null hypothesis and alternate hypothesis are also made when a hypothesis-driven method is used. These hypotheses are not present when using a data-driven method.

Another difference between the two approaches used for analyzing fMRI data is that ICA is a multivariate data analysis technique and a statistical analysis using the GLM is a univariate data analysis technique [53]. When a multivariate data analysis technique is used in fMRI, the relationships between BOLD signals measured from different voxels are considered when calculations are being made. When an ICA algorithm is executed, all voxel measurements are included in the calculations to determine each independent component. Conversely, when parameter estimates are being calculated and t-statistics or F-statistics are being assigned during a statistical analysis with the GLM, regressors in the **G** matrix are compared with BOLD signals one voxel at a time. Consequently, this is called a univariate analysis method.

Both ICA and a statistical analysis using the GLM are valuable methods for examining fMRI measurements. The methods have similarities, but they also complement one another. Interesting differences in results have been observed when ICA and statistical analyses have been performed on the same set of fMRI measurements [54].

1.2.6 The Electrical Activity of the Brain

1.2.6.1 Electroencephalography

A useful procedure for recording neural activity that occurs in the brain is electroencephalography [2]. The electroencephalograph is an instrument that is used to record the neural activity in the brain that is measurable at the scalp. The cap of an electroencephalograph has electrodes on it that are arranged in a particular manner over the cap surface. The cap is placed over a subject's head so the electrodes can come into contact with the subject's scalp. Neural activity in the brain may produce electric potentials that can be recorded at the scalp by the electrodes. The electric potentials are plotted on an electroencephalogram (EEG) [3]. Measurable electric potentials are produced as a result of ionic volume currents being generated in the extracellular regions of neurons when a substantial number of neuron action potentials are conducted simultaneously [2, 55].

The EEG is useful for diagnosing and studying different forms of epilepsy. An EEG acquired from a patient suffering from epilepsy may show ictal discharges, which are EEG signals recorded when a patient is experiencing a seizure [3]. In addition, some epileptic patients may also produce interictal discharges. Interictal discharges are abnormal neural signals that appear on an EEG that is recorded between seizures [2, 3]. Both types of discharges may be used to diagnose different types of epilepsy. However, some epileptic patients may not produce interictal discharges. Furthermore, some patients may produce interictal discharges that appear during some EEG sessions and not others. Interictal discharges may not be visible on the EEG because the discharges may be too short, too intermittent or too insignificant in amplitude [2]. Despite these shortcomings, both interictal and ictal discharges recorded on EEGs have been used to study epilepsy for several decades.

1.2.6.2 Electroencephalography and fMRI

Recently, many research groups have successfully recorded EEG and fMRI measurements simultaneously to study brain disorders like epilepsy [4, 5, 10, 25, 31, 38]. Past combined EEG-fMRI studies have shown that interictal discharges may induce hemodynamic responses. A relationship between interictal discharges and hemodynamic responses exists because interictal discharges require energy that is produced from the nutrients carried by the blood. Hemodynamic responses that are recorded shortly after interictal discharges occur have provided some insight into the regions of the brain that may be causing seizures. This has significant implications for epileptic patients that are being considered for surgery as physicians treating these patients need an accurate assessment of the locations and sizes of the abnormal brain regions. However, interictal discharges that do not have an accompanying hemodynamic response and vice versa have also been observed in epileptic patients during combined EEG-fMRI scans. Thus, there is a complex relationship between interictal discharges and hemodynamic responses.

1.2.7 Scope of the Work

The focus of this work was to design HRFs that are more closely related to a subject's own task-related or stimulus-related BOLD responses than the canonical HRF. The development of an HRF that resembles the hemodynamic response to an interictal event that occurs in the brains of patients suffering from focal epilepsy was of particular interest. The process of developing subject-specific HRFs, particularly in focal epileptic patients, has not been investigated thoroughly [4, 10].

In addition, the HRFs developed in this work were compared with the canonical HRF in terms of validity and goodness-of-fit to the data. In past studies, the quality of the regressors in the GLM has been assessed by the number of active voxels produced by using the regressors in statistical tests [48]. One set of regressors may yield a higher number of active voxels than another set, so the former is considered a "better" set of regressors. This view on the quality of the regressors in the GLM may not be correct. Hence, the quality of the regressor sets in each study of this work is assessed using various measures that will be discussed later.

Designing subject-specific HRFs was chosen as the focus of this work because several research groups have reported substantial variations in the shape of measured task-related and stimulus-related BOLD hemodynamic response signals [4, 5, 10, 16, 52, 53, 56]. Results from past studies show significant variations in relevant hemodynamic responses from one subject to another. Furthermore, hemodynamic responses have been shown to vary across different brain regions in one subject. Different stimuli have been shown to evoke hemodynamic responses with varying shapes as well. Variations in the delay and dispersion (width) of relevant hemodynamic responses are common. Using subject-specific HRFs in the statistical tests of fMRI measurements may also reveal active regions in which the signal-to-noise ratio (SNR) is low [5]. Active regions with a low SNR may not be detected by statistical tests in which non-subject-specific HRFs are used.

As a result of these findings, it is reasonable to question how well the canonical HRF resembles task-related and stimulus-related hemodynamic responses [57]. The canonical HRF is used very frequently in fMRI studies that are conducted to investigate many types of neural activity [4, 38]. In most of these studies, there are several patients for whom the canonical HRF is used as an HRF in the GLM. The canonical HRF may not account for an adequate amount of variance in hemodynamic responses from active voxels. In other words, HRFs are being misspecified. This will cause statistical test results to be invalid, inaccurate and potentially biased [32, 53].

To account for the variation in the shape of task-related and stimulus-related hemodynamic responses, the time derivative and dispersion derivative of the canonical HRF may be included as regressors in the design matrix [32]. The time derivative accounts for differences in the time-to-peak amplitude (delay) between the canonical HRF and the measured task-related or stimulus-related hemodynamic responses. The dispersion derivative accounts for differences in the positive phase width of the canonical HRF and the measured task-related or stimulus-related hemodynamic responses.

Including time and dispersion derivatives of the canonical HRF may not be adequate to account for variations between the canonical HRF and relevant hemodynamic responses. If the canonical HRF is not an accurate depiction of a subject's relevant hemodynamic responses to begin with, then including derivative waveforms may reduce the sensitivity of the statistical analysis process for detecting activations (active voxels) [10, 22]. Moreover, the time and dispersion derivatives may only account for small differences between the canonical HRF and relevant hemodynamic responses [32]. Thus, even if derivative functions are included, statistical test results may still be inaccurate.

To design new HRFs that may resemble task-related or stimulus-related hemodynamic responses more accurately, ICA was used in this work. Spatial ICA and temporal ICA were performed on fMRI measurements to identify spatial independent components and temporal independent components that may correspond to task-related or stimulus-related hemodynamic responses. After some processing of the components (described later), regressors were produced or HRFs were produced that were convolved with appropriate stimulus functions to make regressors. The regressors were placed in separate GLMs that were used in separate statistical tests of the fMRI measurements. The results of the statistical tests in which the ICA-derived regressors were used were compared with the results of the statistical tests in which the canonical HRF was used.

In the first study of this work, measurements from a block design motor control fMRI scan were acquired. A subject was asked to perform a finger flexion task in which the forefinger and thumb of the right hand were tapped together during activation periods. ICA was performed on the fMRI measurements and specific spatial and temporal components were identified and used to produce task-related hemodynamic response regressors.

The first study was used to investigate how effective ICA may be when the technique is used to generate regressors. Statistical test results from three statistical analyses were compared. One statistical analysis was performed with each of the two

ICA-derived regressors and one analysis was performed with the regressor computed using the canonical HRF. Some methods of assessing the validity of the different regressor sets and the goodness-of-fit of the GLM regressors to the data were also implemented. Study 1 was a precursor to Study 2, an important fMRI study performed on an epileptic patient.

In the second study, a continuous EEG-fMRI scan was performed on a patient suffering from partial epilepsy. The patient's EEG was recorded while fMRI measurements were acquired continuously and simultaneously. The EEG was examined after the scan and interictal events were marked. After interictal event times were noted, fMRI measurements were examined for hemodynamic responses that may have occurred shortly after the interictal events. A form of ICA that combines spatial ICA and temporal ICA was used in the fMRI measurement analysis process to identify "spatio-temporal" independent components that may resemble hemodynamic responses to interictal events. After some processing of the components, HRFs were developed and each HRF was then convolved with the corresponding stimulus function to produce regressors for the GLM. In the last step of this study, statistical test results from the statistical analyses using spatio-temporal components were compared with the statistical test results from the statistical analysis using the regressor made with the canonical HRF. In addition, the validity and goodness-of-fit of the GLM regressor sets to the data were also assessed in a similar fashion to Study 1.

The second study was important because it may have significant clinical applications for patients that suffer from partial epilepsy. Accurate assessments of the locations and sizes of brain regions in which seizures begin are important when patients are being considered for surgery. Using ICA-derived regressors in the GLM may produce more accurate localization results versus using a GLM in which regressors have been derived from a canonical HRF. Physicians can use accurate activation maps (brain maps showing active voxels) when they are performing surgeries to remove abnormal brain regions in epileptic patients. Thus, epileptic patients will have a higher chance of becoming seizure-free.

There are not many studies available that describe the production of subject-specific HRFs using ICA, especially in combined EEG-fMRI studies of patients with brain disorders. Furthermore, there are not many fMRI studies available that assess the validity of conventional HRFs. The studies in this work were conducted to investigate these two issues.

1.2.8 Thesis Organization

The remainder of this thesis contains four chapters. The methods that were used to acquire the EEG and fMRI measurements, process the images, analyze the images and compare the different regressors are described in detail in Chapter 2. In Chapter 3, the results of Study 1 and Study 2 are presented. Chapter 4 contains a detailed discussion of the results of the two studies. In the final chapter, some conclusions about the work in this thesis are presented and some future directions that can be taken with the findings are suggested.

Chapter 2

Methods

2.1 The Acquisition of fMRI Data

When fMRI scans are performed, there is a sequence of steps that must be implemented to acquire images [24]. The imaging steps are different for each type of MR image obtained. For example, there are differences in the series of steps that are used to acquire an anatomical MR image versus a functional MR image. The series of steps is called an imaging sequence.

There are a few types of imaging sequences that may be used to acquire fMR brain images from a subject [11]. The sequence used in both studies in this work is a gradient echo-planar imaging sequence (GRE-EPI). This imaging sequence is depicted in Figure 2.1 [24]. This type of imaging sequence is very popular in fMRI because it can be used to produce higher BOLD signal contrasts (differences in amplitude between induced BOLD signals from neural activity and BOLD signals from resting brain activity) than other imaging sequences that have been used for BOLD fMRI [11, 24].

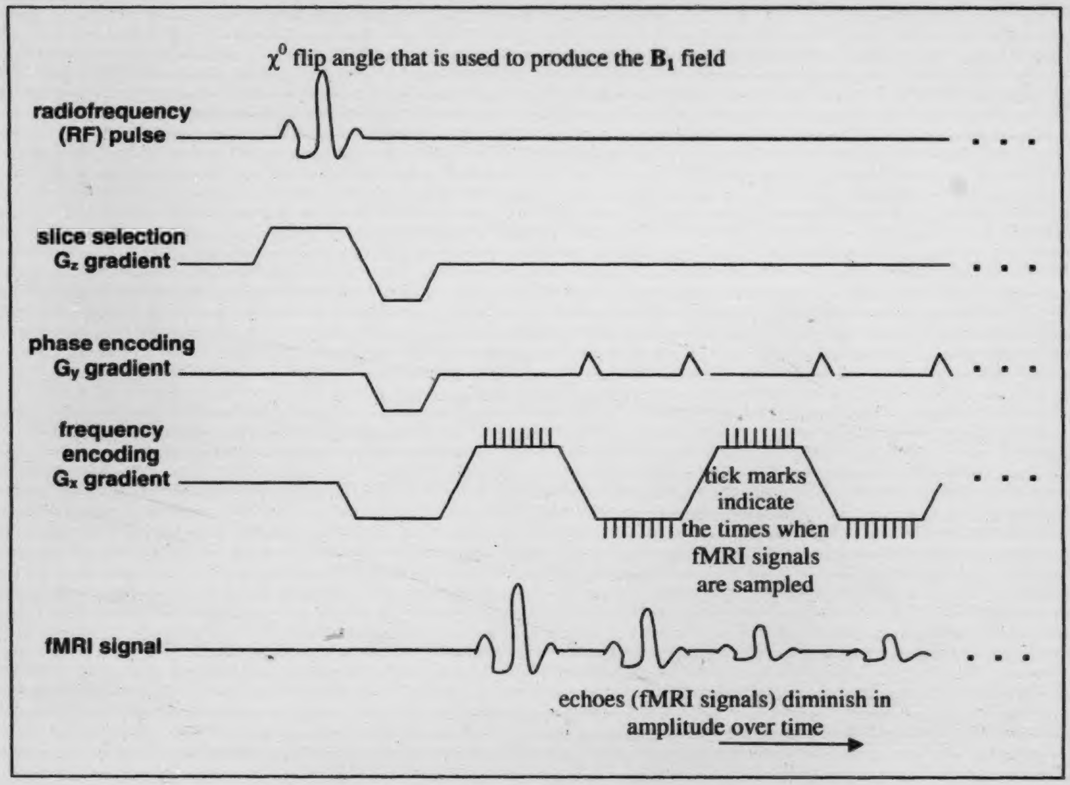
χ^0 flip angle that is used to produce the $\mathbf{B_1}$ field
radiofrequency (RF) pulse
slice selection G_z gradient
phase encoding G_y gradient
frequency encoding G_x gradient
tick marks indicate the times when fMRI signals are sampled
fMRI signal
echoes (fMRI signals) diminish in amplitude over time

Figure 2.1. Gradient Echo-Planar Imaging Sequence

The top of Figure 2.1 shows the RF pulse, which plays a very important role in an fMR imaging sequence. The pass band in the frequency domain of the RF pulse contains several different frequencies. The frequency components in the pass band are equal to the Larmor frequencies of hydrogen nuclear magnetic moments in the body region that is to be imaged [12]. When the RF pulse occurs, the $\mathbf{B_1}$ field is applied for the duration of the RF pulse. The rotating $\mathbf{B_1}$ field will place a torque on the net magnetization vector (which points in the +z-direction) in the body region being imaged. As a result, the net magnetization vector will tip toward the transverse (x-y) plane. The amount of tipping is measured by a parameter called the flip angle (Figure 2.1) [9]. The flip angle is the angle between the tipped magnetization vector and the +z-axis. The magnitude of the flip angle may be controlled by adjusting the area under the RF waveform [11]. Thus, RF waveforms are manipulated to achieve a desired magnitude of the magnetization vector in the transverse plane. The magnitude of the magnetization vector placed in the transverse plane can be calculated by measuring the horizontal component of the tipped magnetization vector [12].

During an fMRI scan, multiple RF pulses are applied [11]. One RF pulse is applied for each slice in the body region being imaged. The length of time that elapses between RF pulses that tip the magnetization vector from the same slice is known as the repetition time (TR). During one TR, multiple RF pulses are applied to acquire BOLD signals from different slices in the body region being imaged. Thus, BOLD fMRI measurements acquired from the brain during one TR are used to produce images of an entire brain volume. The brain volume can then be viewed slice-by-slice. Typical TRs range between 1-3 seconds in fMRI scans [8, 44]. In addition to the TR, there is another time parameter called the echo time (TE) that is often listed in the specifications of a GRE-EPI sequence [13, 58]. In a GRE-EPI sequence, the TE is the time that elapses between the RF pulse application and the acquisition of the BOLD signal that is at the centre of the slice being imaged [58]. The TE is not shown in Figure 2.1.

When each RF pulse occurs, a $\mathbf{G_z}$ gradient magnetic field is also applied. This gradient is also known as the slice selection gradient because it is used to select a slice in a body region where fMRI signals are acquired [12]. When the slice selection gradient is applied, the static magnetic field strength will vary along the z-axis. The static magnetic field strength varies along the z-axis because magnetic fields in addition to the original static magnetic field are implemented by the gradient. The magnetic fields implemented by the gradient can be represented by magnetic field component vectors. These component vectors are shown in red in Figure 2.2. At each location along the z-axis, the components will either be added to or subtracted from the original static magnetic field. The addition or subtraction of the magnetic field component vectors will increase or decrease the static magnetic field strength, respectively. The magnitude of the magnetic field component that is added to or subtracted from the static magnetic field depends on the location of the component along the z-axis. Since the magnetic field strength varies at different points along the z-axis, nuclear magnetic moments will precess with different Larmor frequencies along the z-axis according to equation (2.1). Equation (2.1) is an extension of equation (1.1) as the gradient magnetic field is incorporated into the Larmor frequency equation.

$$\omega(z) = \gamma(B_0 + G_z z) \qquad (2.1)$$

The variable $\omega(z)$ in equation (2.1) is the Larmor frequency of magnetic moments at a particular location on the z-axis as measured from $z = 0$. The variable G_z is the magnitude of the gradient in units of mT/metre. The variable z indicates the location of the magnetic moments along the z-axis as measured from $z = 0$. All other variables in equation (2.1) are the same as the variables in equation (1.1).

Figure 2.2 shows how the slice selection gradient varies along the z-axis according to equation (2.1). The lengths of the red arrows indicate the magnitudes of the gradient magnetic field vector components that are added to the static magnetic field at those locations relative to other locations along the z-axis. The addition of the static magnetic field component and the gradient magnetic field components is a vector addition.

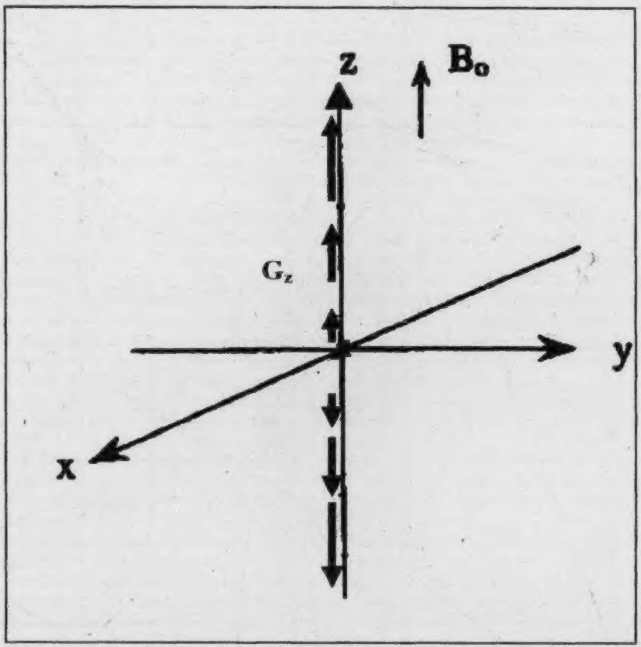

Figure 2.2. G_z Gradient Strength Variation Along the z-axis

The RF pulse that is applied while the slice selection gradient is on has a specific frequency pass band. The frequency values in this pass band are the Larmor frequencies that magnetic moments in a specific region of the body have as a result of the combination of the static magnetic field and the gradient magnetic field [12]. This specific region of the body is the region that will be imaged. Thus, the magnetization vector resulting only from the magnetic moments in this body region will be tipped from the z-axis.

The G_x and G_y gradients cause the static magnetic field to vary, in a similar manner to the G_z gradient, along the x and y-axes, respectively [11]. Equation (2.1) can be written for gradients along the x and y-axes [12]. However, there are some differences between the $\mathbf{G_x}$, $\mathbf{G_y}$ and $\mathbf{G_z}$ gradients. The $\mathbf{G_y}$ gradient, also called the phase encoding gradient, is applied for a short time prior to a $\mathbf{G_x}$ gradient implementation [11]. The phase encoding gradient causes the phases of magnetic moments in the slice being imaged to vary at different locations along the y-axis. Thus, measured BOLD signals are encoded with different phases so that their locations along the y-axis can be determined. Shortly after a phase encoding gradient is applied, a $\mathbf{G_x}$ gradient, or frequency encoding gradient, is applied. The frequency encoding gradient causes the Larmor frequencies of magnetic moments to vary along the x-axis of the slice being imaged. The frequencies of the measured BOLD signals may then be used to determine the locations along the x-axis from which the BOLD signals were measured. Figure 2.3 depicts how the gradient magnetic field components implemented by the gradient magnetic field vary along the y-axis. A similar figure can be constructed for the frequency encoding gradient.

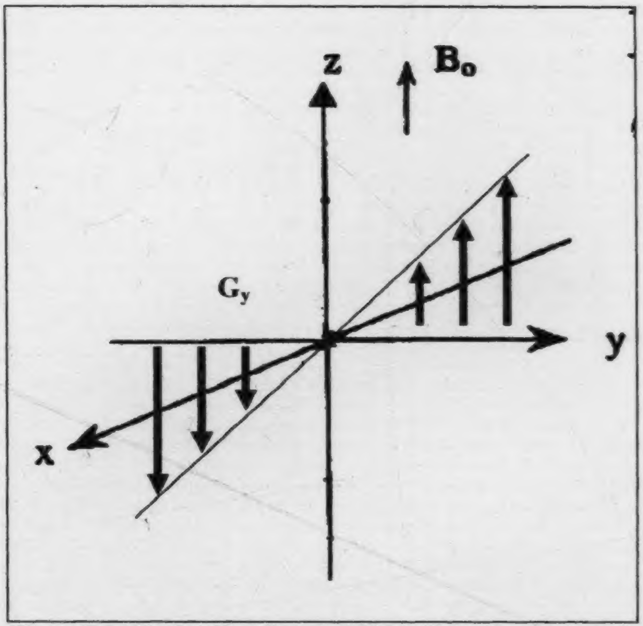

Figure 2.3. G_y Gradient Strength Variation Along the y-axis

While the frequency encoding gradient is applied, the fMRI BOLD signals are sampled as shown by the tick marks in Figure 2.1. The measured fMRI signals, also called echoes, diminish in amplitude over time because of the same factors that contribute to T_2^* signal decay [13]. Since T_2^* decay is rapid, the GRE-EPI sequence is fast so that BOLD signals with sufficient amplitude can be acquired. Images that are acquired in fMRI using GRE-EPI are T_2^*-weighted images.

2.2 The Analysis of fMRI Data

A statistical analysis of fMRI measurements involves three procedures performed in the following order [18]:

1. Preprocessing
2. Parameter estimation by multiple linear regression

3. Statistical inference

Each of these procedures was performed in this work using SPM5 and FSL 3.2β fMRI statistical analysis software. Each procedure is described in the sections that follow.

2.2.1 Preprocessing

Before the fMRI data are statistically examined for BOLD responses to a task or stimulus, the images are prepared by applying several preprocessing steps [20, 59]. The order of the steps presented below is the order in which they were performed during fMR image preprocessing in both studies of this work.

2.2.1.1 Slice Timing Adjustment

An important preprocessing step that is done on fMRI measurements is a slice timing adjustment. During a statistical test, it is assumed that BOLD signal measurements from all voxels in all slices during one particular TR (i.e. for one particular brain volume) were acquired at the same time instant [59]. This is not what happens during an fMRI scan because BOLD signals occurring at different locations in different slices are measured successively during one TR. This slice-to-slice time delay is illustrated in Figure 2.4. The brain image slices in Figure 2.4 were acquired in Study 1 of this work.

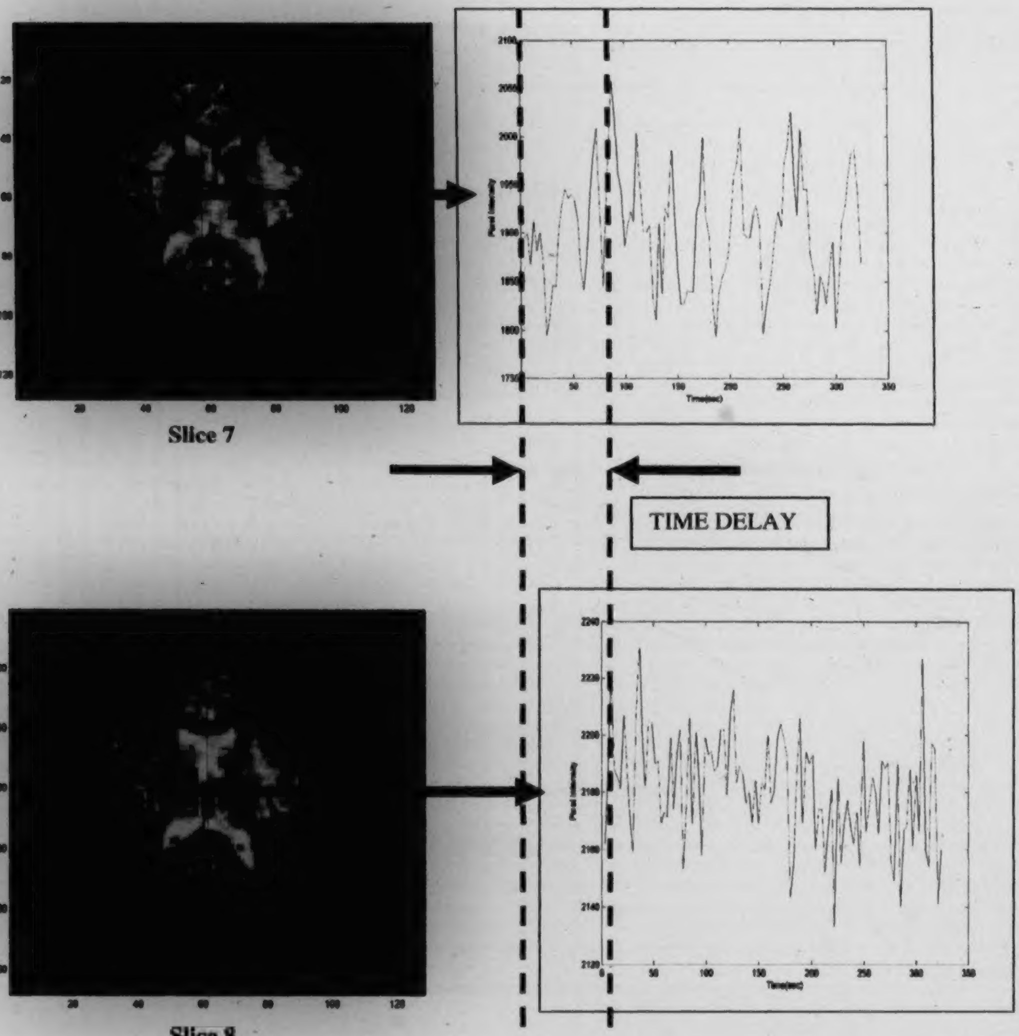

Slice 7

Slice 8

Figure 2.4. Slice Timing Difference Between Two Slices

The black square boxes in the fMR brain image slices indicate the rough locations of the voxels where the BOLD signals, shown on the right, were measured. The sizes of the boxes and, hence, the in-plane sizes of the voxels in Figure 2.4 are extremely exaggerated as the in-plane voxel dimensions are equal to the pixel dimensions in these brain images. The black boxes are large so that slice timing delays can be explained clearly. BOLD signal time samples from the top brain image slice were recorded earlier than BOLD signal time samples from the bottom slice. As a result, when the time course from each voxel is measured and displayed as shown in Figure 2.4, there is a delay between the time courses. This delay is illustrated, in an exaggerated fashion, by the time that elapses between the dashed lines.

To correct for the time delay, a slice timing adjustment is performed on the fMRI measurements [20, 32, 59]. Before a slice timing adjustment is carried out, a reference slice is chosen. The reference slice is usually the first slice in the fMRI scan [21]. The BOLD signals measured in the voxels in the reference slice are left unchanged by the adjustment procedure. During the slice timing adjustment, BOLD signals measured in voxels that are not in the reference slice are changed to account for the time delay. The magnitudes of signal samples are interpolated to what they likely would have been measured to be if all signal samples from all voxels in all slices acquired during one TR were measured simultaneously [20]. Interpolation is done using the BOLD signal samples measured from the same voxel in neighboring acquisitions (adjacent TRs) to estimate an adjusted BOLD signal value for the voxel being examined. Typical interpolation schemes used to perform slice timing adjustments are spline interpolation methods [21].

In order to do a proper statistical analysis on fMRI measurements, the regressor signal values must be compared to the corresponding BOLD signal time samples that were, effectively, recorded at the same instant [32]. This prevents the statistical results from being biased and erroneous. Hence, a slice timing adjustment is important.

2.2.1.2 Motion Correction

Head motion that may occur during fMRI scans can also cause problems during a statistical analysis [60]. Translational head motion less than 1 mm may be enough to cause undesirable changes to measured BOLD signals. Voxel sizes are very small and they are comparable to distances a subject's head may move during imaging. At the beginning of a scan, each voxel corresponds to a particular spatial location in the brain. Head motion can cause voxels to correspond to different spatial locations in subsequent acquisitions (TRs). As a result, the BOLD signal acquired from a voxel affected by head movement will fluctuate because of movement and not because there is a BOLD response due to task performance or stimulus presentation.

Cases in which movement has the most adverse effects on fMR images occur when regions lying close to tissue boundaries move [20]. For example, pixels that cover the air-tissue boundary found at the sinuses may display significant artifacts due to motion. These artifacts occur because of differences in the way that different types of matter or tissue interact with externally applied magnetic fields to produce a local magnetic field [9, 12]. The amount of distortion that an externally applied magnetic field experiences when it interacts with tissue or matter is called magnetic susceptibility. In the previous example, air and tissue have very different magnetic susceptibilities. Thus, the local magnetic fields in regions that contain air and regions that contain tissue are quite different. The difference in local magnetic field magnitudes causes magnetization vectors measured in voxels that contain air-tissue boundaries to decay rapidly. Since the magnetization vectors decay rapidly, some distortion in the brain images will occur when BOLD signals are measured from voxels at air-tissue boundaries. Motion causes even more distortion because the proportion of air and tissue changes within the voxels as a subject moves [20].

Methods are available to deal with the problems associated with head motion [60]. Software programs like SPM and FSL have procedures that rotate and translate the measured brain volumes to find a close match to a reference brain volume. To find the closest matches possible between each volume and the reference volume, the global minimum of a cost function is calculated. Typical reference volumes are the first volume acquired during the fMRI scan or the average volume of all brain volumes acquired [21]. This type of motion correction method is called a rigid body motion correction [60]. During rigid body motion corrections, differences between the reference volume and the volume being analyzed are measured along six rigid body parameters: translational movement along the x, y and z-axes as well as rotational movement about the x, y and z-axes. In SPM5, which is the software used to correct for motion in the two studies of this work, the measured differences in brain volumes are subjected to a least-squares cost function [21]. The least-squares cost function is minimized to find the optimal translations and rotations of the volumes to match the reference volume.

Unfortunately, rigid body motion correction does not remove all BOLD signal fluctuations that are caused by motion [44]. Motion may be highly correlated to the task subjects perform during an fMRI scan [60]. Voxels may be incorrectly labeled active as a result of a task or stimulus instead of being labeled active as a consequence of subject motion. This type of confound is called stimulus-correlated motion and is often observed in fMRI data after rigid body motion correction has been applied. Other motion confounds that are not adequately accounted for by rigid body motion correction are due to the fact that BOLD signal values depend on a subject's position in the MR scanner [44]. The magnetic field magnitude varies at different locations within the scanner because of static field inhomogeneities. If a patient moves within the scanner, the magnetic field may vary at different locations due to field inhomogeneities. As a result, the fMRI signal will depend on position within the scanner. Another motion confound called the spin excitation history effect is a consequence of fMRI signal dependence on subject position in the scanner. Magnetic moments tipped by RF pulses that occur early in a scan may also contribute to BOLD signals measured later in the same scan. If a magnetization vector in one region is tipped by an RF pulse and then the subject moves, BOLD signals measured while the subject is in this new position will depend on the magnetic moments tipped by the aforementioned RF pulse in addition to any new RF pulses that are applied.

Methods are available to remove motion artifacts that are not already removed by a rigid body motion correction [44, 61]. One method that is used often is the inclusion of additional regressors in the design matrix. The regressor values are equal to the rigid body movements measured (in millimetres) during the rigid body motion correction.

Additional regressors were not included in the GLMs to remove motion effects in either study of this work. This is because the subjects exhibited very little motion in all of the runs except one. Additional regressors were not included in the GLM of the run in which there was significant translational and rotational movement because the statistical test results of this run were not much different than the statistical test results of the other runs when motion confound regressors were excluded from all statistical tests. These details will be discussed later.

2.2.1.3 Brain Voxel Extraction

Non-brain tissue that is often observed in raw fMR images does not need to be present in the images when statistical analyses are performed [20]. Non-brain tissues seen in raw fMR images are often skull or scalp, which are tissues that are not involved in producing BOLD hemodynamic responses. Pixels showing non-brain tissues may be blacked out through a brain voxel extraction algorithm [62]. Pixels containing non-brain tissue often have a lower intensity than pixels containing brain tissue. One slice of an fMR brain image before brain voxel extraction is shown in Figure 2.5. The same image slice after a brain voxel extraction procedure has been performed is shown in Figure 2.6.

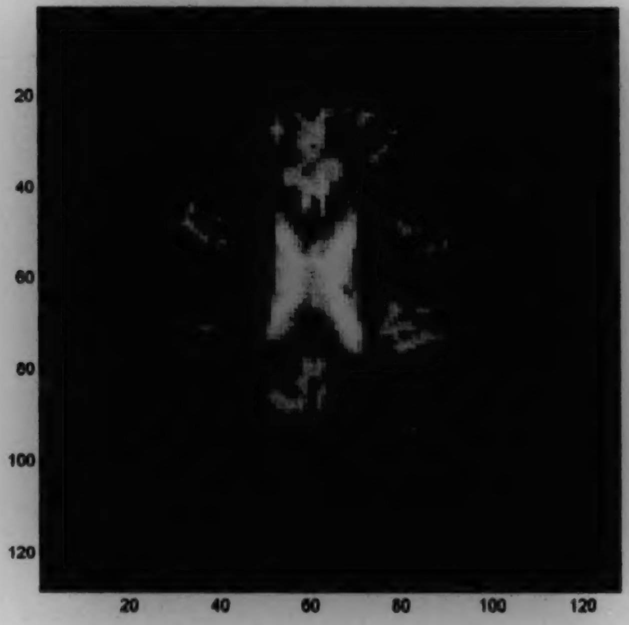

Figure 2.5. fMRI Slice that Shows Pixels Containing Non-Brain Tissue

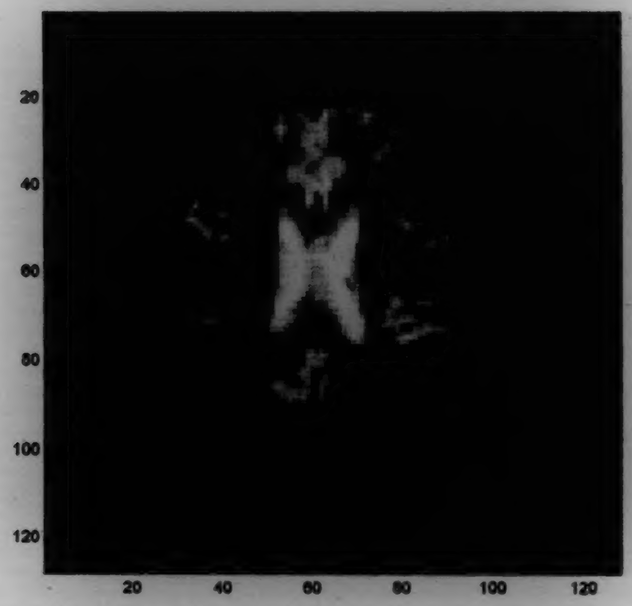

Figure 2.6. fMRI Slice in which Non-Brain Tissue is Removed

Some of the grey-colored pixels at the outer edge of the brain in Figure 2.5 are pixels containing fMRI signals from skull and scalp tissue. These pixels were blacked out by the brain voxel extraction procedure as shown by the image in Figure 2.6.

2.2.1.4 Spatial Smoothing

Spatial smoothing is another important preprocessing step [20]. When fMR images are spatially smoothed, BOLD signal measurements in each voxel are replaced with weighted averages of BOLD signal measurements acquired from neighboring voxels and from the voxel being analyzed [59]. To perform spatial smoothing, a three-dimensional signal known as a Gaussian kernel is convolved with the BOLD signal measurements. The Gaussian kernel values are weights that are multiplied by the BOLD signal measurements in the convolution operation. The size of the Gaussian kernel determines the number of neighbouring voxels that are included in the average. A parameter that indicates the size of a Gaussian kernel is called the Full Width at Half Maximum (FWHM). This parameter is measured on a Gaussian kernel by measuring the distance (in millimetres) between two points that correspond to half the kernel's peak value. As the FWHM gets larger, more voxels are included in the average to yield a smoother image. The FWHM is usually specified in millimetres along the x, y and z-axes. Common FWHM dimensions are about one to two times the dimensions of a voxel [20]. For example, the voxel dimensions of images acquired in a typical fMRI scan may be 4.0 mm x 4.0 mm x 4.0 mm. The FWHM chosen for the Gaussian kernel to smooth the images from this fMRI scan may be 8.0 mm x 8.0 mm x 8.0 mm.

Spatial smoothing is performed on fMRI measurements for several reasons. First, spatial smoothing improves the signal-to-noise ratio (SNR) in each voxel [59]. Any BOLD responses that correspond to the neural activity that occurs when subjects perform a task or experience a stimulus will increase the SNR because these BOLD responses are added together during spatial smoothing. On the other hand, noise will tend to be cancelled out by the spatial smoothing process. Noise signal magnitudes are random, so positive and negative noise measurements that are added together during spatial smoothing will diminish the noise magnitude. A higher SNR will increase statistical testing power, which is a measure of the ability of statistical tests to detect BOLD signals from truly active voxels. Another benefit of performing spatial smoothing is that the data will be converted to a form in which Gaussian Random Field Theory can be applied. Gaussian Random Field Theory will be discussed shortly. Lastly, spatial smoothing reduces the sensitivity of BOLD measurements to movement [10].

Although there are many benefits to spatial smoothing, there are also some shortcomings. Spatial smoothing reduces the spatial resolution of the fMR images significantly, which results in blurred images [11, 59, 63]. Spatial smoothing also increases the correlation between BOLD signals measured from neighbouring voxels, which is undesirable when performing a univariate statistical analysis [32, 53, 63]. Problems may also arise if the Gaussian kernel is too large or too small. If the kernel is too small, then the voxel measurements do not meet the specifications required to apply Gaussian Random Field Theory [64]. If the kernel is too large, then the ability to detect true activations (statistical power) will decline [59]. According to a theory known as the matched filter theory, the optimal kernel size is a kernel with an FWHM that is the same size as the expected active regions [15, 32, 64]. Using a kernel this size will result in optimal active region detection during the statistical analysis. Therefore, a Gaussian kernel with an FWHM equal to the size of the activated areas should be chosen to smooth the images. This principle is difficult to apply in practice because the size of the active regions is what is under investigation. The size of the kernel then depends on the anticipated size of the active regions [64].

Figure 2.7 shows a single brain image slice, acquired in Study 1, before spatial smoothing was applied. The same slice after spatial smoothing with a Gaussian kernel with an FWHM = 8.0 mm x 8.0 mm x 8.0 mm is shown in Figure 2.8. Notice that the image in Figure 2.8 has a much lower spatial resolution than the image in Figure 2.7.

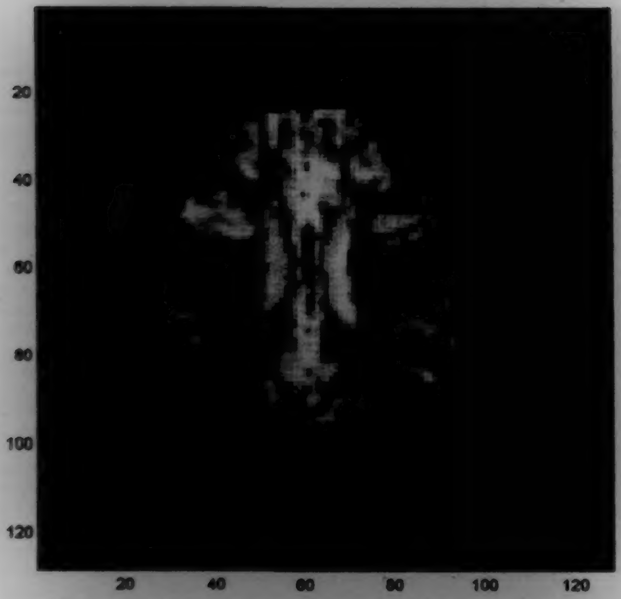
20
40
60
80
100
120
20
40
60
80
100
120

Figure 2.7. fMRI Slice Before Spatial Smoothing

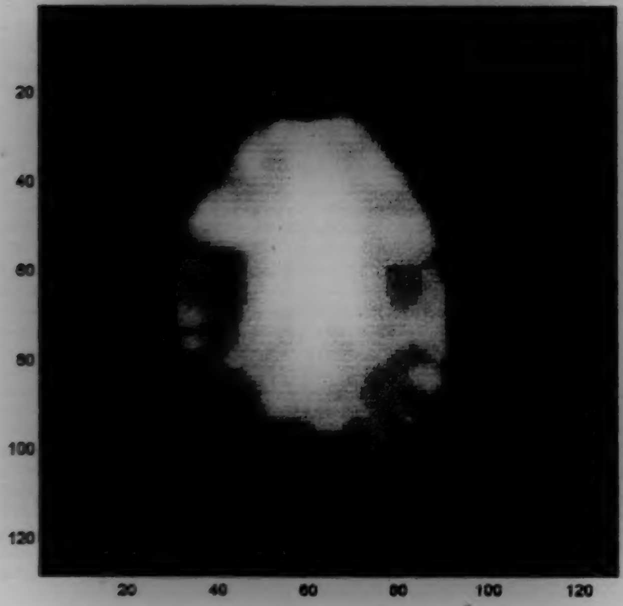
20
40
60
80
100
120
20
40
60
80
100
120

Figure 2.8. fMRI Slice After Spatial Smoothing

2.2.1.5 Temporal Filtering

In most fMR image analyses, temporal filtering is the last preprocessing step [59]. Applying temporal filtering to the fMRI data will remove noise from the images. Noise that is present in the data can dilute BOLD responses corresponding to neural activity that occurs when subjects perform a task or experience a stimulus [13].

Noise can be produced by several physiological or scanner-dependent sources. Two separate physiological effects, rhythmic cardiac pulsations and breathing, result in the appearance of undesirable low frequency signals in the data [20, 59]. A beating heart causes low frequency signals to appear in fMRI data because arterioles in the brain expand and contract at the same frequency as a beating heart [43, 65]. The changing blood flow that occurs when arterioles expand and contract causes changes in the measured BOLD signals. With regard to respiratory noise, patient breathing causes very small head movements as well as changes in blood oxygenation that are dependent on respiration instead of being dependent on neural activity [43]. Another type of noise that appears in BOLD signals is low frequency scanner drift [32]. BOLD signals might slowly drift over the course of an fMRI scan because there may be slow changes in the temperature of the scanning environment.

The physiological types of noise listed above are usually undersampled during fMRI signal acquisition [43]. These noise signals are aliased to lower frequency components according to the Nyquist theorem. The frequency range of a typical heart beat is 0.80-1.3 Hz [20]. The typical respiration rate of a human at rest is 0.10-0.30 Hz. To deal with noise caused by physiological effects, respiration and heart rate can be monitored externally during an fMRI scan using a respiration belt and pulse-oximeter, respectively [43]. Using the heart rate and respiration rate information recorded by the monitoring devices, regressors that account for physiological noise can be constructed and placed in the design matrix. Unfortunately, external monitoring devices are not always available, so a certain amount of physiological noise is expected and tolerated in the measured BOLD signals.

The most common way to deal with low frequency noise is to use a high pass filter [20, 59]. High pass filtering is done carefully because the frequency of the paradigm (the frequency of a task-rest cycle or trial) may be close to some noise frequency components in the frequency domain [59]. Inadvertently removing frequency components of BOLD signals that are related to the subject's performance of a task or experience of a stimulus by high pass filtering may have drastic consequences on the results. In most software packages such as SPM5, the signal measurements are not directly high pass filtered because this can introduce additional negative autocorrelation into the residuals. To avoid this problem, cosine functions with low frequencies are used as regressors in the design matrix. Thus, any linear combination of these cosine functions will emulate the low frequency noise terms to account for the noise.

Temporal low pass filtering may also be applied to fMRI signals to remove high frequency artifacts [59]. Low pass filtering is usually implemented with a Gaussian kernel-shaped filter similar to the ones used in spatial smoothing.

The effectiveness of low pass filtering is very controversial. One reason for the controversy is that low pass filtering reduces the power of fMRI statistical analyses [20, 59]. Since this controversy exists, direct low pass filtering of the fMRI data was not performed in the two studies of this work.

2.2.2 Parameter Estimation by Multiple Linear Regression

Once the fMRI measurements have been preprocessed, the parameters are estimated and the residual matrix (ε) values are calculated [18]. Parameters are estimated using a statistical method called multiple linear regression [15, 18]. In this work, SPM5 software was used to perform the parameter estimations and residual calculations. Thus, SPM5 software was used to "fit" the GLM to the BOLD signal measured in each voxel. The following section describes the process that is used by SPM5 to fit the GLM to each BOLD signal.

With regard to using the GLM to fit to fMRI measurements, an important point about the independence of BOLD signal time samples is considered before performing the parameter estimation. Since BOLD signals are sampled quickly during fMRI scans with TRs of 1-3 seconds, the BOLD signal samples measured from each voxel are not independent of the other samples measured from the same voxel [32, 66]. The signal samples exhibit some temporal correlation (correlation in time) with each other. Problems may arise in the statistical analyses of fMRI measurements because of the temporal correlation that exists between the samples. For instance, if some of the effects present in the BOLD signals are left unaccounted for by the GLM, such as noise or other task-related or stimulus-related BOLD responses, then the residuals from each voxel will be temporally correlated with other residuals from the same voxel [32, 48]. This correlation between residuals is called temporal autocorrelation. When the GLM is used in any statistical analysis, it is assumed that the residuals are independent [48]. Since the residuals are usually not temporally independent, adjustments are made to the parameter estimation procedure to account for temporal autocorrelation between the residuals.

Temporal autocorrelation between residuals reduces the degrees-of-freedom of the t-test or F-test [15]. Adjustments to the statistical analysis are made to account for the reduction in degrees-of-freedom. A parameter called the effective degrees-of-freedom is calculated for the t-test or F-test to account for the smaller degrees-of-freedom. Alternatively, the degrees-of-freedom may stay the same with some parameter estimation procedures, such as the parameter estimation procedure in SPM5.

SPM5 uses a method called restricted maximum likelihood (ReML) to calculate parameter estimates and residual values to fit the GLM to each BOLD signal [21]. ReML takes into account the temporal autocorrelation of residuals to obtain parameter estimates [15, 33, 67, 68].

To describe ReML, it is easiest to begin with the assumption that there is no temporal autocorrelation between the residuals. In this scenario, the residuals are independent and identically distributed (iid) [68]. When the residuals are iid, each time course of residuals (one time course of residuals is calculated for each voxel) is assumed to have a temporal mean of zero and a normal (Gaussian) amplitude distribution [36]. In addition, each residual value is assumed to be temporally independent from other residual values in the same time course. When the residuals are iid, the covariance matrix of a residual vector calculated for one voxel (i.e. a residual time course from one voxel) has the generic form shown in equation (2.2) [68].

$$\mathrm{covar}(\boldsymbol{\varepsilon}_{\mathrm{n}}) = \begin{bmatrix} s_1 & 0 & \dots & 0 \\ 0 & s_2 & \dots & 0 \\ \vdots & \vdots & \ddots & \vdots \\ 0 & 0 & \dots & s_T \end{bmatrix} \sigma_{\mathrm{n}}{}^2 = \mathbf{V}_{\mathrm{T \times T}} \sigma_{\mathrm{n}}{}^2 \qquad (2.2)$$

The variable $\boldsymbol{\varepsilon}$ is the vector of residuals from one voxel. The variable n indicates the voxel being analyzed. The square matrix **V** is the correlation matrix [33, 68]. Each entry in the **V** matrix, labeled s, along the diagonal is the variance of the signal intensities in each image 1 through T [68]. The variable T is the number of images (brain volumes) acquired, so the **V** matrix is a T x T matrix. The variable σ_n^2 is the overall noise measured in the nth voxel. The variance values along the diagonal in the covariance matrix in equation (2.2) are used to calculate the t-statistics (equation (1.6)) and F-statistics (equation (1.7)).

In the simplest case of parameter estimation, the residuals are assumed to be iid, the **V** matrix is set equal to the identity matrix (**I**) and the parameters are estimated using ordinary least-squares estimation according to a theorem known as the Gauss-Markov theorem [33]. With these assumptions, the ordinary least-squares (OLS) parameter estimates for all regressors and all voxels are given by equation (2.3).

$$\hat{\boldsymbol{\beta}}^{OLS} = \left(\mathbf{G}^T\mathbf{G}\right)^{-1}\mathbf{G}^T\mathbf{Y} \qquad (2.3)$$

All matrices in equation (2.3) are the same matrices found in the GLM (equation (1.2)). In addition, the covariance of the $\hat{\boldsymbol{\beta}}$ matrix for a single voxel n is estimated by equation (2.4). This equation is used for every voxel.

$$\mathrm{cov}(\hat{\boldsymbol{\beta}}^{OLS})_n = \left(\mathbf{G}^T\mathbf{G}\right)^{-1}\hat{\sigma}_n^{2\,OLS} \qquad (2.4)$$

Lastly, the variance of the residuals for one voxel ($\hat{\sigma}_n^2$ in equation (2.4)) is estimated using equation (2.5). In equation (2.5), **Y** and $\boldsymbol{\beta}$ are vectors (one column each) as opposed to matrices as in the GLM. The **Y** and **β** vectors contain values from the n^th^ voxel.

$$\hat{\sigma}_n^{2\,OLS} = \frac{\left(\mathbf{Y}-\mathbf{G}\hat{\boldsymbol{\beta}}^{OLS}\right)^T\left(\mathbf{Y}-\mathbf{G}\hat{\boldsymbol{\beta}}^{OLS}\right)}{\nu} \qquad (2.5)$$

The variable υ in equation (2.5) is the same degrees-of-freedom variable from the Student's t-distribution (equation (1.6)).

Since the residuals are not temporally independent in an fMRI measurement statistical analysis, the ReML estimation method is used to account for residual autocorrelation [33]. In the first step of ReML parameter estimation, the covariance of the residuals (equation (2.2)) is assumed to have a particular structure. An example structure is called the first order autoregressive model or AR(1) model [32, 33]. The details of the AR(1) model are not important to this work. Once a structure for the covariance of the residuals has been chosen, ReML is used to estimate the parameters and the covariance of the residuals [33]. The ReML method requires a significant number of calculations because it is iterative, so various simplifying assumptions are made to speed up the process. Once the covariance of the residuals has been estimated, the estimated correlation matrix, $\hat{\mathbf{V}}$, is used to decorrelate the residuals in the GLM. The decorrelation process is called whitening. The GLM (equation (1.2)), equation (2.3), equation (2.4) and equation (2.5) are all modified by the whitening process [33].

The whitened GLM is shown in equation (2.6).

$$\begin{aligned} \mathbf{V}^{-1/2}\mathbf{Y} &= \mathbf{V}^{-1/2}\mathbf{G}\boldsymbol{\beta} + \mathbf{V}^{-1/2}\boldsymbol{\varepsilon} \\ \Rightarrow \mathbf{Y}' &= \mathbf{G}'\boldsymbol{\beta} + \boldsymbol{\varepsilon}' \end{aligned} \qquad (2.6)$$

In practice, the estimated correlation matrix, $\hat{\mathbf{V}}$, is used as the **V** matrix in equation (2.6). The prime symbol (') indicates a matrix that has been whitened. The equations below are the modified equations used to estimate the parameters, parameter covariances and residuals when ReML is used. The parameter estimates are no longer ordinary least-squares estimates. Instead, the parameter estimates are called generalized least-squares (GLS) estimates.

$$\hat{\boldsymbol{\beta}}^{GLS} = \left(\mathbf{G}'^{T}\mathbf{G}'\right)^{-1}\mathbf{G}'^{T}\mathbf{Y}' \qquad (2.7)$$

$$\mathrm{cov}(\hat{\boldsymbol{\beta}}^{GLS})_n = (\mathbf{G}'^{T}\mathbf{G}')^{-1}\,\hat{\sigma}_n^{2\,GLS} \qquad (2.8)$$

$$\hat{\sigma}_n^{2\,GLS} = \frac{\left(\mathbf{Y}' - \mathbf{G}'\hat{\boldsymbol{\beta}}^{GLS}\right)^{T}\left(\mathbf{Y}' - \mathbf{G}'\hat{\boldsymbol{\beta}}^{GLS}\right)}{\nu} \qquad (2.9)$$

Once again, the **Y** and **β** vectors in equation (2.9) contain values from the n^th voxel.

2.2.3 Statistical Inference

Once the parameters of the GLM have been estimated from the BOLD signals measured from each voxel, the parameter estimates of a single regressor or a combination of parameter estimates from multiple regressors are statistically tested [30, 47, 67]. The statistical test is usually a Student's t-test or an F-test, so the parameter estimates that are tested are determined by contrast vectors according to equation (1.6) or equation (1.7), respectively. A threshold is set on the t-statistics or F-statistics to determine if the corresponding voxels are active or inactive. The process of determining active voxels from inactive voxels once a threshold is chosen is called a statistical inference [18]. With regard to the studies in this work, only Student's t-tests were performed.

When a statistical analysis of fMRI measurements is performed, there are two commonly used methods which describe the nature of the combined parameter estimation and statistical inference processes. There is the classical method and the Bayesian method [67]. With regard to this work, the classical method was used because it is simpler than the Bayesian method and it is more practical for a single subject [21, 67]. Hence, the bulk of this section focuses on the classical method. In particular, the classical method that involves the Student's t-test is discussed.

The classical method begins with the parameter estimation steps described in Section 2.2.2 [67]. The t-statistics that are calculated using the parameter estimates are assumed to be distributed according to a Student's t-distribution with a certain number of degrees-of-freedom as described in Section 1.2.3.3. t-statistic values may be converted to p-values which, under the classical method, indicate the probabilities that the parameter estimates occurred by chance. When a Bayesian method is used, p-values indicate the probabilities that the voxels were active (parameter estimates exceeded the threshold) given the acquired BOLD signal measurements.

With regard to the classical method, once the p-values are calculated, a low p-value threshold is selected to find voxels whose parameter estimates have very low probabilities of occurring by chance [67]. Hence, it can be concluded with a reasonable amount of confidence that voxels whose parameter estimate p-values are lower than the threshold are active.

A p-value may also be considered as the probability that a voxel is identified as being active when the voxel is truly inactive [22]. In other words, the p-value is the probability that the null hypothesis is falsely rejected. Hence, the p-value assigned to a parameter estimate is the probability of a false positive. The p-value can also be called the type I error rate. False positives are kept to a minimum during a classical statistical inference, which is why the p-value threshold is low.

False negatives also occur in the statistical analysis of fMRI measurements. False negatives occur when a voxel is labeled as inactive when the voxel is truly active [22, 46]. A false negative can also be called a type II error. A false negative is an incorrect acceptance of a null hypothesis. The probability of a false negative occurring is one minus the statistical power of the test. The statistical power is a measure of the probability of detecting an active voxel if the voxel is truly active as mentioned in Section 2.2.1.4 [22, 30]. Statistical power is increased by increasing the SNR of the BOLD signal measurements and by acquiring several BOLD signals from subjects while using a small number of accurate regressors in the GLM (i.e. having high degrees-of-freedom) [22, 30, 32]. Statistical power can be measured using methods such as Monte Carlo calculations [22]. Statistical power was not measured in the fMRI studies of this work because this was not the focus of the studies.

One issue that is considered during the inference stage of the statistical analysis of fMRI measurements is the multiple comparisons problem [63]. The multiple comparisons problem arises as a consequence of considering each voxel independently even though BOLD hemodynamic responses are measured from tens of thousands of voxels. Voxels in close spatial proximity to one another may show some correlation between their BOLD signals, which exacerbates the multiple comparisons problem. In a hypothetical example of an analysis of fMRI measurements, a brain volume may consist of 25, 000 voxels. If a p-value threshold (also known as an α threshold) of $\alpha \leq 0.05$ was implemented, then 1, 250 voxels (25, 000 x 0.05 = 1, 250) may be active by chance alone. This is much too high to be acceptable. This issue is called the multiple comparisons problem. The statistical analysis is modified to take the multiple comparisons problem into account.

In order to account for the multiple comparisons problem, voxels are considered in groups [63]. The probability that the parameters of task-related or stimulus-related regressors for the whole brain volume were obtained by chance (from a null Student's t-distribution) is of interest, rather than the individual probabilities that the parameter value for each task-related or stimulus-related regressor at each voxel occurred by chance. When a threshold is applied to a group of t-statistics from a statistical analysis of fMRI measurements, it is called a family-wise error rate (FWE). An FWE threshold was applied in this work.

One method of applying an FWE is called the Bonferroni correction [63]. Referring back to the hypothetical example given earlier, an α threshold was assigned to each voxel. The probability that the entire brain volume of voxels is active (i.e. all voxel p-values are less than or equal to α) is given by equation (2.10).

$$\text{Prob}\,(p \leq \alpha) = \alpha^{N} \qquad (2.10)$$

In equation (2.10), N is the total number of voxels. Given equation (2.10), the probability that none of the voxel p-values are less than or equal to α is given by equation (2.11).

$$\mathrm{Prob}(p > \alpha) = (1 - \alpha)^N \qquad (2.11)$$

Thus, the probability of obtaining at least one voxel with a p-value less than α is shown by equation (2.12). This is the FWE using the Bonferroni correction.

$$\alpha_{FWE} = 1 - (1 - \alpha)^N \qquad (2.12)$$

Since α for each voxel is small, equation (2.12) may be simplified to equation (2.13).

$$\alpha_{FWE} \approx N\alpha \qquad (2.13)$$

Regarding the hypothetical fMRI scan example, with 25 000 voxels and a desired α_{FWE} = 0.05, the α threshold for each voxel is $\alpha = 2.0*10^{-6}$ ($0.05/25\,000 = 2.0*10^{-6}$).

The Bonferroni correction is considered to be too conservative for a statistical analysis of fMRI measurements [63]. The α threshold for each voxel using the Bonferroni correction in the hypothetical example is too low. Voxels are still treated independently when a Bonferroni correction is used, so corrections to the threshold must take this into account.

Gaussian Random Field (GRF) Theory was introduced to properly correct for the multiple comparisons problem in the statistical analyses of fMRI measurements [63]. GRF Theory accounts for spatial correlation between neighbouring voxels. Groups of adjacent voxels are treated as independent units. The spatial correlation is estimated in terms of smoothness, which is expressed as the FWHM of a Gaussian kernel.

Smoothness is calculated using the correlations between residual values that are calculated during the parameter estimation step. The FWHM in this case is not the same as the FWHM of the Gaussian kernel used to spatially smooth the images. The FWHM of the smoothing estimate is used to determine the number of groups of adjacent pixels in a brain image slice that are the same size as the FWHM. These groups are called resolution elements or resels. The number of resels is used in an equation to determine an α_{FWE} threshold for the image in which groups of adjacent voxels are identified where each voxel has a t-statistic above a t-statistic threshold that is set for each voxel. The number of groups with voxels that have t-values above the threshold is the Euler characteristic (EC) of the image. The t-value threshold can be raised to decrease the EC or lowered to increase the EC. The formula in equation (2.14) is used to calculate the expected EC of an image.

$$\mathrm{E}[EC] = R(4\ln(2))(2\pi)^{-3/2} Z_t e^{-Z_t^2/2} \qquad (2.14)$$

The variable R is the number of resels and Z_t is the t-value threshold converted to a statistical z-score. The EC depends mostly on the number of resels when the brain volume is significantly larger than a resel. The expected EC corresponds to the probability of finding a group of voxels that have t-values above the t-value threshold by chance. Hence, the expected EC can be considered as the α_{FWE} for the image. The t-value threshold can be adjusted to achieve the desired α_{FWE} and correct for the multiple comparisons problem.

2.3 The Assessment of GLMs

In order to compare the different regressors that were used in the studies of this work, some statistical calculations and performance measures were computed. As mentioned in Section 1.2.7, several research groups claim that one set of regressors that is used in the GLM to fit to the data is better than another set of regressors because the former set of regressors yields a higher number of active voxels [48]. The number of active voxels is counted after two separate statistical analyses of the fMRI measurements, one analysis for each set of regressors. A set of regressors used in the GLM may be called a hemodynamic response (HR) model. A difference in the number of active voxels is not a suitable way of determining if one HR model is better than another. For this reason, calculations with various statistics and performance measures were performed on the fMRI measurements in both studies of this work.

2.3.1 Statistics Used To Compare HR Model Performance

2.3.1.1 Concurrence Ratio

The first variable used to compare the HR models is the concurrence ratio (CR) [54]. The CR is not a statistic; it is a measure that represents the agreement between the results from two different t-tests. A different HR model is used in each t-test. If most of the active voxels from the two t-tests are the same (i.e. at the same spatial locations), the CR will be high. Conversely, if the active voxels from the first t-test do not match most of the active voxels from the second t-test, the CR will be low. The formula for the CR is shown below by equation (2.15).

$$CR = \frac{number\ of\ active\ voxels\ at\ same\ location\ from\ both\ t-tests}{average\ number\ of\ active\ voxels\ from\ both\ t-tests} \quad (2.15)$$

2.3.1.2 Durbin-Watson Statistic

The second calculation used to compare the HR models is the Durbin-Watson (DW) statistic [48]. The DW statistic can be used to determine the quality of HR models by evaluating the validity of the models at each voxel. A DW statistic is calculated for every voxel in the fMR images. The Durbin-Watson statistic is calculated using the formula in equation (2.16).

$$DW = \frac{\sum_{t=2}^{n}(e_t - e_{t-1})^2}{\sum_{t=1}^{n}(e_t)^2} \quad (2.16)$$

In the DW equation, n is the number of time samples and e_t is the error (residual) at time t. To properly use the GLM in a statistical analysis, it is assumed that the residuals are temporally independent. This assumption is violated in the statistical analysis of fMRI measurements as mentioned in Section 2.2.2. The degree of temporal autocorrelation between the residuals is an indicator of the quality of the corresponding HR model. The DW statistic is a way of measuring the amount of temporal autocorrelation between the residuals, so the statistic can be used to determine the validity of HR models at each voxel.

Once the DW values have been calculated, they must be interpreted [69]. DW values are interpreted in a manner that is similar to the interpretation of t-statistics. DW values range from 0 to 4. A DW value that is equal to 2 means that there is no significant correlation between the residuals. A DW value that is less than 2 indicates that there is substantial positive correlation between residuals. A DW value that is greater than 2 indicates that there is substantial negative correlation between residuals. The DW statistic distribution approaches a normal distribution that has a mean of 2 and a variance of 4/n when a large sample size is used (i.e. a large number of voxels). However, the exact DW distribution should be used whenever possible.

In the statistical analysis of fMRI measurements, a certain amount of correlation between the residuals is expected, so an α threshold can be set on the DW values [69]. An α threshold is used because, much like t-statistics and F-statistics, DW statistics can be converted to p-values. Before calculating an α threshold, it is important to know that a DW distribution depends on the regressors being used in the design matrix. Different regressors change the DW values at different α thresholds of the DW distribution. However, there are upper and lower bounds on the DW values at commonly used α thresholds ($\alpha \leq 0.01$ or $\alpha \leq 0.05$) if the exact regressor values are unknown. If the p-value of a DW statistic falls below the α threshold, there is a certain amount of correlation between the residuals that is acceptable under the one-tailed DW test null hypothesis that there is positive correlation between the residuals. For instance, for a design matrix with 2 regressors that have 100 time samples each (one regressor being a vector of ones) and an $\alpha \leq 0.01$ threshold, the upper bound on the DW statistic is 1.562 and the lower bound is 1.522 (taken from a DW statistic table) [70]. If a DW value calculated for an arbitrary voxel is less than 1.522, there is a considerable probability of significant positive temporal autocorrelation between the residuals that cannot be tolerated [69, 70]. Conversely, if the DW value is greater than 1.562, then the probability of positive autocorrelation between the residuals is low and the null hypothesis can be rejected. If the DW value falls between 1.522 and 1.562, then the evaluation of the validity of the HR model at the randomly chosen voxel is inconclusive.

2.3.1.3 F-statistic (to Assess HR Model Performance)

After the DW test, an F-test must be done on the voxels that pass the DW test to determine if the HR model accounts for a statistically significant amount of variance in the BOLD signals measured at those voxels [48]. If the F-values exceed a threshold (i.e. the F-values are below the equivalent α threshold), then there is a high probability that the corresponding HR model explains a significant amount of data variance at those voxels. The formula for calculating the F-statistic is given by equation (2.17)(a) and equation (2.17)(b).

$$\begin{aligned} F(R^2) &= \frac{R^2 / (p-1)}{(1-R^2) / (n-p)} && (a) \\ R^2 &= \frac{SSR}{SST} && (b) \end{aligned} \qquad (2.17)$$

In equation (2.17)(b), the SSR variable is the sum of squared regressor values from the linear combination of regressors that is used to account for the BOLD hemodynamic responses. The variable SST is called the total sum-of-squares, which is the sum of squared BOLD signal values measured from one voxel. The variables n and p represent the number of time samples and the number of regressors in the design matrix, respectively. The F-score formula in equation (2.17)(a) is the ratio of the variance accounted for by the HR model to the variance not accounted for by the HR model [48]. Equation (2.17)(a) is also corrected by the two different degrees-of-freedom of an F-test: p-1 and n-p (equation (1.9)). The F-test is used because it is assumed that the F-statistic follows an F distribution with (p-1, n-p) degrees-of-freedom. The null hypothesis for this F-distribution is that the model does not explain a significant amount of variance in the data, while the alternative hypothesis is that the model does explain a significant amount of variance in the data.

2.3.1.4 Adjusted Coefficient of Multiple Determination

The final variable used to compare the HR models is the adjusted coefficient of multiple determination (R_a^2) [48]. The R_a^2 variable computes how well each model fits the BOLD signal from each voxel that passes the DW test and the F-test. This coefficient describes the amount of variance in a BOLD signal that is accounted for by the HR model. The coefficient ranges in value from 0 to 1. An R_a^2 value of 0 indicates the model does not account for any of the variance of the BOLD signal. An R_a^2 value of 1 means the model fits the signal perfectly. The formula for R_a^2 is given by equation (2.18).

$$R_a^2 = 1 - \frac{SSE/(n-p)}{SST/(n-1)} \qquad (2.18)$$

The SSE variable in equation (2.18) is the sum of squared errors (residuals) for one voxel. An HR model that has a higher R_a^2 at a given voxel is considered to be a better model.

2.4 Combined EEG-fMRI Scanning

EEG and fMRI may be successfully performed simultaneously [10, 71]. There has been a lot of interest recently in performing fMRI scans and acquiring EEGs simultaneously. Combined EEG-fMRI scans provide new information about brain activity in both healthy subjects and patients with disorders like epilepsy. This information cannot be acquired when EEG and fMRI measurements are obtained separately. A combined EEG-fMRI scan was performed on a patient suffering from partial epilepsy in the second study of this work.

EEG and fMRI have complementary advantages that are exploited in a combined EEG-fMRI scan [26, 31, 72]. Signals recorded on an EEG have a very fine temporal resolution because they are sampled with a period on the order of milliseconds. In contrast, BOLD signals from the same voxel are sampled every few seconds during an fMRI scan. However, fMRI has much better spatial resolution. Voxel dimensions are much smaller than the distances between electrodes on the cap of an electroencephalograph. Distances between electrodes are usually on the order of centimetres.

2.4.1 Continuous versus Spike-Triggered EEG-fMRI Scanning

Currently, there are two ways of performing combined EEG-fMRI scans on patients suffering from epilepsy. In both methods, interictal events that are identified on an EEG are of interest because they often result in BOLD hemodynamic responses [4, 10].

The first method is spike-triggered EEG-fMRI in which fMRI scanning commences a few seconds after interictal events are identified on the EEG [10]. Spike-triggered EEG-fMRI scans preceded continuous EEG-fMRI scans [38].

Spike-triggered EEG-fMRI scanning has several challenges [10, 38]. Spike-triggered EEG-fMRI is labour intensive because it requires careful attention to the EEG during the EEG-fMRI scanning process. Since BOLD responses do not occur after every interictal event and BOLD response time courses are not consistent in duration, it is difficult to determine an appropriate time to begin the fMRI scan after an interictal event. BOLD responses peak at different times in different patients and they peak at different times in different brain regions. Thus, if scanning begins too soon or too late, only portions of relevant BOLD responses may be measured. Moreover, it is difficult to identify interictal events as some of them may not be clearly evident on the EEG. Knowing when to stop an fMRI scan after an interictal event is also a challenge. Scanning must stop before the BOLD response settles back to baseline to avoid obtaining scans that contain baseline fMRI signals that are misconstrued as being part of the BOLD response of interest [38]. Thus, a truncated BOLD response is often acquired, which limits the study of neural activity. Another issue is that a BOLD signal acquisition cannot begin until at least 15 seconds after the completion of the previous BOLD signal acquisition. This time period is maintained to allow the tipped magnetic moments in the excited tissue to return to their original state. This prevents the contamination of subsequent signal acquisitions with magnetization vectors that were tipped in previous RF pulse applications. Lastly, in order to properly compare the interictal event-related BOLD signals with baseline BOLD signals, brain images must be acquired during periods that are free of interictal events so that baseline BOLD signals can be measured [10]. Time periods in which patients will not elicit interictal neural activity are difficult to predict.

Continuous EEG-fMRI scanning is the other form of combined EEG-fMRI scanning [10]. When continuous EEG-fMRI scanning is performed, both the EEG and fMR images are acquired continuously and simultaneously throughout the procedure. Continuous EEG-fMRI scanning overcomes the limitations of spike-triggered EEG-fMRI procedures. Since many of the shortcomings of spike-triggered EEG-fMRI scanning are not relevant to continuous EEG-fMRI scanning, continuous EEG-fMRI scanning was performed in the second study of this work

There are several artifacts in the fMRI scans and the EEG that are accounted for during processing of continuous EEG-fMRI data. The artifacts and methods of removing them are discussed in the next section.

2.4.2 Artifacts in Combined EEG-fMRI Scanning

While combining EEG and fMRI has great potential to reveal interesting information about brain activity, there are several artifacts in the fMR images and in the EEG that occur when the two methods are combined [10, 73]. These artifacts do not appear when fMR images and EEGs are acquired separately. The most significant artifacts are seen on the EEG signals.

Significant artifacts appear on the EEG due to MR gradients and RF pulses. Since closed circuit loops are part of an electroencephalograph device, rapidly changing MR gradients and RF pulses that occur during fMRI induce currents in the electrode wires [6, 10, 38]. The induced currents cause rapid amplitude fluctuations in the potentials measured by the electrodes. The amplitudes of potentials contaminated by gradient artifacts and RF pulse artifacts are much higher than the typical amplitudes of the potentials measured at the scalp.

Fortunately, there are ways of removing gradient and RF pulse artifacts [6, 10, 38]. One way of removing the artifacts is to estimate the electric potentials that are contributed by the artifacts and subtract the estimated artifact signals from the signals measured at the electrodes. Another method of removing gradient and RF pulse artifacts is to filter the artifacts out of the EEG signals. In Study 2, the gradient and RF pulse artifacts were removed using the former procedure. An average EEG signal waveform for each electrode channel was calculated and then subtracted from the corresponding EEG signal to yield EEG signals in which scanner artifacts were removed.

Another artifact that appears on EEGs is caused by subject head movements [10, 38]. EEG electrodes are very sensitive to slight head movements. Small, rhythmic head movements caused by large blood vessels moving blood along with each heart beat or by respiration are enough to induce currents in the electrodes. The induced currents generate undesirable changes in potentials. The EEG artifact caused by head movement from a beating heart is called the ballistocardiogram. Methods of removing the ballistocardiogram have been developed, which include using ICA [73].

In Study 2, average ballistocardiogram waveforms were produced from the EEG signals that were contaminated with ballistocardiogram artifacts. The average ballistocardiogram waveforms were then used to create spatial filters to remove the ballistocardiogram artifacts from contaminated EEG signals.

The electroencephalograph also has adverse effects on MR image measurements [10]. For instance, there may be a loss of MR signal strength around the electrodes. However, this artifact can actually be advantageous because it makes it easy to identify the locations of the electrodes on the MR images. Anatomical MR images are images that are more severely affected by this artifact than functional images. The artifact was not present in the functional images that were received for the second study of this work. In addition, the functional images were not registered to the anatomical images in Study 2, so the artifacts caused by the electrodes were not a problem.

2.5 The Application of ICA to fMRI Measurements

Spatial ICA and temporal ICA were applied to the fMRI measurements in both studies of this work. This section describes the steps that were completed when ICA was performed on the fMRI measurements.

2.5.1 Preprocessing

Prior to conducting ICA on the fMRI measurements, most ICA software programs will preprocess the measurements.

First, the fMRI data are subjected to the slice timing adjustment, motion correction, brain voxel extraction, spatial smoothing and temporal filtering preprocessing steps that were discussed in Section 2.2.1 [28, 74].

Next, the fMRI measurements are subjected to a process called centering [49]. In this step, the temporal mean of each mixed signal (BOLD signal measured from one voxel) is calculated and subtracted from the corresponding measured mixed signal time samples. This process centers the fluctuations of the mixed signals about zero. The means are often added back to the independent component time samples once the independent components have been calculated. Centering simplifies the independent component extraction process so the ICA algorithms can proceed quickly. An equation that describes how the ICA mathematical model is modified by the centering process is shown by equation (2.19).

$$\mathbf{x} = \mathbf{x}_0 + E\{\mathbf{x}\} = \mathbf{A}\mathbf{s} \qquad (2.19)$$

The **s**, **A** and **x** matrices in equation (2.19) are the same matrices from the ICA mathematical model (equation (1.11)). The $\mathbf{x}_0$ matrix contains the measured mixed signals that have been centered. The $E\{\}$ notation is an operator that returns the vector of expected values (temporal means) of each mixed signal.

The next preprocessing step is called whitening, which is very similar to the whitening method used to find parameter estimates (Section 2.2.2) [49]. Whitening is performed by using a technique called Principal Component Analysis (PCA), which is a signal analysis method described in the next section. Whitening decorrelates the centered mixed signals and sets the variance of each signal to one. The resulting covariance matrix of the whitened signal observations is the identity matrix. Whitening is performed to simplify the calculation of the **A** matrix. After the ICA algorithm has whitened the data, each column in the **A** matrix will be orthogonal to all the other columns. Thus, the ICA algorithm will compute the independent components much faster using whitened data. The first step in whitening is to perform an eigenvalue decomposition of the covariance matrix of the centered data matrix as shown by equation (2.20). Hence, equation (2.20) describes the PCA process.

$$E\{\mathbf{x}_0\mathbf{x}_0^T\} = \mathbf{EDE}^T \qquad (2.20)$$

The product of the $\mathbf{x_0x_0}^T$ operation is the covariance matrix. The **E** matrix contains the eigenvectors of the covariance matrix. The **D** matrix is a diagonal matrix; the eigenvalues of the covariance matrix are the values along the diagonal. The eigenvectors are the principal components of the covariance matrix. To obtain the whitened, centered mixed signal matrix, the $\mathbf{x_0}$ matrix is subjected to equation (2.21).

$$\tilde{\mathbf{x}}_0 = \mathbf{ED}^{-1/2}\mathbf{E}^T\mathbf{x}_0 \qquad (2.21)$$

The covariance matrix of the new matrix of whitened, centered mixed signals is now the identity matrix as shown by equation (2.22).

$$E\{\tilde{\mathbf{x}}_0\tilde{\mathbf{x}}_0^T\} = \mathbf{I} \qquad (2.22)$$

2.5.2 Principal Component Analysis versus Independent Component Analysis

Independent Component Analysis and Principal Component Analysis are similar methods of decomposing a set of mixed signals into component signals [15]. PCA was used to preprocess the fMRI measurements in both studies of this work.

PCA is a technique that will decompose mixed signals into a set of component signals that are statistically uncorrelated [75]. Two random variables that are uncorrelated satisfy equation (2.23) [49].

$$E\{y_1 y_2\} - E\{y_1\}E\{y_2\} = 0 \qquad (2.23)$$

In equation (2.23), y_1 and y_2 are arbitrary random variables. Equation (2.23) states that the covariance of two uncorrelated random variables is equal to 0.

Statistical independence and uncorrelatedness are related to one another [49]. Uncorrelatedness is a weak form of statistical independence [15, 49]. Random variables that are statistically independent are also uncorrelated, but uncorrelated random variables are not necessarily independent [49]. Therefore, any independent components that are estimated by ICA algorithms will also be uncorrelated, which implies that whitening the mixed signals prior to calculating independent components is a legitimate procedure.

PCA can also be used to reduce the dimensions of the data matrix [15, 49-51, 74]. Data reduction can be done using PCA because it is assumed that there are fewer independent components than time samples in spatial ICA or fewer components than voxels in temporal ICA. Principal components are used to account for the variance of the fMRI measurements. The principal components (columns of **E** matrix in equation (2.20)) are usually arranged in order of the proportions of the variance they account for in the measurements. The eigenvalues along the diagonal of the **D** matrix indicate the amount of variance accounted for by each of the eigenvectors. Some of the eigenvalues have small magnitudes, so the corresponding eigenvectors account for very little variance in the fMRI measurements. Principal components that account for very little data variance are usually discarded because it is assumed they account for noise or other unimportant effects that are present in the data [50, 75, 76]. The eigenvectors and the corresponding eigenvalues that account for a small amount of data variance can be removed from the **E** and **D** matrices, respectively, to reduce the data dimensions. By reducing the dimensions of the data matrix, the number of independent components that an ICA algorithm computes is reduced.

ICA and PCA can be illustrated using plots in an n-dimensional space where n is the number of mixed signals measured [35]. In this example, two source signals were mixed together by a mixing (**A**) matrix using an in-house MATLAB program to create two mixed signals. The values of the mixing matrix were real numbers chosen at random from Gaussian and uniform distributions. The source signals were time courses of residuals from two voxels. The residual time courses were calculated using fMRI measurements acquired during Study 2. These signals are not related, so it is assumed they are statistically independent. The source signals are plotted against one another as shown in Figure 2.9.

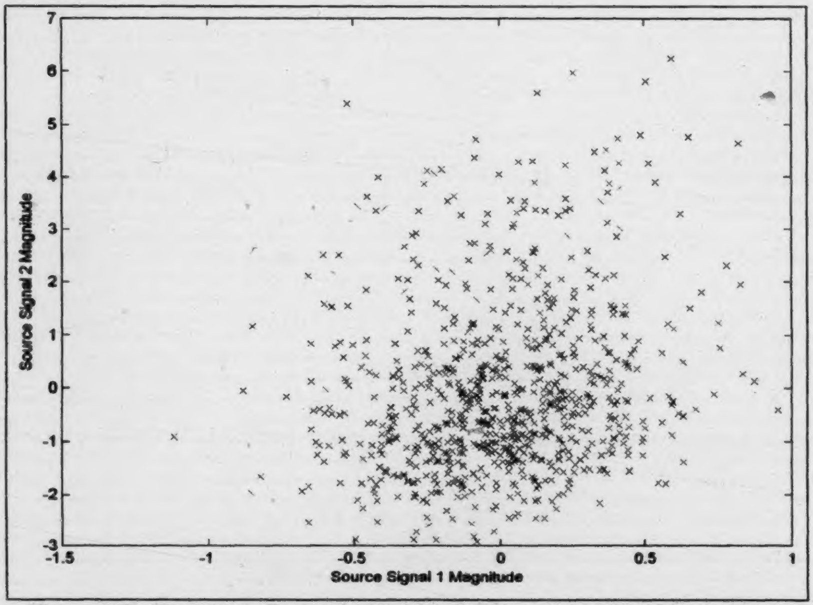

Figure 2.9. Two Time Courses of Residuals Plotted Against One Another

If source signals extracted from mixed signals are statistically independent, knowing the values of one source signal does not provide any information about the values of any other source signal in the mixture [75]. There is no apparent relationship between the two signals in Figure 2.9, so the signals appear to be statistically independent.

The signals were linearly mixed together with a known **A** matrix. The corresponding mixed signals are shown in Figure 2.10 and Figure 2.11.

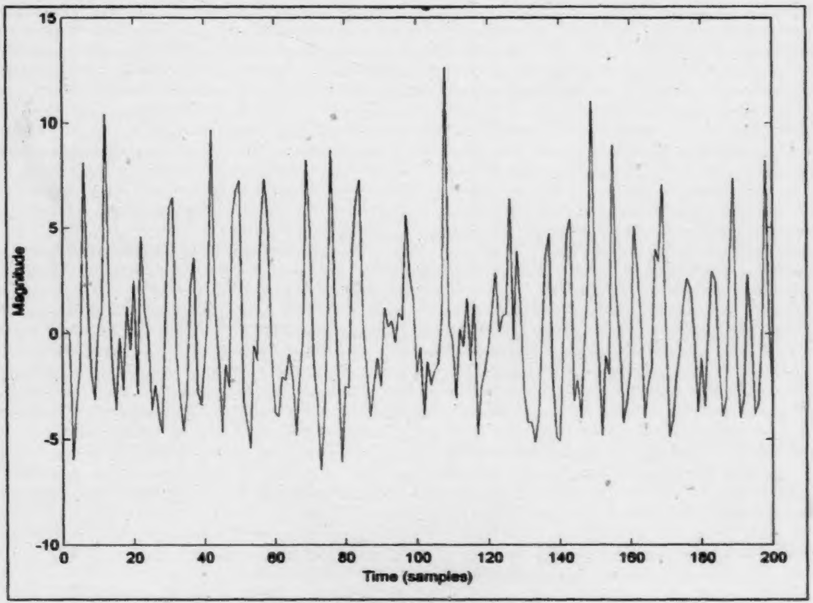

Figure 2.10. Mixed Signal 1

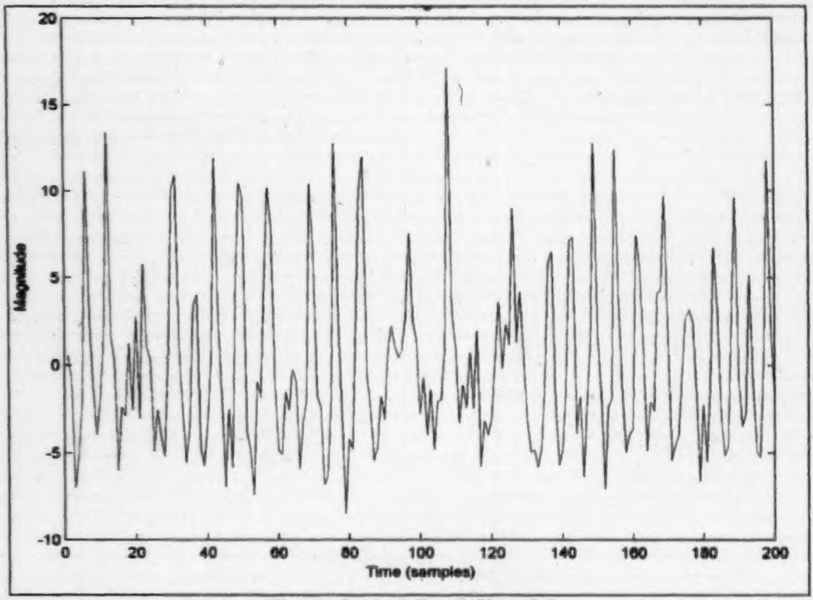

Figure 2.11. Mixed Signal 2

The mixed signals are plotted against one another in Figure 2.12 and Figure 2.13.

Both mixed signals were subjected to temporal ICA and PCA. To demonstrate the difference between PCA and ICA on plots in two-dimensional space, the mixed signals are projected onto two vectors in both PCA and ICA to produce uncorrelated and statistically independent component signals, respectively [35]. The vectors are obtained from the inverse of the **A** matrix in ICA and from the inverse of the **E** matrix in PCA. The directions of the vectors for PCA and ICA are shown in Figure 2.12 and Figure 2.13, respectively. The first principal component vector, shown in red in Figure 2.12, corresponds to the principal component that accounts for the largest amount of variance in the mixed signals. The second principal component vector, shown in green in Figure 2.12, corresponds to the principal component that accounts for the second largest amount of variance. The two principal component vectors are orthogonal to one another [35]. If there were more source signals (i.e. more dimensions), then there would be a third principal component that would account for the third largest amount of variance in the data, and so on. By contrast, the two independent component vectors shown in Figure 2.13 are oriented in different directions than the principal component vectors.

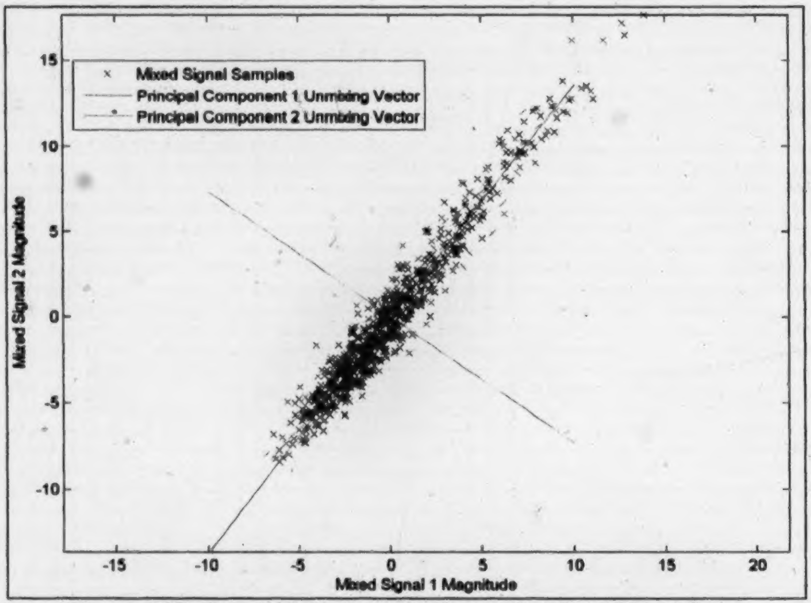

Figure 2.12. Principal Component Vectors in Mixed Signal Space

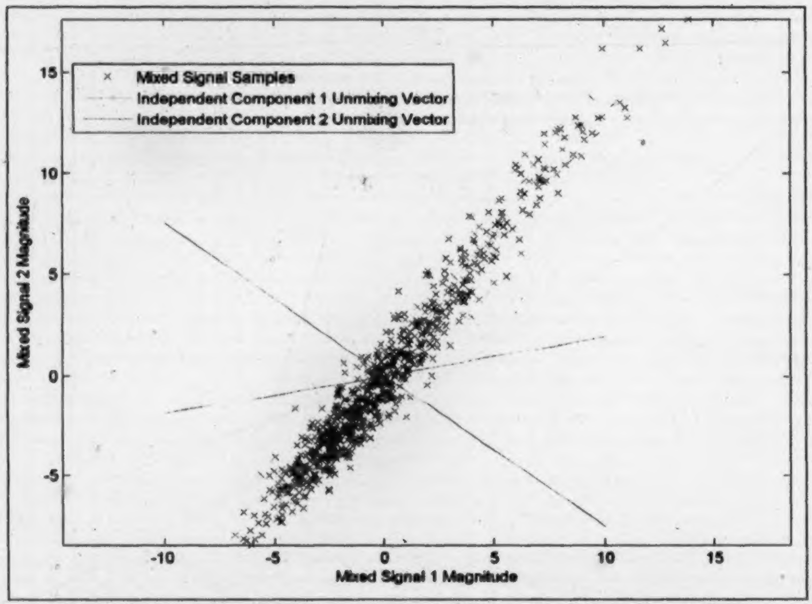

Figure 2.13. Independent Component Vectors in Mixed Signal Space

2.5.3 The Calculation of Independent Components

There are several ICA algorithms available to calculate independent components that are embedded in a set of mixed signals [77]. Two ICA algorithms were used to calculate independent components from the fMRI measurements acquired in both studies of this work. Both of these algorithms are used frequently in studies that involve ICA.

The first algorithm is called FastICA [49]. This algorithm computes independent components by finding component signals that have maximum non-Gaussianity. Non-Gaussianity is a measure of independence because of the implications of the Central Limit Theorem (Section 1.2.4.3). The first step in finding the components is to rearrange equation (1.11) to equation (2.24) shown below.

$$\mathbf{s} = \mathbf{A}^{-1}\mathbf{x} \qquad (2.24)$$

Since PCA was performed as a preprocessing step in the ICA procedure, the **A** matrix has been reduced to a square matrix. Thus, the **A** matrix is invertible, so the ICA mathematical model can be rearranged to the equation shown by equation (2.24). If the **A** matrix is not square, then a pseudoinverse of the **A** matrix may be calculated and used in equation (2.24).

The components in equation (2.24) are computed one at a time by finding the maximum non-Gaussianity of the product of each $\mathbf{A}^{-1}$ matrix row vector and the **x** matrix (projections of the mixed signals onto vectors in the $\mathbf{A}^{-1}$ matrix as described earlier). For the first iteration, the values in one row of the $\mathbf{A}^{-1}$ matrix are estimated or chosen randomly. The values of the $\mathbf{A}^{-1}$ matrix row vector are then adjusted during subsequent iterations until maximum non-Gaussianity is calculated. Each row of the $\mathbf{A}^{-1}$ matrix is calculated iteratively until all the independent components are determined. The number of independent components that is computed depends on the type of ICA. Different types of ICA are described later.

A measure of non-Gaussianity that FastICA uses is called kurtosis [49]. Kurtosis is defined by equation (2.25).

$$K(y) = E\{y^4\} - 3(E\{y^2\})^2 \qquad (2.25)$$

The variable y in equation (2.25) is a random variable. During each iteration of the FastICA algorithm, the y variable is a mixed signal that is being changed by the algorithm. When the kurtosis of the y variable is maximized, the y variable is an independent component. The kurtosis of a Gaussian random variable is equal to 0. The kurtosis of a random variable with a "spiky" pdf is greater than 0. A spiky pdf is a pdf that has high probability densities when the values of the random variable are small or large and low probability densities when the values of the random variable are intermediate. Random variables with positive kurtosis values are called superGaussian random variables. The kurtosis of a random variable with a "flat" pdf is less than 0. A flat pdf is a pdf that has approximately constant probability densities when the values of the random variable are small and low probability densities when the values of the random variable are high. In most fMRI studies, spatial independent component brain maps show small regions of voxels with high spatial weights [52]. Hence, most spatial independent components found from fMRI measurements are superGaussian.

The direct calculation of a random variable's kurtosis is difficult to perform, so an alternate method of calculating non-Gaussianity is used by FastICA [49]. Kurtosis calculations are sensitive to outliers in the data, which are measured mixed signal time samples (random variable measurements) that lie at the extremes of the signal's pdf. Outliers may be errors that could result in a poor estimate of kurtosis. To overcome this problem, a measure of non-Gaussianity called negentropy is used. Negentropy is derived from a quantity in information theory called entropy [49]. Entropy is a measure of the average uncertainty of a random variable [78]. The entropy of a continuous random variable is given by equation (2.26) [49].

$$H(y) = -\int p(y)\log\{p(y)\}dy \qquad (2.26)$$

In equation (2.26), p(y) is the pdf of the random variable y. Negentropy is calculated using equation (2.27).

$$J(y) = H(y_{gauss}) - H(y) \qquad (2.27)$$

The y_{gauss} variable is a Gaussian random variable.

Negentropy is difficult to calculate in practice [49]. Therefore, negentropy may be estimated using calculations that involve non-quadratic functions. Negentropy is approximated by the proportionality relationship given by (2.28).

$$J(y) \propto [E\{G(y)\} - E\{G(y_{gauss})\}]^2 \qquad (2.28)$$

The function G( ) is any non-quadratic function. A typical non-quadratic function is the hyperbolic tangent function. Negentropy values for Gaussian random variables are equal to 0 and negentropy values for superGaussian random variables are greater than 0.

The second ICA algorithm that was used in the studies of this work is called Infomax [79]. Infomax, much like FastICA, was developed using principles of information theory [35]. A principle of information theory known as mutual information is exploited by the Infomax algorithm. Mutual information is a measure of the dependence between random variables [49, 78]. Therefore, the mutual information between the output signals of the Infomax algorithm is minimized [79]. The output signals of the Infomax algorithm are the independent components. If the output signals of the Infomax algorithm are statistically independent from one another, the mutual information between the output signals is equal to 0. Mutual information is described by equation (2.29) [49].

$$I(y_1, y_2, ..., y_m) = \sum_{i=1}^{m} H(y_i) - H(\mathbf{y}) \qquad (2.29)$$

The y variables in equation (2.29) are random variables. During each iteration of the Infomax algorithm in which fMRI measurements are the input signals, y variables are mixed signals that are being manipulated by the algorithm. When the mutual information between the y variables is minimized, the y variables become independent components. The variable m is the total number of random variables. The $H(y_i)$ function is the entropy of a single random variable. Lastly, $H(\mathbf{y})$ is the joint entropy of the random variables. The details of the steps of the Infomax algorithm are not important to discuss in this work.

2.6 fMRI Studies

2.6.1 Study 1: Block Design Paradigm

2.6.1.1 The Task

BOLD fMRI measurements were acquired from one healthy subject during an fMRI scan performed with a block design paradigm. The fMRI scan was performed using a General Electric Sigma 3.0 T scanner (General Electric, Waukesha, WI, USA). The task the subject performed was a right handed finger flexion task. During the task portion of the scan, the subject made finger tapping movements in which the forefinger and thumb touch one another. For most of the task blocks, one finger tap was performed per second (i.e. at a 1.0 Hz rate). The subject viewed a flashing checkerboard that provided visual cues at a 1.0 Hz rate to indicate when to perform finger taps. For the remaining task blocks, the subject performed the finger tap movements at an arbitrary pace. The duration of the task period was 12 seconds followed by a rest period of 24 seconds. The fMRI scan began with the task period. This sequence was repeated nine times for a total imaging time of 5 minutes and 24 seconds. A graphical depiction of the task is shown in Figure 2.14. The task and rest periods are indicated in the figure.

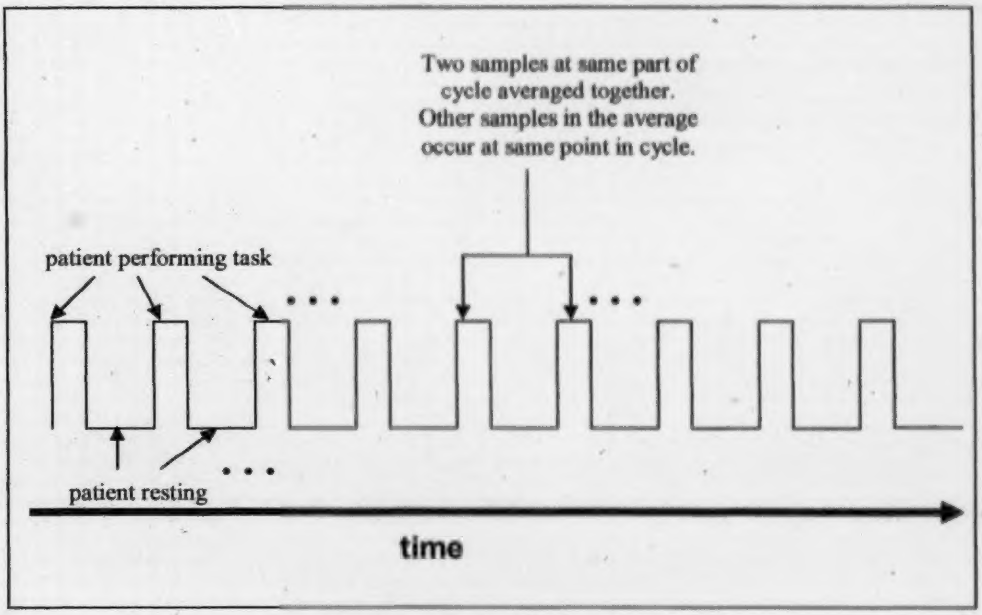
Two samples at same part of cycle averaged together. Other samples in the average occur at same point in cycle.
patient performing task
• • •
• • •
patient resting
• • •
time

Figure 2.14. Finger Flexion Block Design Paradigm

2.6.1.2 Imaging Sequence

fMR images were acquired with a GRE-EPI sequence. The GRE-EPI sequence was a two-shot sequence. In a two-shot GRE-EPI sequence, two RF pulses are required to obtain all the measurements from one slice [24, 58]. After the first RF pulse is applied, BOLD signal samples are measured from one-half of the voxels in one slice. Then a second RF pulse is applied so that the remaining half of the measurements may be acquired. Twenty slices were acquired in an interleaved fashion from the top of the head to the bottom. When interleaved sequences are used, odd (or even) numbered slices are acquired first, followed by even (or odd) numbered slices [21]. In this case, the first slice acquired at the top of the subject's head was labeled slice number 1. Hence, the interleaved slice acquisition order was 1, 3, 5, ..., 19, 2, 4, 6, ..., 20. The imaging specifications were: a total TR = 3.0s (1.5 seconds/shot), flip angle = 60^0, TE = 30 ms, field-of-view along the x-direction (FOVx) = 24 cm, FOVy = 24 cm, 5 mm slice thickness with no gap, in-plane voxel dimensions 1.875 mm x 1.875 mm and data matrix that is 96 pixels x 96 pixels zero-filled to 128 pixels x 128 pixels. Some scans at the beginning of the imaging sequence were discarded because they were acquired while the MR scanner was not in steady-state operation. Once the scanner reached steady-state operation, which often takes less than 10 seconds, the block design paradigm began. Over the entire steady-state fMRI scan, 108 volumes were acquired.

2.6.1.3 Image Preprocessing

After the fMRI measurements were acquired, the images were preprocessed. First, a slice timing adjustment was performed on the images to align the acquisition timing of the slices to the first slice (top of the head) that was acquired. The slice timing adjustment was performed using SPM5 software. Then the fMR images of each run were adjusted using a rigid body motion correction. SPM5 software was used to perform the rigid body motion correction. The reference brain volume was the first brain volume acquired in each run. After motion correction, fMRI signals from non-brain tissue were removed by performing a brain voxel extraction. The brain voxel extraction was performed using the BET tool in the FSL 3.2β software program. After this step, SPM5 was used again to spatially smooth each volume with a three-dimensional Gaussian kernel of FWHM = 8.0 mm x 8.0 mm x 8.0 mm in the x, y and z-dimensions. Lastly, the data were temporally high-pass filtered with FSL 3.2β software. The cutoff period of the high-pass filter was 120 seconds.

2.6.1.4 fMRI Measurement ICA

After the preprocessing steps were completed, temporal ICA and spatial ICA were performed on the fMRI data.

Spatial ICA was performed with the fMRI measurements from all 108 brain volumes using fMRLAB software (Swartz Center for Computational Neuroscience, San Diego, CA, USA). Spatial ICA was performed on the data to check for the presence of at least one spatial independent component that corresponds to the task paradigm. The fMRLAB software program performs spatial ICA using the Infomax algorithm [35, 52].

The spatial independent component brain maps were visually inspected to find voxels with high spatial weights in the left hemisphere motor cortex region of the brain. High spatial weights were determined by setting a threshold for the z-scores of the spatial weights. The z-score of a spatial weight is the number of standard deviations that the spatial weight is above or below the mean spatial weight of the corresponding spatial independent component [46, 52]. The formula to calculate z-scores is shown by equation (2.30).

$$z = \frac{\nu - \mu}{\sigma} \qquad (2.30)$$

In equation (2.30), υ is the value of the spatial weight, μ is the mean spatial weight for the spatial independent component being examined and σ is the standard deviation of the spatial weights of the spatial independent component being examined. The z-score threshold was chosen to be $z \geq 2.5$. This threshold score is similar to the z-score threshold used in past studies such as the study done in [52] and the study done in [28]. By visual inspection, a single spatial independent component showed an apparent relation to the motor task.

To confirm that the spatial independent component was task-related, the time course that corresponds to the spatial independent component (column of the **A** matrix in spatial ICA) was inspected. Time courses that correspond to spatial independent components often provide clues about the sources of the independent components [35, 51]. In this study, time courses of task-related spatial components should show a signal with an approximate sinusoidal shape because of the periodic nature of the task paradigm. The peaks and troughs of the time courses of the task-related spatial components should correspond to the timing of the task. There will be some delay before the task-related spatial component time courses show an increase or decrease in signal amplitude after each task block is initiated. This is because hemodynamic responses take some time to begin after the initiation of the corresponding neural activity (mentioned in Section 1.2.2.2).

To identify consistently task-related components, a correlation method developed in [35] was used. With this method, a reference signal must be calculated first. The reference signal is the canonical hemodynamic response for the block design task paradigm. The canonical hemodynamic response is the signal that results when the square wave in Figure 2.14 is convolved with the canonical impulse response in Figure 1.9. Next, the correlation coefficient was calculated between the canonical hemodynamic response and the positive region of activation (ROA+) average time course of the suspected task-related spatial component. If the task-related spatial component ROA+ average time course has a high correlation coefficient with the canonical hemodynamic response, the spatial component can be labeled as consistently task-related according to the independent component labeling method used in the study in [35]. The ROA+ average time course of a spatial component will be explained shortly. The equation for the correlation coefficient is shown by equation (2.31).

$$r_k = \frac{\sum_{i=1}^{n}(x_{ik}-\bar{x}_k)(y_i-\bar{y})}{\sqrt{\sum_{i=1}^{n}(x_{ik}-\bar{x}_k)^2}\sqrt{\sum_{i=1}^{n}(y_i-\bar{y})^2}} \qquad (2.31)$$

The variable r_k is the correlation coefficient for the kth independent component. The variable x_{ik} is the value of the ith time sample of the kth component. The variable $\bar{x}_k$ is the temporal mean of the kth independent component. The variable y_i is the value of the ith time sample of the canonical hemodynamic response y. The variable $\bar{y}$ is the temporal mean of the canonical hemodynamic response. Lastly, n is the number of time samples.

The ROA+ average time course is the time course that is computed when time courses from voxels that had spatial weights with z-scores ≥ 2.5 in a suspected task-related spatial component are averaged together. The reason the ROA+ average time course was used instead of the spatial component time course is because the ROA+ average time course is easier to obtain as an output signal from the fMRLAB software program. The ROA+ average time course and the spatial component time course are also very similar. The two time courses were found to be similar using a feature of the fMRLAB program. When spatial independent components are displayed on brain maps using the fMRLAB program, the ROA+ average time course and a "projected" spatial component time course are also displayed for each spatial component. With regard to the projected spatial component time course, each spatial independent component time course is projected onto the ROA+ voxels by multiplying the spatial component time course with the spatial weights above threshold. Then the time courses that result are averaged together to yield a "component projected onto ROA+ voxels" time course. The "component projected onto ROA+ voxels" time course accounted for 88.0% of the variance of the ROA+ average time course for the spatial independent component that was suspected of being task-related. Therefore, the two time courses are very similar and the ROA+ average time course was used to create a regressor (described later).

The spatial independent component that was suspected of being task-related was identified to be consistently task-related using the method of independent component labeling developed in [35]. The ROA+ average time course of the spatial component had a high correlation coefficient with the canonical hemodynamic response and the brain map of the spatial component showed voxels with spatial weights above the z-score threshold in the left hemisphere motor cortex region.

Once the component was identified, the fMRI measurements were averaged over the trials. Each trial lasted 36 seconds, so 12 brain volumes (i.e. 12 BOLD signal samples) were acquired during each trial. BOLD signal samples that were acquired at corresponding points in different trials were averaged together. One averaged BOLD signal time course was calculated for every voxel to generate averaged fMRI measurements. Averaging the images over the trials improves the SNR, which may produce improved statistical test results. The averaging procedure is illustrated in Figure 2.14.

Once the averaging procedure was completed, spatial ICA was performed on the averaged fMRI data. One consistently task-related spatial component was identified with the same method of component identification that was used on the unaveraged fMRI data. However, each time course was 12 time samples instead of 108. Since there were only 12 time samples, only 12 spatial independent components were computed by fMRLAB. Since independent component time courses from the averaged fMRI data were being inspected, a task-related spatial component time course was assumed to be a signal that increased and decreased with timing that corresponds to a single trial of the task paradigm. A spatial component that had high spatial weights in the left hemisphere motor cortex was selected. The correlation coefficient between this spatial component and a single period of the canonical response (i.e. the canonical response to a single neural event shown in Figure 1.9) was calculated. The ROA+ average time course and the "component projected onto ROA+ voxels" time course were essentially the same as the "component projected onto ROA+ voxels" time course accounted for 98.3 % of the variance of the ROA+ average time course

Next, temporal ICA was performed on a subset of the unaveraged fMRI data to extract one or more consistently task-related temporal independent components. This step was carried out to ensure that task-related temporal components were present in the fMRI measurements. Prior to performing temporal ICA, some adjustments were made to the data.

First, voxel measurements from slices 16 to 19 were extracted from the unaveraged data to use in temporal ICA. Temporal ICA was performed on measurements from slices 16 to 19 only because it was difficult to extract task-related temporal components from the fMRI measurements from all slices. Since this is a study of motor control, it is reasonable to assume that task-related components will most likely be calculated from BOLD signals measured in the motor cortex region. Slices 16 to 19 cover a large portion of the motor cortex region. Furthermore, the spatial ICA results revealed task-related spatial components with very high spatial weights in the motor cortex region in slices 16 to 19. Thus, slices 16 to 19 of each acquired brain volume were used in temporal ICA.

With regard to the temporal ICA process, the fMRI measurements needed to be rearranged. The fMRI measurements from slices 16 to 19 were rearranged from a four-dimensional matrix (spatial dimensions x, y, z and temporal dimension t) to a two-dimensional matrix (voxels x time). An in-house software program was built using MATLAB version 7.0 (MathWorks, Natick, MA, USA) to place the measurements in a two-dimensional matrix and to keep track of the locations of the voxels in three-dimensional space.

According to ICA theory, the maximum number of temporal components that can be computed is equal to the number of voxels. In this case, there were 9, 245 voxels in slices 16 to 19. A matrix of 9, 245 voxels x 108 time samples is too large to process using temporal ICA. Moreover, it is unnecessary to calculate 9, 245 components because most of the components will account for a very small fraction of the variance in the fMRI measurements. Thus, the data matrix was reduced in size.

To accomplish the matrix reduction, an economy singular value decomposition (svd) was performed on the fMRI data using MATLAB. An economy svd was used to produce singular values; singular values are the square roots of the eigenvalues of the data covariance matrix. An economy svd also produces spatial vectors (similar to eigenvectors) that correspond to the singular values. The singular values can be used in the exact same way as the eigenvalues to reduce the dimensions of the data matrix [66]. The economy svd computes the largest singular values and the corresponding spatial vectors up to the number of time samples within the data. This way, components that account for a large percentage of the data variance are kept and insignificant components are discarded without affecting the inherent structure of the data too severely. Hence, the data matrix that results from data reduction using an economy svd is 108 rows x 108 columns.

There is a measurement factor that limits the number of independent components that can be computed using temporal ICA. This limitation is in addition to the restriction in which the maximum number of temporal independent components that can be calculated is equal to the number of voxels. This additional restriction only has an effect on temporal ICA in this study. Improper components will be produced by the temporal ICA algorithm if the algorithm is not restricted to compute an appropriate number of components. If there is an insufficient number of BOLD time samples measured from each voxel, then the ICA algorithm breaks down and does not compute legitimate components [80]. If illegitimate component signals were computed, the signals would have very small amplitudes at nearly all time samples. At the few time samples in which the component signal amplitudes are not small, there is a sharp change in value to some maximum or minimum. The rule of thumb is to compute N temporal components so that the inequality in (2.32) is satisfied.

$$kN^2 \leq number\ of\ time\ samples \qquad (2.32)$$

The variable k is an arbitrary integer. In this study, a $k = 3$ value was chosen. The temporal ICA algorithm was constrained to produce three temporal components from the unaveraged fMRI data, so the inequality in (2.32) is satisfied ($3*3^2 = 27 \leq 108$).

This additional restriction does not affect the spatial ICA calculations in this study. Since spatial ICA requires the transpose of the **x** matrix used in temporal ICA, the inequality in (2.32) becomes the inequality in (2.33) for spatial ICA.

$$kN^2 \leq number\ of\ voxels \qquad (2.33)$$

The other restriction on spatial ICA is that the maximum number of spatial components that can be computed is limited by the number of time samples. In this study, there were 108 time samples in the unaveraged fMRI data, so the fMRLAB program only computed a maximum of 108 spatial components. Since 108 components were computed, the inequality in (2.33) is already satisfied. There is a total of 78, 087 voxels in the unaveraged fMRI data and the result calculated using (2.33) is 34, 992 ($3 * 108^2 = 34, 992 \leq 78, 087$). The inequality in (2.33) is also satisfied when spatial ICA is performed using the averaged fMRI data. There are only 12 time samples in the averaged fMRI data, and the result calculated using (2.33) is 432 ($3 * 12^2 = 432 \leq 78, 087$).

After performing an economy svd on the data matrix and taking the restrictions of temporal ICA into account, the two-dimensional data were subjected to the FastICA software program (Helsinki University of Technology, Helsinki, Finland) to compute temporal independent components.

The temporal components were then inspected to find consistently task-related temporal components. The procedure used to find consistently task-related temporal independent components was similar to the procedure used to find consistently task-related spatial independent components.

During the inspection procedure, the spatial weight vectors corresponding to the temporal components were analyzed. Just as there is a corresponding unconstrained time course for each spatial independent component when spatial ICA is performed, there is a corresponding unconstrained spatial weight vector for each temporal component when temporal ICA is performed [51]. FastICA does not have a feature that can be used to display temporal component spatial weight vectors on a brain map. In addition, fMRLAB only performs spatial ICA. Hence, a software program was built using MATLAB to display each temporal component's spatial weight vector on a crude brain map to visualize the magnitude of the spatial weights. However, z-scores were not computed for the spatial weights because visual inspection of the weights was sufficient.

One temporal independent component was identified using the procedure developed in [35]. Many of the spatial weights in the left hemisphere motor cortex region in the brain map of the selected temporal component were high. A correlation coefficient between this component and the canonical response was calculated in order to label the component a consistently task-related temporal component. The temporal component has a high correlation coefficient with the canonical response, so it is a consistently task-related temporal independent component.

In the next phase, temporal ICA was performed on the averaged fMRI data to locate one or more consistently task-related temporal independent components to use for constructing a temporal ICA-derived hemodynamic response regressor. The averaged fMRI data were rearranged into two dimensions using the MATLAB software program previously mentioned, reduced to a 12 x 12 matrix using an economy svd and then subjected to the FastICA program. Only two components were computed, which satisfies the inequality in (2.32) ($3 * 2^2 = 12 \leq 12$).

One temporal component was suspected of being consistently task-related based on visual inspection of the temporal component's corresponding spatial weight brain map. The correlation coefficient between the temporal component and one cycle of the canonical hemodynamic response is high, so the component is a consistently task-related temporal independent component.

2.6.1.5 fMRI Measurement Statistical Analyses

The next phase of this study was to build three design matrices. Three task-related regressors were placed in separate design matrices in the GLM. The first regressor that was built was the canonical hemodynamic response. This regressor is commonly used in the GLM in many types of fMRI studies, which was mentioned in Section 1.2.3.2 [4, 10, 38]. The temporal ICA-derived regressor was constructed next by concatenating the consistently task-related temporal independent component acquired from the averaged fMRI data. The temporal component was concatenated in series nine times to represent the nine trials that occurred over the entire scan. The spatial ICA-derived regressor was generated in the same manner by concatenating the ROA+ average time course that corresponds to the consistently task-related spatial component acquired from the averaged fMRI data. In addition to the task-related regressors, five regressors that are cosine signals used to high-pass filter the fMRI recordings were placed in each design matrix. A vector with all the signal values equal to 1 was included in the design matrix to account for the non-zero mean (baseline) of the BOLD signals that were measured. Regressors that account for head motion were not included in the design matrices because the subject exhibited less than 1 mm of translational motion along each spatial axis and less than 1^0 of rotational motion about each spatial axis during the scan. Each design matrix was subjected to SPM5 to build three separate GLMs.

Next, the parameters of the $\boldsymbol{\beta}$ matrix were estimated and the residuals of the $\boldsymbol{\varepsilon}$ matrix were calculated by SPM5 to satisfy the GLM equation in all three cases. A popular method of compensating for autocorrelation between the residuals by using an AR(1) model was not used in this study [32]. This is so each HR model's performance in isolation could be assessed rather than evaluating the effectiveness of methods that compensate for residual autocorrelation in combination with an HR model [48].

Once the GLMs were prepared, a Student's t-test was performed on the parameter estimates that correspond to each task-related hemodynamic response regressor. The t-test results indicate which brain regions were active in response to the task. The threshold for active voxels was set at $\alpha_{FWE} \leq 0.01$ with a contiguous active voxel extent minimum of 5 voxels. A contiguous active voxel extent minimum is the minimum number of active voxels that must be adjacent to one another in order to declare the region active. The voxel extent minimum used in this study is the same voxel extent minimum used in the study in [25]. The active voxels were determined using a very low threshold because multiple t-tests were performed. The active voxels were located and highlighted on images of transverse slices of the brain. An in-house software program generated with MATLAB was used to highlight the active voxels on the images of transverse brain slices.

2.6.1.6 HR Model Comparisons

The final stage of this study was to compare the performance of each HR model. The t-test results for each HR model were compared using the CR, DW statistics, F-statistics and R_a^2 measures that were described in Section 2.3.1. These measures were calculated using an in-house software program built using MATLAB. A DW value was calculated for the active voxels that correspond to each of the three HR models. A two-sided DW statistical test was performed because it is not known whether the residual autocorrelation is predominantly positive or negative in this fMRI study. After the DW test, F-values were calculated for the active voxels. The active voxels that had F-values above the F-value threshold of $F = 2.99$ were input to the R_a^2 formula to produce R_a^2 measures. The F-value threshold was selected from an F-statistic table [81, 82]. Finally, the HR models were compared in pairs. The quality of each HR model was assessed based on the comparisons.

2.6.2 Study 2: Event-Related Paradigm

2.6.2.1 The Events

BOLD fMR images and EEG signals were recorded from a female patient suffering from refractory right temporal lobe epilepsy. Three EEG-fMRI scans were performed in which fMRI measurements and EEG measurements were acquired continuously and simultaneously. The patient did not perform any tasks during the EEG-fMRI scans. Scans were performed using an event-related paradigm. A single interictal discharge on the EEG was an event during the scans. Each scan was referred to as a run. All runs were performed on the same day and each run was 20 minutes in duration.

A General Electric Sigma 3.0 T MR scanner and a NeuroScan MagLink RT 64-electrode EEG cap (Compumedics, El Paso, TX, USA) compatible with MRI were used to record the fMRI and EEG signals, respectively. EEG electrodes were attached to the scalp according to the International 10-20 system. A diagram of the International 10-20 system of electrode placements for the 64 electrodes is shown in Figure 2.15. The meaning of the electrode labels is not important for discussion in this work. EEG signals were sampled with a frequency of 10 kHz.

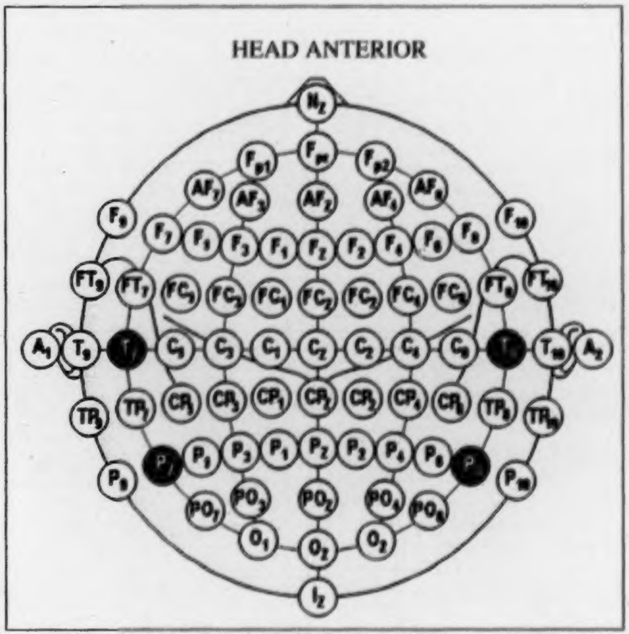

Figure 2.15. International 10-20 System of Electrode Placements

2.6.2.2 Imaging Sequence

The fMR images were acquired with a GRE-EPI sequence. Twenty-four slices were acquired in an interleaved fashion from the top of the head to the bottom. The specifications of the GRE-EPI sequence are as follows: one-shot TR = 1500 ms, TE = 30 ms, flip angle = 60 ^{0}, 5 mm slice thickness with no gap, $FOV_x = FOV_y$ = 24 cm, single slice data matrix that is 64 voxels x 64 voxels and a 3.75 mm x 3.75 mm in-plane voxel area. Some scans at the beginning of the imaging sequence were discarded because these scans were acquired before the MR scanner reached steady-state operation. After the MR scanner reached steady-state operation, 800 brain volumes were recorded in each run.

2.6.2.3 The EEG

After all measurements were acquired, the EEG was analyzed first. Gradient and RF pulse artifacts in the EEG signals were removed using NeuroScan software. The EEG signals were then decimated to a frequency of 1.0 kHz. After the decimation step, the ballistocardiogram artifacts were removed from the EEG signals. Lastly, the EEG was arranged into a standard bipolar montage by subtracting the electrode signals from one another in pre-determined reference pairs. The interictal epileptic events were marked by an epileptologist on the bipolar montage.

2.6.2.4 Image Preprocessing

Next, the fMR images were preprocessed. First, a slice timing adjustment was performed on the images of each run to align the acquisition timing of the slices to the first slice (top of the head) that was acquired in the corresponding run. The slice timing adjustment was performed using SPM5 software. Then the fMR images of each run were adjusted using a rigid body motion correction. The rigid body motion correction was performed using SPM5 software. The reference brain volume was the first brain volume acquired in each run. After motion correction, fMRI signals from non-brain tissue were removed by performing a brain voxel extraction using the BET tool in the FSL 3.2β software program. After this step, SPM5 was used again to spatially smooth each volume with a three-dimensional Gaussian kernel with FWHM = 6.0 mm x 6.0 mm x 6.0 mm in the x, y and z-dimensions. Lastly, the data were high-pass filtered with FSL 3.2β software. The cutoff period of the high-pass filter was 100 seconds.

2.6.2.5 fMRI Measurement ICA

After the preprocessing steps were completed, spatio-temporal ICA was performed on the fMRI data. Spatio-temporal ICA is a technique that combines spatial ICA and temporal ICA [83]. In this method, spatial ICA is performed on the fMRI recordings first. One or more spatial independent components are chosen based on criteria such as the locations of voxels with high spatial weights in the component brain maps and high correlation coefficients between spatial component time courses and an expected hemodynamic response time course. Time courses from voxels with high spatial weights in the chosen spatial independent component brain maps are then subjected to temporal ICA. In the last step of spatio-temporal ICA, one or more temporal components are selected as event-related components based on high correlation coefficients between the temporal components and an expected hemodynamic response.

Spatio-temporal ICA was performed on the BOLD fMRI measurements acquired from each run. The spatio-temporal ICA method used in this study is similar to the method used in [83]. An important difference between the method used in [83] and the method used in this study is that kurtosis was used as a criterion to select temporal components in [83]. An EEG was not recorded during the fMRI scans in the study in

[83], so kurtosis was used as a measure to identify potential BOLD responses that were related to interictal events. Spatio-temporal ICA was used in this study to produce spatio-temporal independent component time courses that were, after some processing, used to generate hemodynamic impulse response signals. The steps that were performed to generate the impulse responses are described later.

Spatial ICA was performed first on the fMRI measurements acquired in this study using the Group ICA of fMRI Toolbox (GIFT) program (the MIND Institute, Albuquerque, NM, USA). GIFT is a software program that operates in the MATLAB environment. The GIFT program was constrained to produce 47 spatial independent components from the run 1 measurements, 50 components from the run 2 measurements and 50 components from the run 3 measurements. The GIFT program was constrained to produce these numbers of components by using the PCA data matrix reduction technique. These numbers of spatial components are well below the limit set by (2.33). The minimum number of voxels that were analyzed in one run was 15, 899. Using (2.33), the maximum result is 7500 ($3 * 50^2 = 7500 \leq 15,899$).

Before the spatial components were examined, a canonical hemodynamic response signal was constructed by convolving the canonical impulse response signal (Figure 1.9) with a pulse train that had square wave pulses beginning when each interictal event was recorded on the EEG. The average interictal event was computed from the patient's EEG measurements to determine a suitable duration for the pulses in the stimulus function (input signal to a voxel). The duration of interictal events from past studies was also investigated to determine a suitable pulse duration. Interictal event durations can be anywhere from 20-200 ms depending on the type of interictal epileptic waveform [84]. Each pulse was given a duration of 150 ms in the stimulus function. The canonical hemodynamic response signal was used for the process of finding interictal event-related spatial independent components.

To identify spatial components that correspond to the interictal events, two criteria were used. First, correlation coefficients were calculated to describe the similarities between the canonical hemodynamic response and each time course that corresponds to a spatial independent component. Second, the spatial weight brain maps were visually inspected to find components that had high spatial weights in the right temporal lobe. Hemodynamic activity was expected in the right temporal lobe of this patient because of her epilepsy. A single component with a significant negative correlation coefficient that had high spatial weights in the right temporal lobe was identified from each run to be related to the interictal events.

Time courses from voxels that had a z-score of at least 80% of the highest z-score from the chosen spatial components were subjected to temporal ICA. This step differs from the same step in the study in [83] because only one spatial independent component from each run was chosen in this study for further examination. In the study completed in [83], voxels that had spatial weights above the z-score threshold in any of the spatial component brain maps were examined using temporal ICA.

For the temporal ICA procedure, the FastICA software program was used to calculate three temporal components from each run. Using (2.32), the maximum result is 27, so the inequality in (2.32) is satisfied ($3 * 3^2 = 27 \leq 800$). In this case of temporal ICA, however, the maximum number of temporal components that can be computed is 12 because there were time courses from only 12 voxels that were available for temporal

ICA. The two restrictions on computing maximum numbers of temporal components are explained in Section 2.6.1.4. Only three components were necessary to compute since, according to the results from the whitening preprocessing step, the eigenvalues of three components accounted for the majority of the variance in the measurements. The FastICA algorithm also had difficulty converging to a solution when it was constrained to produce 7 to 12 components.

Much like the procedure in which correlation coefficients were calculated between spatial component time courses and canonical responses, the correlation coefficients between the temporal components and their corresponding spatial component time course were calculated. The temporal independent component from each run that had the highest correlation coefficient was chosen to prepare an average patient-specific spatio-temporal ICA-derived hemodynamic impulse response.

2.6.2.6 Impulse Response Preparations

After a spatio-temporal component was chosen for each run, some processing was completed to obtain an average spatio-temporal ICA-derived hemodynamic impulse response signal that corresponds to a single interictal event. An average hemodynamic impulse response to a single interictal event was generated because interictal events mostly occurred in clusters for this patient. Different numbers of interictal events occurred at different points in each interictal event cluster, so the BOLD signals could not be averaged like the BOLD signals were averaged in Study 1. Since interictal events rarely occurred in isolation, the average BOLD response that the patient produced shortly after each interictal event was assumed to be a suitable estimate of the hemodynamic impulse response signal. In this study, it is assumed that the spatio-temporal component time courses contain BOLD signals that the patient generated shortly after she experienced interictal epileptiform activity. Therefore, a deconvolution technique was applied to the event-related spatio-temporal independent component time courses to extract a hemodynamic impulse response from each run.

For the first step in the deconvolution, the spatio-temporal components were interpolated to obtain a signal that was sampled at a rate of 1.0 kHz. Since the EEG recordings were sampled at a decimated frequency of 1.0 kHz, the spatio-temporal independent component time courses were upsampled to this frequency to perform a deconvolution. The original sampling period for the spatio-temporal component signals was the TR, which is equal to 1.5 s.

The next step in the deconvolution process was to estimate the hemodynamic impulse responses using a Wiener filter. The Wiener filter formula and its application in computing an approximate impulse response are illustrated by equations (2.34)(a) and (b) [85].

$$\begin{aligned} M(f) &= \frac{X^*(f)}{|X(f)|^2 + S_{vv}(f)/S_{hh}(f)} && (a) \\ \hat{H}(f) &= M(f)Y(f) && (b) \end{aligned} \qquad (2.34)$$

In equations (2.34)(a) and (b), the variable f is the frequency value. The function M(f) in equation (2.34)(a) is the frequency spectrum (Fourier transform) of the Wiener filter. The function X(f) is the frequency spectrum of the interictal event pulse train signal and the asterisk (*) denotes the complex conjugate of X(f). The signal S_{vv}(f) is the estimated power spectrum for white noise. The function $\hat{H}(f)$ in equation (2.34)(b) is the estimated frequency spectrum of the impulse response. In order to calculate $\hat{H}(f)$, an estimate of the power spectrum of $\hat{H}(f)$ is required. The estimated power spectrum of $\hat{H}(f)$ is the function $S_{hh}(f)$. The function Y(f) in equation (2.34)(b) is the (approximate) frequency spectrum of the event-related spatio-temporal independent component.

If white noise is not present in the fMRI measurements, the right side of equation (2.34)(a) reduces to Y(f)/X(f). Hence, the whole process of estimating the impulse response becomes a direct deconvolution as shown by equation (2.35).

$$\hat{H}(f) = \frac{Y(f)}{X(f)} \qquad (2.35)$$

A direct deconvolution is not feasible for this study. Some of the magnitudes of the frequency components in the X(f) frequency spectrum are equal to 0 or very close to 0. Division by frequency components with really small magnitudes results in extremely large frequency component magnitudes in the $\hat{H}(f)$ frequency spectrum. The resulting impulse response computed by performing an inverse Fourier transform on the $\hat{H}(f)$ frequency spectrum has invalid values.

The Wiener filter method was used to obtain impulse response signals. The $S_{vv}(f)/S_{hh}(f)$ term in equation (2.34)(a) prevents the denominator from approaching zero, resulting in a much smoother estimate of the impulse response. The $S_{vv}(f)$ power spectrum is given a constant magnitude of 10, 000 over all frequencies. The $S_{hh}(f)$ function used in equation (2.34)(a) is the normalized power spectrum of the canonical impulse response. The normalized power spectrum of the canonical impulse response is used as the $S_{hh}(f)$ signal because it is expected that the estimated impulse responses will have pass band frequency spectra that are somewhat similar to the canonical impulse response frequency spectrum. The power spectrum of the canonical impulse response is shown in Figure 2.16.

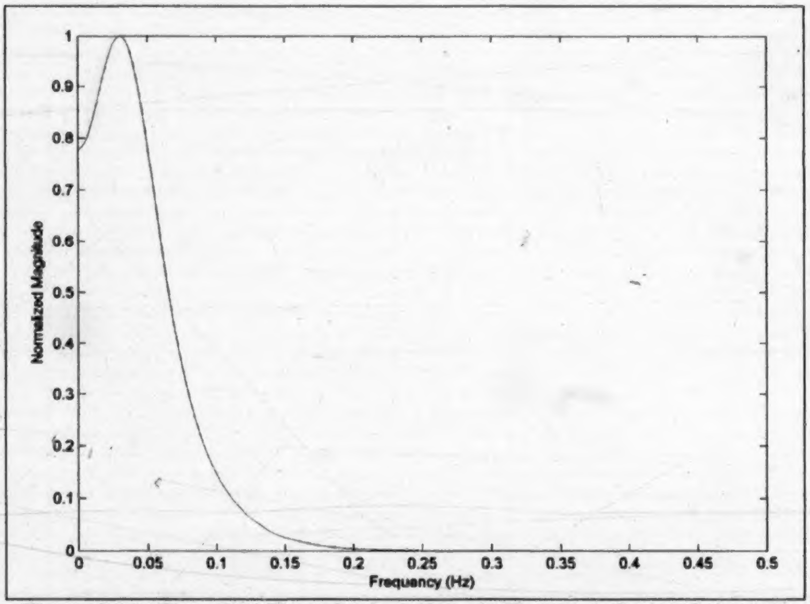

Figure 2.16. Canonical Hemodynamic Impulse Response Power Spectrum

The values chosen for the $S_{vv}(f)/S_{hh}(f)$ ratio resulted in an appropriate magnitude spectrum for M(f). The M(f) function that was designed and used in equations (2.34)(a) and (b) produced a $\hat{H}(f)$ frequency spectrum with a pass band that is similar to the canonical impulse response frequency spectrum pass band.

The last step in the deconvolution process used to prepare the spatio-temporal ICA-derived impulse responses was to smooth the frequency spectra of the impulse responses using a Hamming window. Smoothing was necessary to remove oscillations that are in the impulse response signals in the time domain. The oscillations are present because of small magnitude frequency components that remain in the frequency spectra of the spatio-temporal ICA-derived impulse responses after Wiener filtering. The canonical impulse response spectrum is smooth, so the spatio-temporal ICA-derived hemodynamic impulse response spectra should be smooth as well.

Hamming windows of various sizes were tested to find optimal impulse responses. The first step in testing different Hamming windows was to obtain impulse responses from spectra that were smoothed with different Hamming windows. Impulse responses in which the signal amplitudes approach zero in the time domain at about 30 seconds were optimal since the canonical impulse response lasts about 30 seconds. The spatio-temporal ICA-derived impulse responses that were produced by smoothing with various Hamming windows were convolved with the pulse train event signal from the corresponding run to produce spatio-temporal ICA-derived hemodynamic responses. The spatio-temporal ICA-derived hemodynamic responses were compared with the spatio-temporal independent component time courses to find hemodynamic responses with BOLD signal changes that were concordant with the interictal event-related BOLD signal changes in the spatio-temporal component time courses. The optimal Hamming window size was 133 points as shown in Figure 2.17.

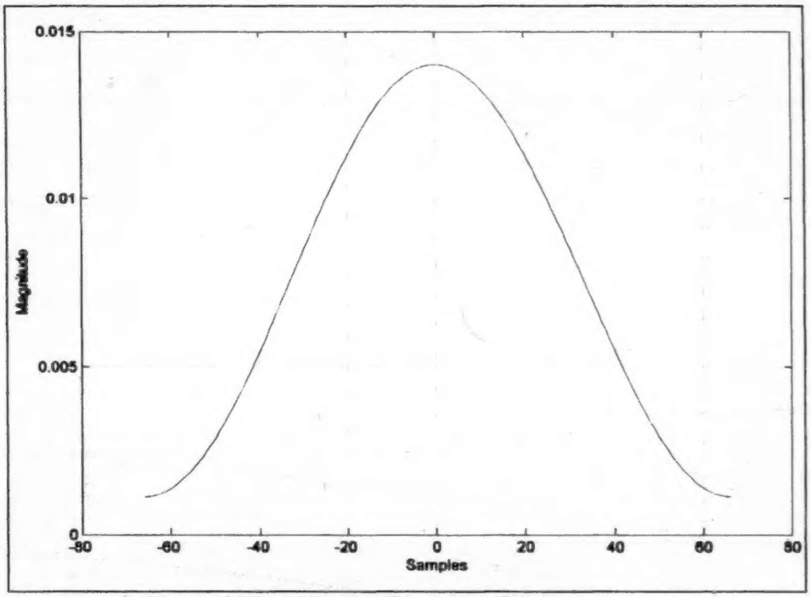

Figure 2.17. 133-point Hamming Window

2.6.2.7 fMRI Measurement Statistical Analyses

Next, hemodynamic response model regressors were constructed for each run. The spatio-temporal ICA-derived hemodynamic response regressors are the signals that resulted from the convolution of the optimal spatio-temporal ICA-derived impulse response from each run with the corresponding interictal event pulse train. After the convolution, the spatio-temporal ICA-derived hemodynamic responses were decimated to signals that have a sampling rate of 0.67 Hz (equivalent to a TR of 1.5 s). Decimation was performed so that regressors with 800 time samples could be placed in separate design matrices.

Canonical hemodynamic response regressors for each run were also constructed and placed in separate design matrices. Since the interictal event-related spatio-temporal independent components show negative BOLD responses, some unexpected additional steps were added to this study. The canonical hemodynamic response signal values for each run were multiplied by -1 (i.e. the canonical responses were inverted) to obtain negative canonical hemodynamic responses to use as regressors in GLMs for three additional statistical tests on the fMRI measurements. Hence, there were six canonical responses that were generated in total: one canonical response with positive values and one canonical response with negative values for each of the three runs.

In addition, 24 cosine function regressors were placed in all of the design matrices. The cosine functions were used to high-pass filter the fMRI signals by removing frequency components that had periods longer than 100 s. Lastly, a vector with all the signal values equal to 1 was included in each design matrix to account for the non-zero mean (baseline) of the BOLD signals that were measured. Regressors that account for head motion were not included in the design matrices because the patient exhibited less than 1 mm of translational motion along each spatial axis and less than 1^0 of rotational motion about each spatial axis during runs 1 and 2. In run 3, the patient moved her head a maximum of 4 mm along one of the axes and rotated her head a maximum of about 1.75^0 about one of the axes. However, in this case the activation maps are not very different from run-to-run when motion confound regressors are excluded from all the statistical tests. Thus, motion confound regressors were excluded from the design matrices corresponding to run 3.

Each design matrix was subjected to SPM5 software to build separate GLMs. The parameters were estimated and the residuals were calculated for the GLMs using SPM5. The popular method of compensating for autocorrelation between the residuals by using an AR(1) model was not used in this study [32]. This is so each HR model's performance in isolation could be assessed rather than evaluating the effectiveness of methods that compensate for residual autocorrelation in combination with an HR model [48].

Once the GLMs were prepared, Student's t-tests were performed on the parameter estimates that correspond to the interictal event-related regressors, the canonical hemodynamic response regressors and the inverted canonical hemodynamic response regressors. The t-test results indicate which voxels were active in response to the interictal events. The threshold for active voxels was set at $\alpha_{FWE} \leq 0.01$ with a contiguous active voxel extent minimum of 5 voxels. The voxel extent minimum used in this study is the same voxel extent minimum used in the study in [25]. The active voxels were determined using a very low threshold because multiple t-tests were performed. The active voxels were located and highlighted on transverse slice images of the brain using an in-house program generated with MATLAB.

2.6.2.8 HR Model Comparisons

The final stage of this study was to compare the performance of each HR model. The t-test results for each HR model were compared using the CR, DW statistics, F-statistics and R_a^2 measures that were described in Section 2.3.1. These measures were calculated using an in-house software program that was built using MATLAB. A DW value was calculated for the active voxels corresponding to each of the HR models. A two-sided DW statistical test was performed because it is not known whether the residual autocorrelation is predominantly positive or negative in this fMRI study. After the DW test, F-values were calculated for the active voxels. The active voxels that had F-values above the F-value threshold of F = 1.80 were input to the R_a^2 formula to produce R_a^2 measures. The F-value threshold was selected from an F-statistic table [81, 82]. Finally, the HR models were compared and the quality of each HR model was assessed based on the comparisons.

Chapter 3

Results

3.1 Study 1: Block Design Paradigm

3.1.1 Regressor Preparations

After the fMRI measurements were acquired and preprocessed, spatial ICA was performed on the unaveraged fMRI data first. One consistently task-related spatial independent component was found.

Figure 3.1 is the consistently task-related spatial component brain map. Voxels with spatial weight z-scores of $z \geq 2.5$ (the z-score threshold) are shown in red and yellow in Figure 3.1 and voxels with spatial weight z-scores ≤ -2.5 are shown in blue. The legend of the brain map is shown at the right of the brain map. There are several voxels in the left hemisphere motor cortex region that have high spatial weights. There are a few small regions in the supplementary motor cortex and ipsilateral cerebellum that have high spatial weights as well. However, the spatial weights in the supplementary motor cortex and cerebellum are not as high as those in the motor cortex region. There are very few small regions that have negative spatial weights. These regions were ignored.

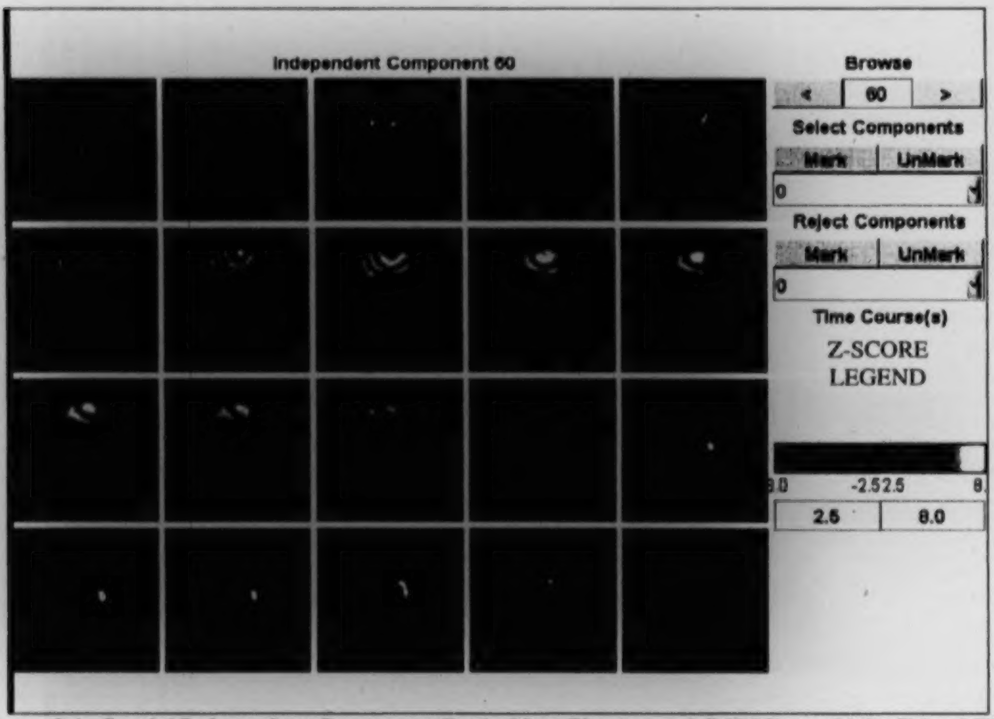
Independent Component 60
Browse
<
60
>
Select Components
Mark
UnMark
0
Reject Components
Mark
UnMark
0
Time Course(s)
Z-SCORE
LEGEND
-2.52.5
2.5
8.0

Figure 3.1. Spatial Independent Component Brain Map (Unaveraged fMRI Data; Right Side of Slice is Left Side of Brain and Bottom of Slice is Anterior of Brain)

Figure 3.2 is the ROA+ average time course for the spatial component computed using the unaveraged fMRI measurements. This time course shows a sinusoid-shaped signal. The amplitudes of peaks and troughs are not constant across trials. The peak per cent increase in amplitude of the signal relative to the average signal amplitude in voxels that have a weight greater than $z = 2.5$ is nearly 1 % and the peak per cent decrease in amplitude relative to the average signal amplitude in voxels that have a weight less than $z = 2.5$ is -0.66 %. The per cent signal amplitude changes were calculated using fMRLAB. The correlation coefficient between the ROA+ average time course and the canonical response is 0.79. This correlation coefficient is considered to be sufficiently high.

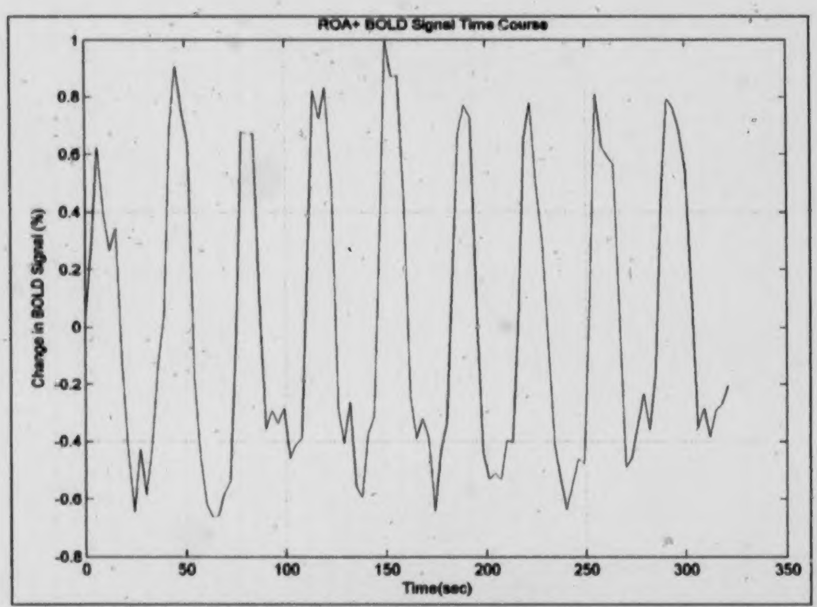

Figure 3.2. ROA+ BOLD Signal Time Course for Task-Related Spatial Independent Component (Unaveraged fMRI Data)

The spatial independent component brain map acquired using the averaged fMRI measurements is shown in Figure 3.3. The spatial weights are high in locations that are similar to the locations of high spatial weights in Figure 3.1. However, there are some differences. There are some regions that have spatial weights greater than z = 2.5 in the occipital/parietal lobe regions and one region that has spatial weights less than z = -2.5 in the parietal lobe region. These regions are not highlighted in the brain map of the spatial component found using the unaveraged fMRI measurements. Once again, voxels that had spatial weights less than z = -2.5 were ignored.

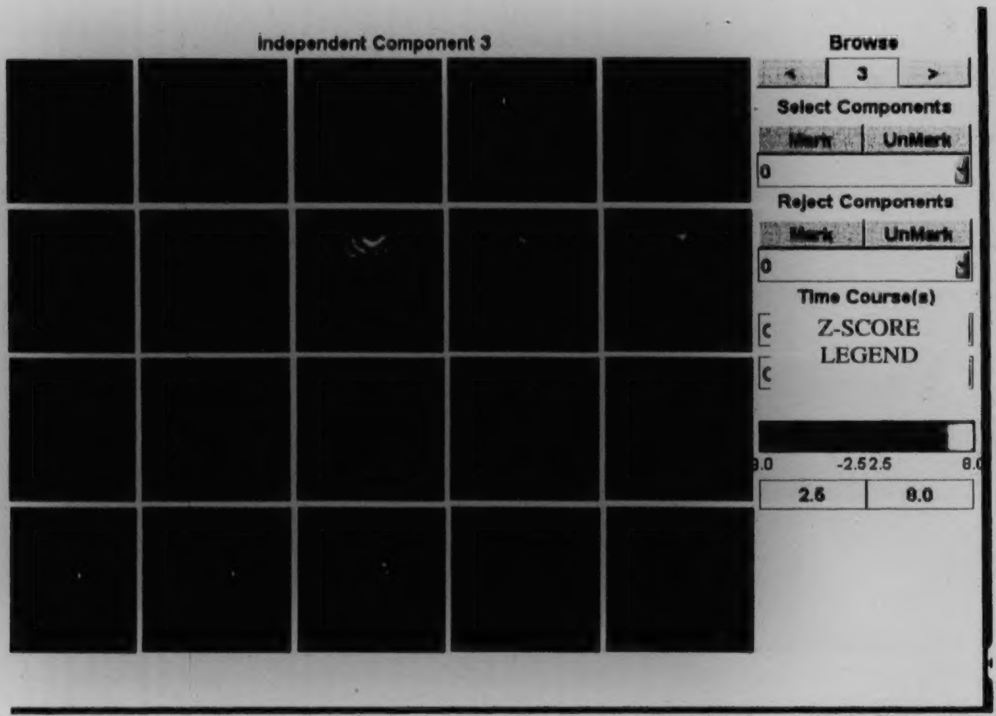
Independent Component 3
Browse
<
3
>
Select Components
Mark
UnMark
0
Reject Components
Mark
UnMark
0
Time Course(s)
Z-SCORE
LEGEND
-2.5 2.5
2.5
8.0

Figure 3.3. Spatial Independent Component Brain Map (Averaged fMRI Data; Right Side of Slice is Left Side of Brain and Bottom of Slice is Anterior of Brain)

Figure 3.4 is the ROA+ time course for the spatial component computed using the averaged fMRI measurements. The signal is approximately one cycle of the sinusoid-shaped signal in Figure 3.2. The peak per cent increase in amplitude of the signal relative to the average signal amplitude in voxels that have a weight greater than z = 2.5 is 0.85 % and the peak per cent decrease in amplitude relative to the average signal amplitude in voxels that have a weight less than z = 2.5 is -0.48 %. The per cent signal amplitude changes were calculated using fMRLAB. The correlation coefficient between this time course and one cycle of the canonical response is 0.87. This correlation coefficient is even higher than the correlation coefficient between the canonical response and the ROA+ average time course for the spatial component computed using the unaveraged fMRI measurements.

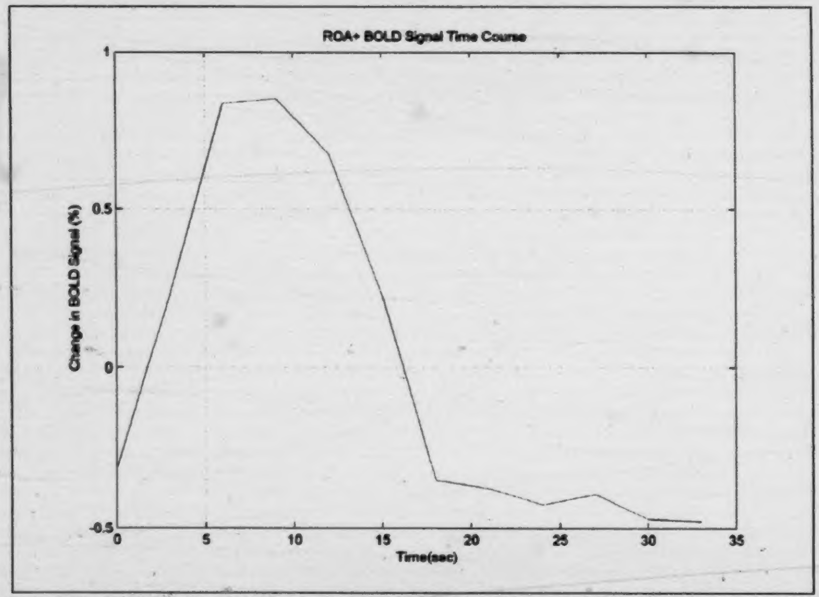

Figure 3.4. ROA+ BOLD Signal Time Course for Task-Related Spatial Independent Component (Averaged fMRI Data)

The time course in Figure 3.4 was concatenated nine times to produce the spatial ICA-derived task-related regressor shown in Figure 3.5.

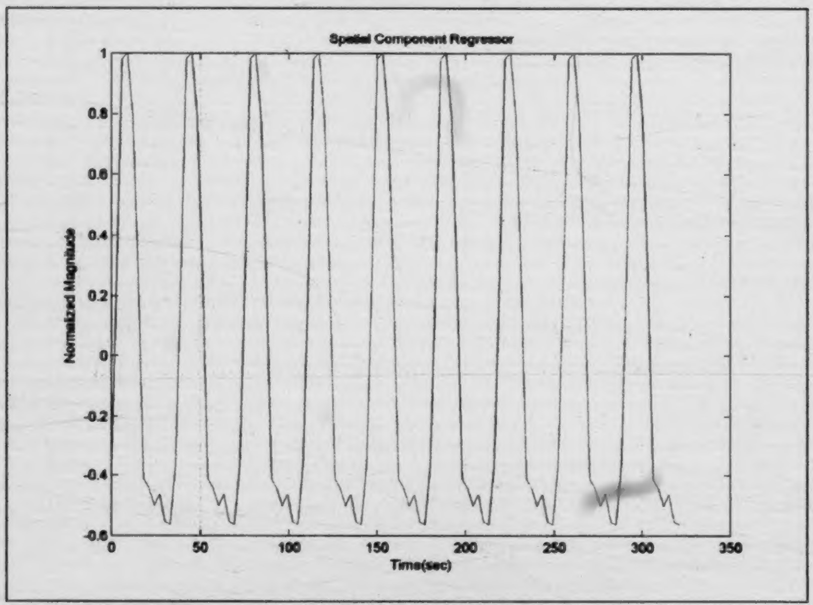

Figure 3.5. Spatial ICA-Derived Regressor

Next, temporal ICA was performed on the unaveraged fMRI measurements from slices 16 to 19. One consistently task-related temporal independent component was identified. Figure 3.6 is the brain map of spatial weights for the task-related temporal component computed using the unaveraged fMRI measurements. The spatial weight vector is displayed on a grey-scale brain map in the figure. The legend of the brain map is shown at the bottom of the brain map. There are several voxels in the left hemisphere motor cortex region that have high spatial weights. There are a few small regions in the supplementary motor cortex that have high spatial weights as well. However, the spatial weights in the supplementary motor cortex are not as high as those in the motor cortex region.

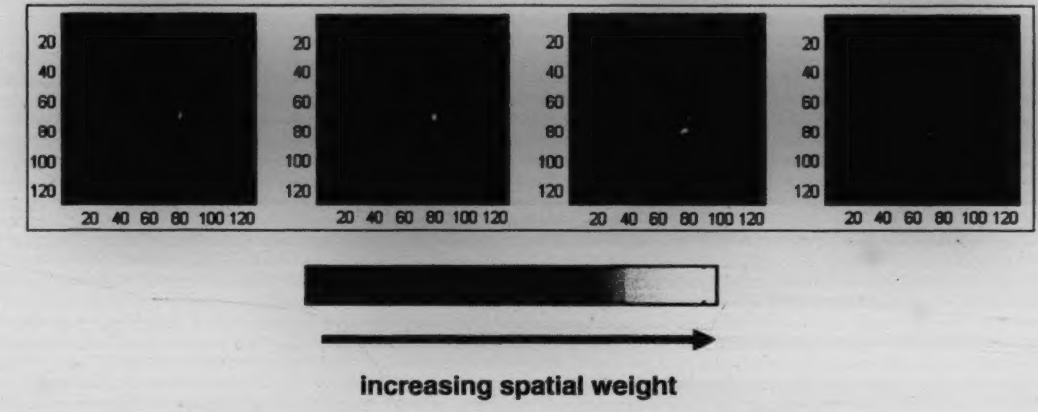

Figure 3.6. Brain Map of Spatial Weights for the Task-Related Temporal Independent Component (Unaveraged fMRI Data; Images are in Radiological Orientation)

Figure 3.7 is the temporal independent component time course computed using the unaveraged fMRI measurements. This time course shows a sinusoid-shaped signal. However, the amplitudes of peaks and troughs are not constant across trials. The correlation coefficient between this time course and the canonical hemodynamic response is 0.80. This correlation coefficient is considered to be sufficiently high.

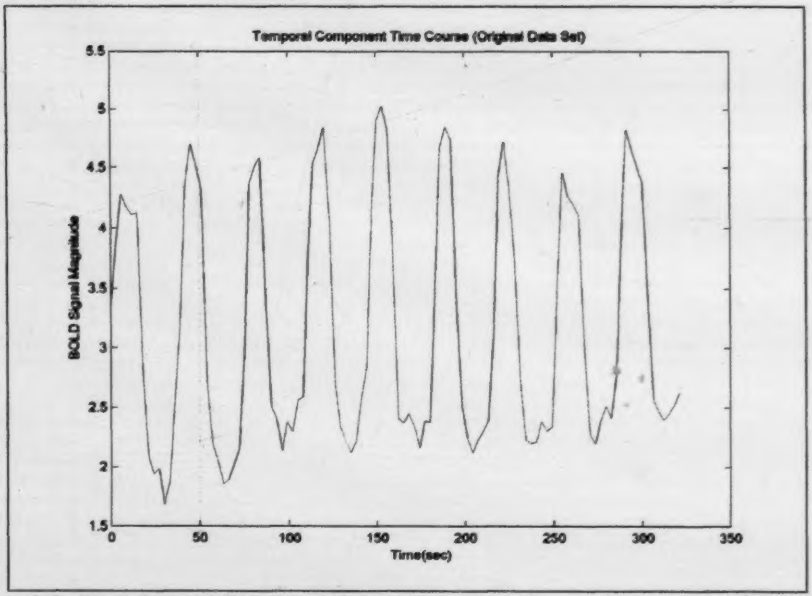

Figure 3.7. Task-Related Temporal Component Time Course (Unaveraged fMRI Data)

Figure 3.8 is the spatial weight vector of the task-related temporal component computed using the averaged fMRI measurements. The spatial weights are high in locations that are similar to the locations of high spatial weights in Figure 3.6.

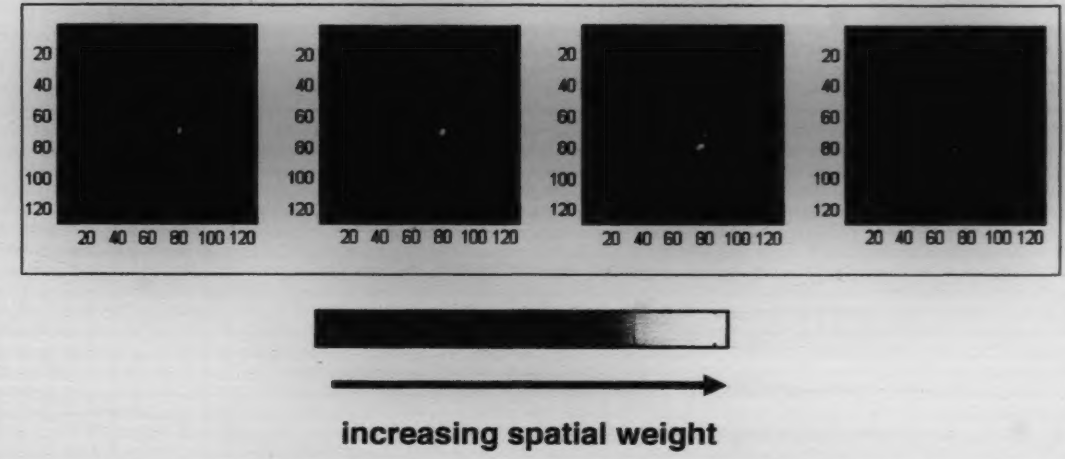
20
40
60
80
100
120
20 40 60 80 100 120
increasing spatial weight

Figure 3.8. Brain Map of Spatial Weights for the Task-Related Temporal Independent Component (Averaged fMRI Data; Images are in Radiological Orientation)

Figure 3.9 is the temporal component time course computed using the averaged fMRI measurements. The signal is approximately one cycle of the sinusoid-shaped signal in Figure 3.7. The correlation coefficient between this time course and one cycle of the canonical response is 0.86. This correlation coefficient is even higher than the correlation coefficient between the canonical response and the temporal independent component time course computed using the unaveraged fMRI measurements.

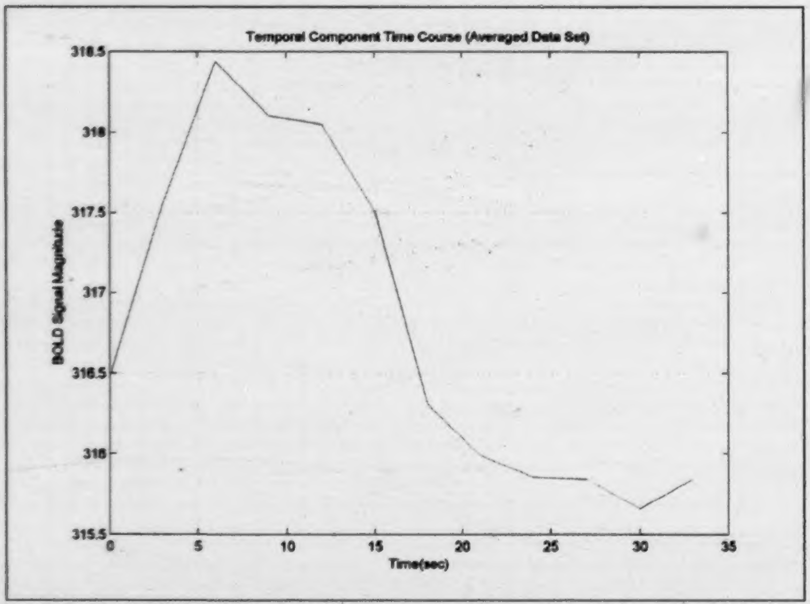

Figure 3.9. Task-Related Temporal Component Time Course (Averaged fMRI Data)

The time course in Figure 3.9 was concatenated nine times to produce the temporal ICA-derived task-related regressor shown in Figure 3.10.

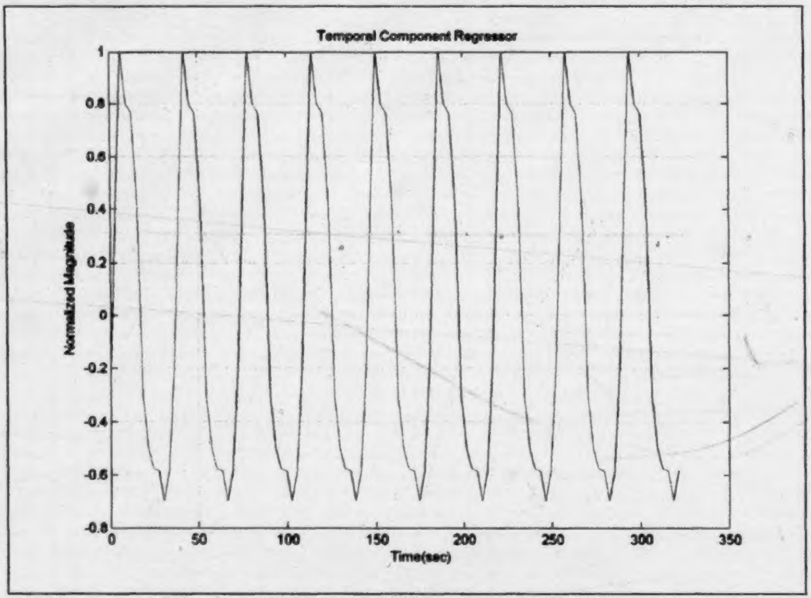

Figure 3.10. Temporal ICA-Derived Regressor

The last regressor that was produced to use in a GLM is the canonical hemodynamic response regressor. This regressor is shown in Figure 3.11.

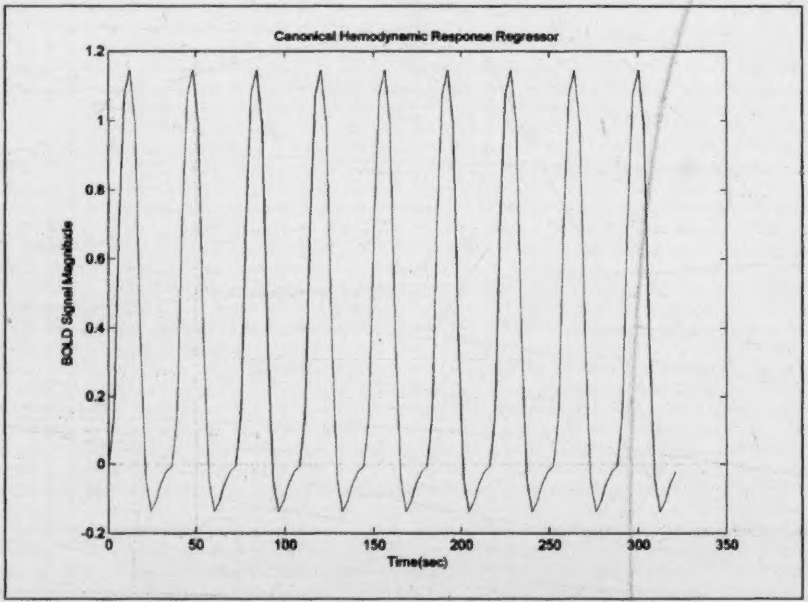

Figure 3.11. Canonical Hemodynamic Response Regressor

3.1.2 fMRI Measurement Statistical Analyses

The regressors in Figure 3.5, Figure 3.10 and Figure 3.11 were placed in separate GLMs to perform separate parameter estimations. A Student's t-test ($\alpha_{FWE} \leq 0.01$ with a contiguous active voxel extent minimum of 5 voxels) was performed on each of the parameter estimates corresponding to the task-related regressors. The voxels that were active according to the Student's t-tests are shown on brain maps below. Figure 3.12 is the activation map that resulted from the t-test in which the spatial ICA-derived regressor was the task-related regressor. Figure 3.13 is the activation map that resulted from the t-test in which the temporal ICA-derived regressor was the task-related regressor. Lastly, Figure 3.14 is the activation map that resulted from the t-test in which the canonical hemodynamic response regressor was the task-related regressor.

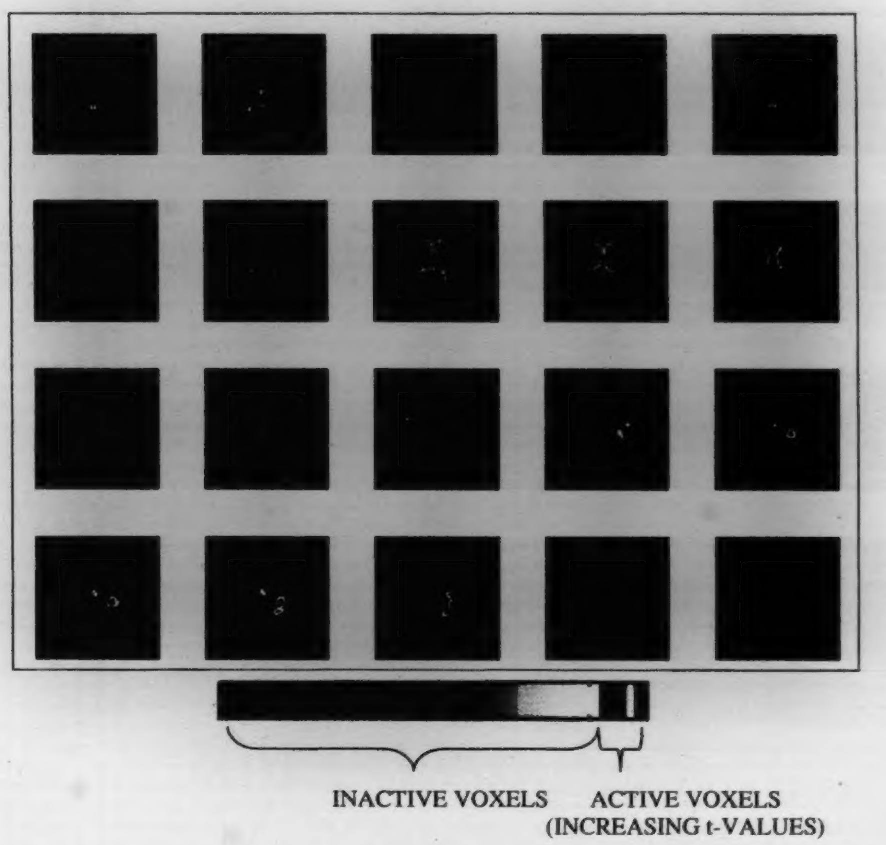
INACTIVE VOXELS
ACTIVE VOXELS
(INCREASING t-VALUES)

Figure 3.12. Activation Map Computed Using Student's t-test with the Spatial ICA-Derived Regressor (Images are in Radiological Orientation)

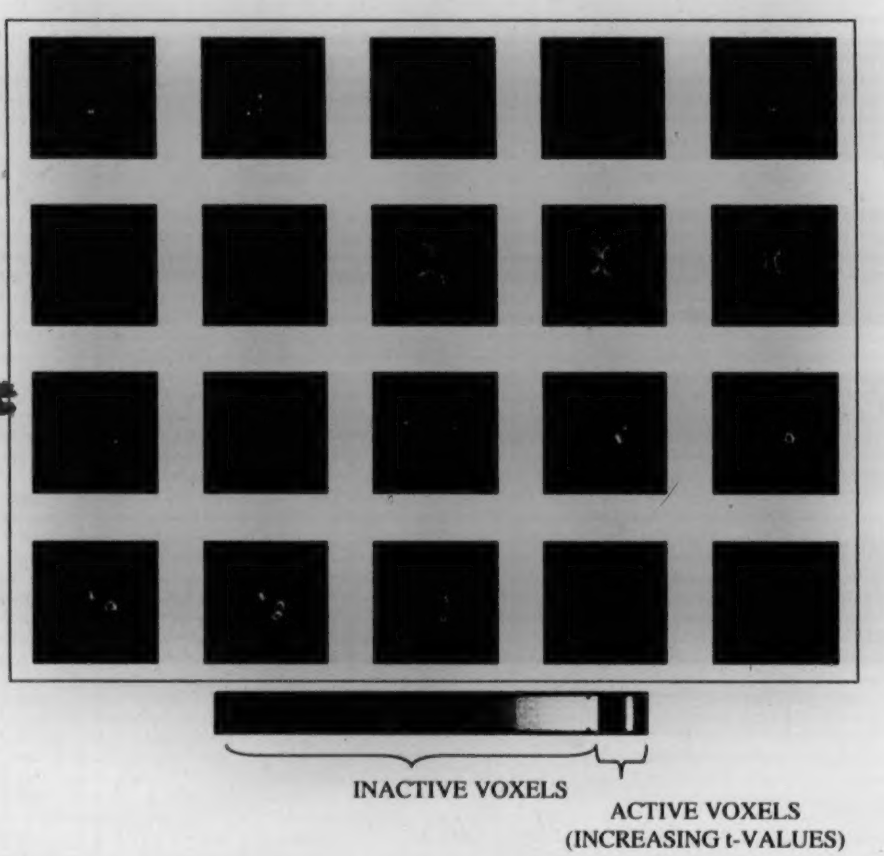
INACTIVE VOXELS
ACTIVE VOXELS
(INCREASING t-VALUES)

Figure 3.13. Activation Map Computed Using Student's t-test with the Temporal ICA-Derived Regressor (Images are in Radiological Orientation)

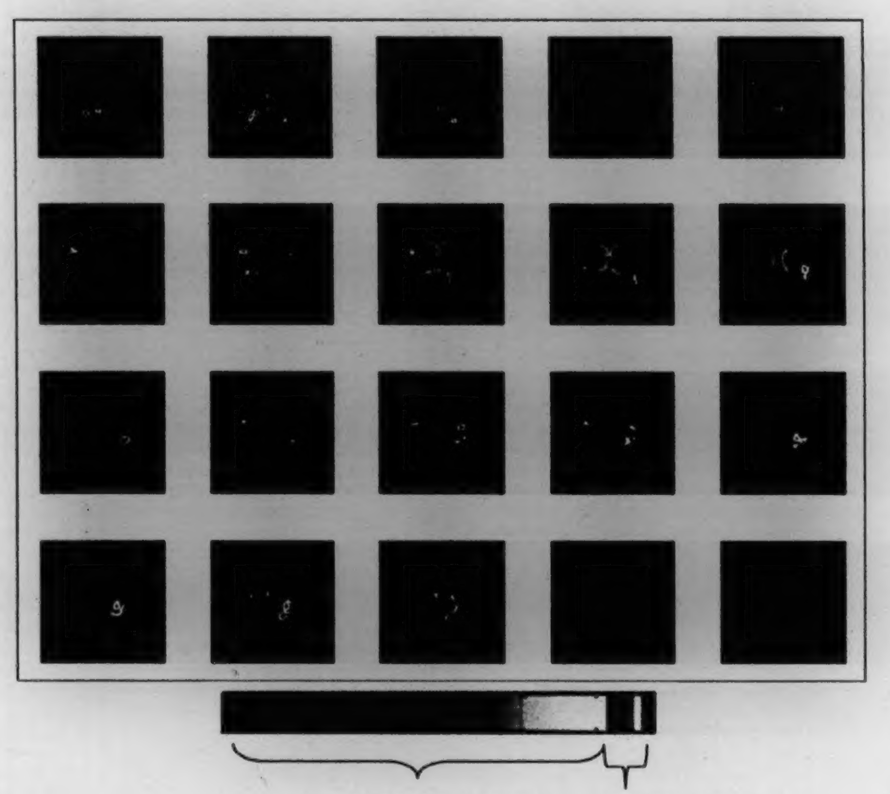

Figure 3.14. Activation Map Computed Using Student's t-test with the Canonical Hemodynamic Response Regressor (Images are in Radiological Orientation)

3.1.3 HR Model Comparisons

In the final phase of this study, the results from the Student's t-tests performed using all three HR models were compared using various measures and statistics. The voxels that were active according to the t-test results were subjected to the CR measures, DW statistics and F-statistics calculations. The active voxels that reached the F-statistic threshold were used for the R_a^2 calculations. First, the total number of voxels that were analyzed and the number of active voxels found using each HR model are listed in Table 3.1. Next, the CR measures and the range, mean and standard deviation of each set of active voxel t-values and each set of active voxel DW statistics are also listed in Table

3.1. The number of active voxels (found using each HR model) that had a DW p-value (probability of uncorrelated residuals) of at least 0.50 is listed in Table 3.1 as well. The number of active voxels that reached the F-value threshold is also listed in Table 3.1. Finally, the range, mean and standard deviation of the R_a^2 measures for the active voxels that reached the F-value threshold are listed in Table 3.1.

Table 3.1. Comparison of HR Models

Test/Model	**Canonical HR Model**		**Temporal ICA-Derived HR Model**		**Spatial ICA-Derived HR Model**	
Voxels Analyzed	59, 770		59, 770		59, 770	
Active Voxels	7, 071		10, 229		9, 108	
t-value Range	5.5 - 16.7		5.5 - 27.1		5.5 - 25.7	
Mean t-value	7.7		8.6		8.5	
t-value SD	1.8		3.3		3.2	
Concurrence Ratio (%)	**with TICA-Derived HR Model**	**with SICA-Derived HR Model**	**with Canonical HR Model**	**with SICA-Derived HR Model**	**with Canonical HR Model**	**with TICA-Derived HR Model**
	77.4	79.4	77.4	93.6	79.4	93.6
DW p-value Range	0.00 - 0.99		0.00 - 0.99		0.00 – 1.0	
Mean DW p-value	0.020		0.024		0.024	
DW p-value SD	0.083		0.090		0.089	
Voxels with DW p $\geq$ 0.50	52		102		87	
Voxels with F $\geq$ 2.99	7, 071		10, 229		9, 108	
R_a^2 Range	0.18 - 0.72		0.18 - 0.87		0.18 - 0.86	
Mean R_a^2	0.32		0.37		0.36	
R_a^2 SD	0.11		0.16		0.15	

3.2 Study 2: Event-Related Paradigm

3.2.1 Regressor Preparations

After the fMRI measurements were acquired and preprocessed, the fMRI measurements were subjected to a spatial ICA algorithm. The brain maps of the interictal event-related spatial independent components for run 1, run 2 and run 3 are shown in Figure 3.15, Figure 3.16 and Figure 3.17, respectively. The highest spatial weights of these components are in the right temporal lobe of the patient's brain. The correlation coefficients between the spatial component time courses and the canonical hemodynamic responses (in corresponding runs) are listed in Table 3.2.

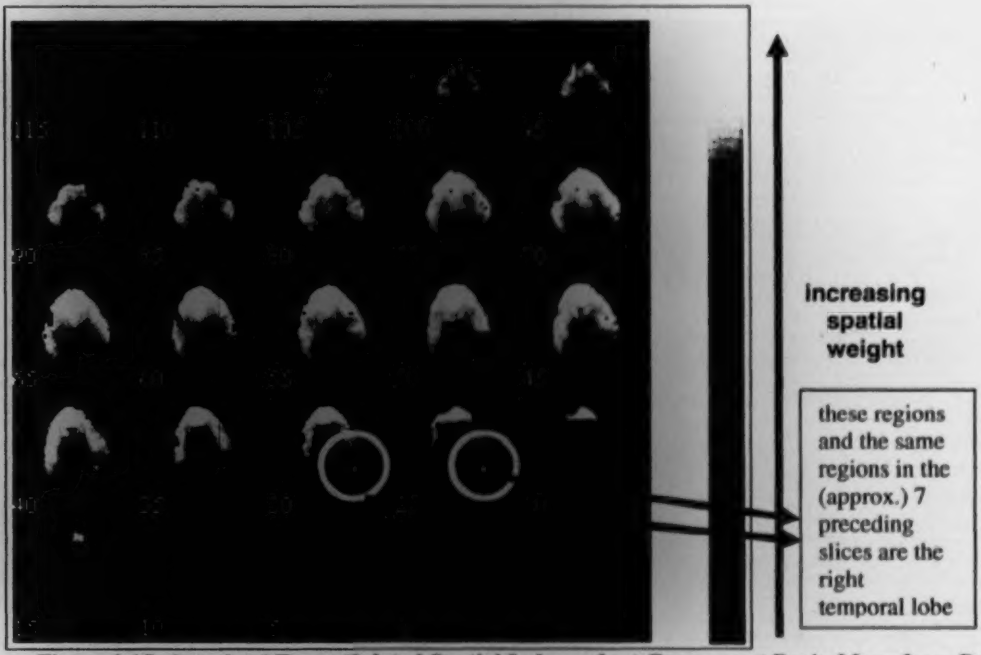
increasing spatial weight
these regions and the same regions in the (approx.) 7 preceding slices are the right temporal lobe

Figure 3.15. Interictal Event-Related Spatial Independent Component Brain Maps from Run 1 (Images are in Neurological Orientation)

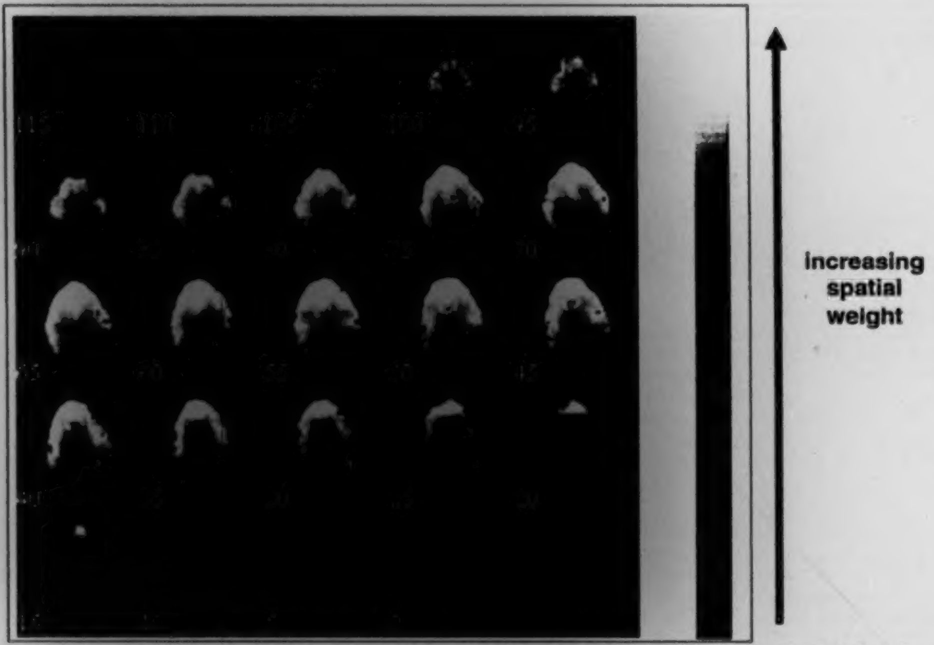
increasing
spatial
weight

Figure 3.16. Interictal Event-Related Spatial Independent Component Brain Map from Run 2 (Images are in Neurological Orientation)

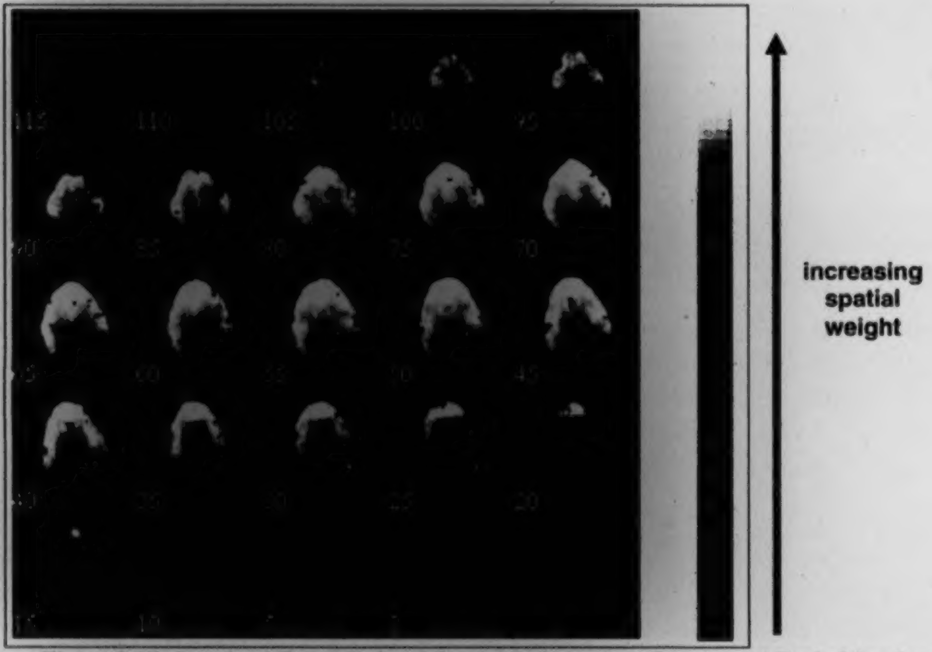
increasing
spatial
weight

Figure 3.17. Interictal Event-Related Spatial Independent Component Brain Map from Run 3 (Images are in Neurological Orientation)

Table 3.2. Spatio-Temporal Component Derivation Results

	Run 1	Run 2	Run 3
Spatial Component Time Course Correlation Coefficient with Canonical Response	-0.30	-0.30	-0.37
Max z-score from Spatial Weights	11.6	9.8	9.6
Number of Voxels with z-score ≥ 80% of z_{max}	12	12	12
Number of Temporal Independent Components Produced	3	3	3
Temporal Component Correlation Coefficient with Spatial Component Time Course	0.92	0.95	0.95

Time courses from voxels that had z-scores that were at least 80% of the maximum z-score in the corresponding interictal event-related spatial component were subjected to a temporal ICA algorithm. The number of voxels with z-score values above the threshold in each run was recorded in Table 3.2. The correlation coefficients between the interictal event-related temporal component chosen from each run and the corresponding spatial component time course are shown in Table 3.2. These temporal components had the highest correlation coefficients, so they were chosen as the interictal event-related spatio-temporal components.

The interictal event-related spatio-temporal component time courses are shown in Figure 3.18, Figure 3.19 and Figure 3.20. Spatio-temporal component time samples that are not in a 33-second window (the duration of the canonical impulse response according to SPM5) after interictal events occurred were removed from the spatio-temporal components. The time samples were removed by setting the amplitudes of the signals to 0. Any hemodynamic activity in the spatio-temporal components that occurs outside this time frame is assumed to be unrelated to the interictal events. The spatio-temporal components that have time samples set to 0 were given the name "zeroed spatio-temporal components". The canonical responses are superimposed on the zeroed spatio-temporal components in Figure 3.18, Figure 3.19 and Figure 3.20 so that the zeroed spatio-temporal components and canonical responses can be compared. Moreover, the interictal event pulse trains are also included in the figures so that the timing of the zeroed spatio-temporal components and the timing of the canonical responses relative to the interictal event onsets can be examined. It is evident from Figure 3.18, Figure 3.19 and Figure 3.20 that the patient exhibited negative BOLD hemodynamic responses to the interictal events she experienced. However, the zeroed spatio-temporal components in the figures also show positive phases that are smaller in amplitude than the negative phases.

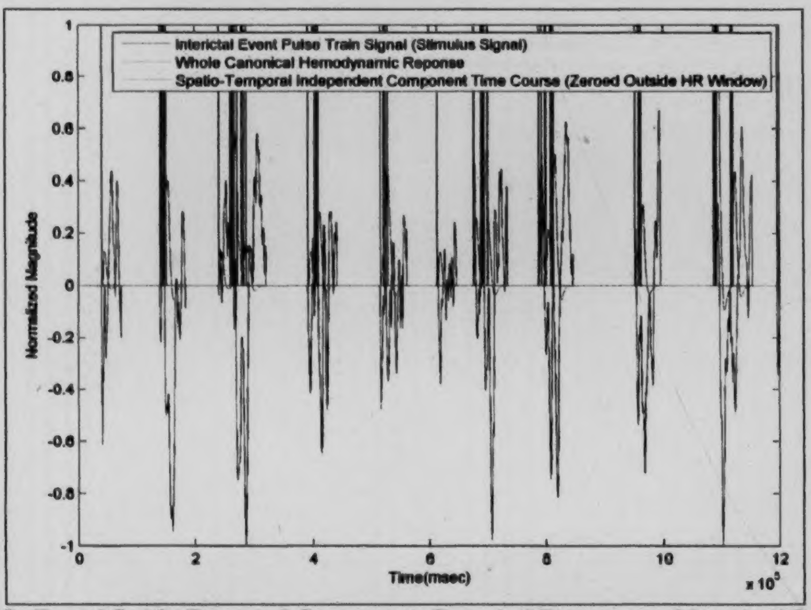

Figure 3.18. Zeroed Spatio-Temporal Component, Canonical Response and Interictal Event Pulse Train Signal Superimposed on One Another (Run 1)

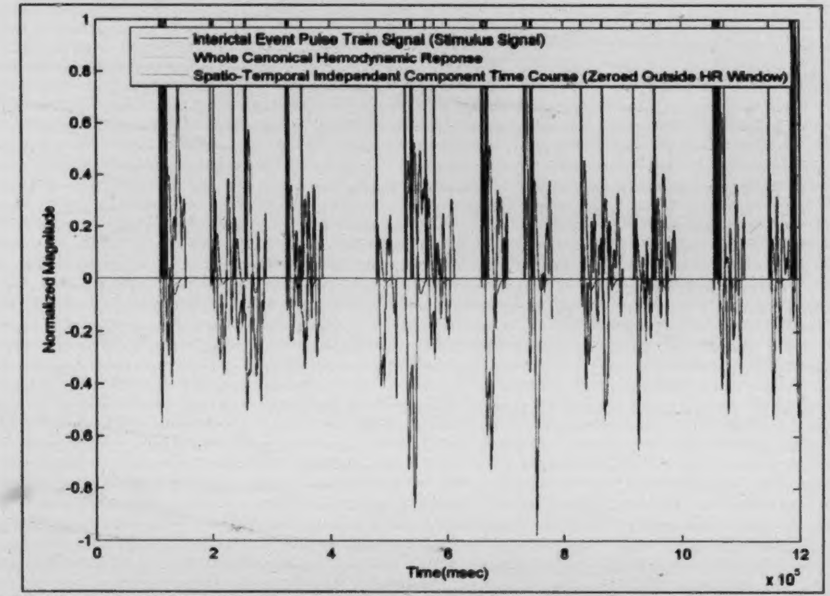

Figure 3.19. Zeroed Spatio-Temporal Component, Canonical Response and Interictal Event Pulse Train Signal Superimposed on One Another (Run 2)

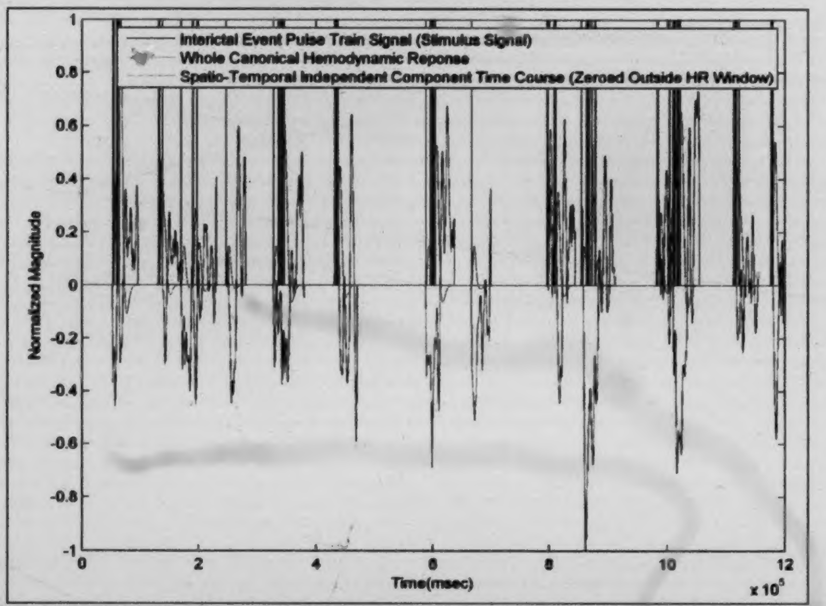

Figure 3.20. Zeroed Spatio-Temporal Component, Canonical Response and Interictal Event Pulse Train Signal Superimposed on One Another (Run 3)

In the next step, the zeroed spatio-temporal components were modified in the frequency domain using a Wiener filter and smoothed using a 133-point Hamming window. These procedures were performed to obtain spatio-temporal ICA-derived hemodynamic impulse responses. The magnitude spectrum of the Wiener filter (M(f) in equation (2.34)) for run 1 is displayed in Figure 3.21. The Wiener filters for runs 2 and 3 were very similar to the Wiener filter for run 1.

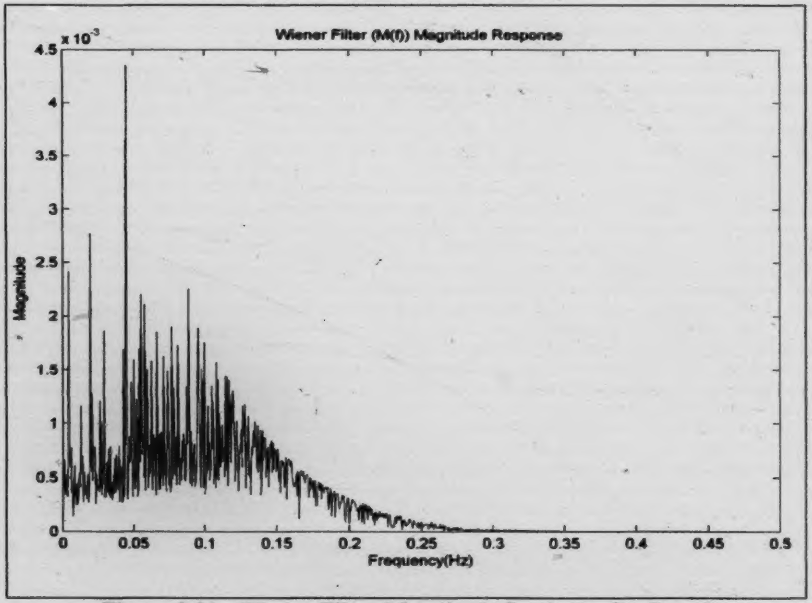

Figure 3.21. Wiener Filter Magnitude Spectrum for Run 1

When the Wiener filters were applied to the frequency spectra of the zeroed spatio-temporal components, the resulting magnitude spectra of the spatio-temporal ICA-derived impulse responses contained frequency components with a considerable magnitude in a band of frequencies that is similar to the pass band of the magnitude spectrum of the canonical impulse response. The magnitude spectra of the canonical hemodynamic impulse response and the spatio-temporal ICA-derived impulse responses are shown in Figure 3.22, Figure 3.23, Figure 3.24 and Figure 3.25.

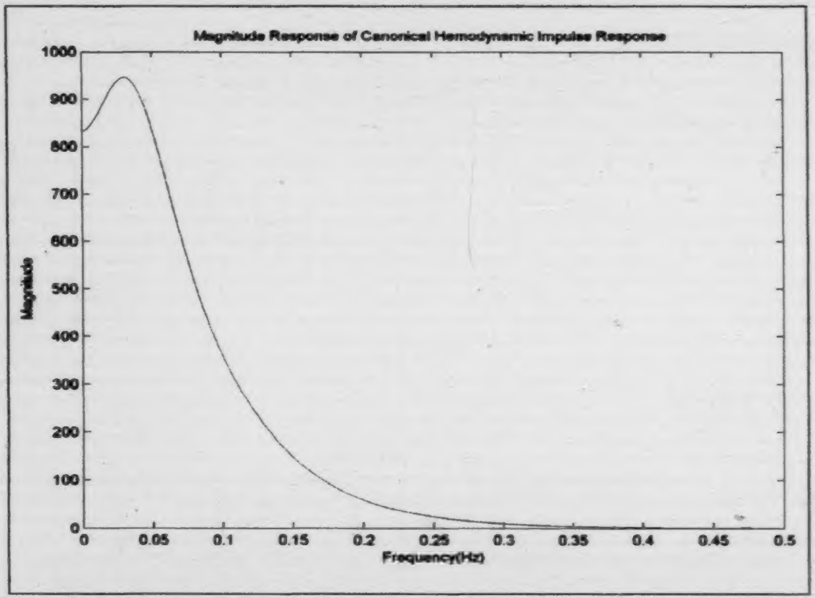

Figure 3.22. Magnitude Response of Canonical Hemodynamic Impulse Response

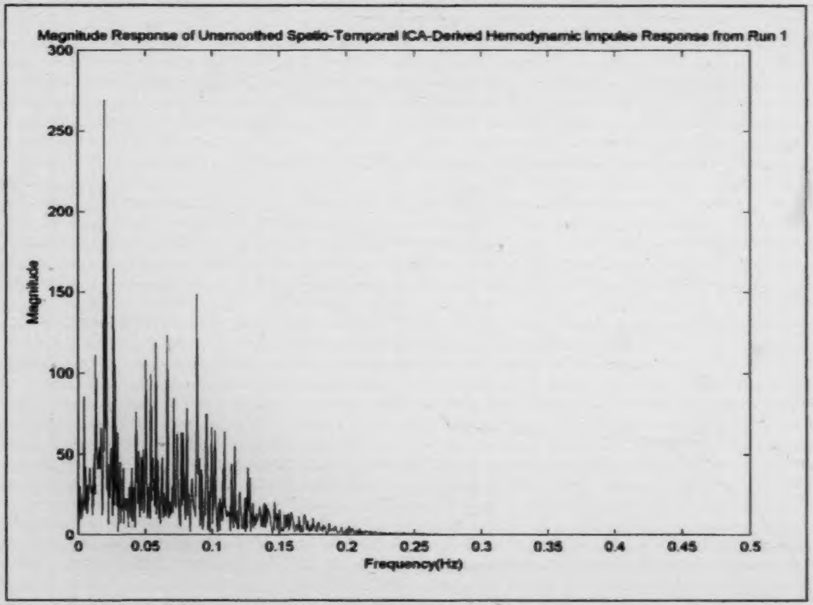

Figure 3.23. Magnitude Response of Spatio-Temporal ICA-Derived Impulse Response (Run 1)

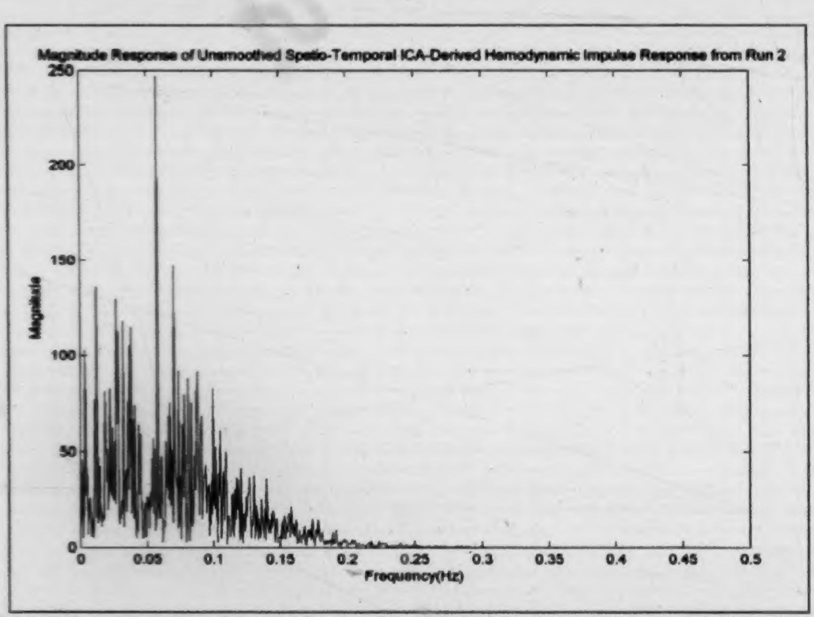

Figure 3.24. Magnitude Response of Spatio-Temporal ICA-Derived Impulse Response (Run 2)

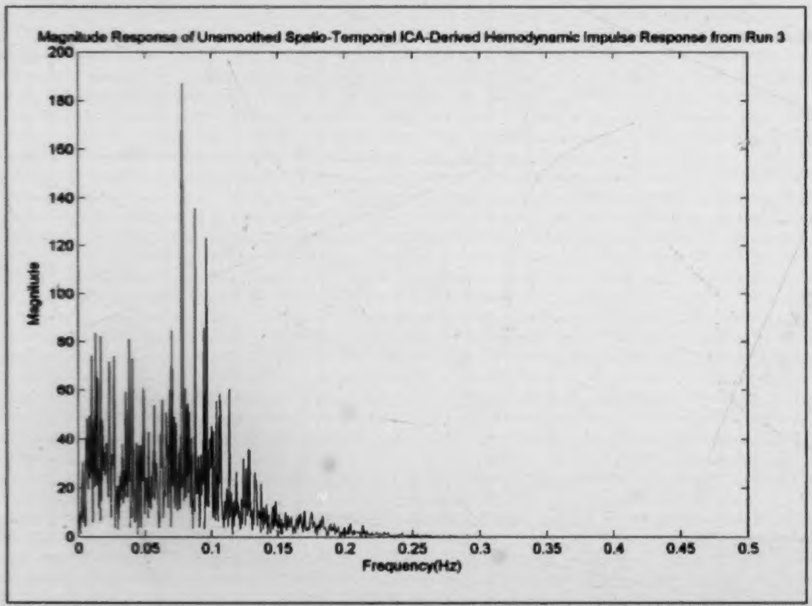

Figure 3.25. Magnitude Response of Spatio-Temporal ICA-Derived Impulse Response (Run 3)

The magnitude spectrum of the canonical impulse response is much smoother than the magnitude spectra of the spatio-temporal ICA-derived impulse responses. Sharp peaks in the spectra of the spatio-temporal ICA-derived impulse responses caused a significant number of oscillations to appear in the time domain versions of the spatio-temporal ICA-derived impulse responses. The spatio-temporal ICA-derived impulse response (time domain) for run 1 that has an unsmoothed frequency spectrum is shown in Figure 3.26. The spatio-temporal ICA-derived impulse responses for run 2 and run 3 had similar oscillations.

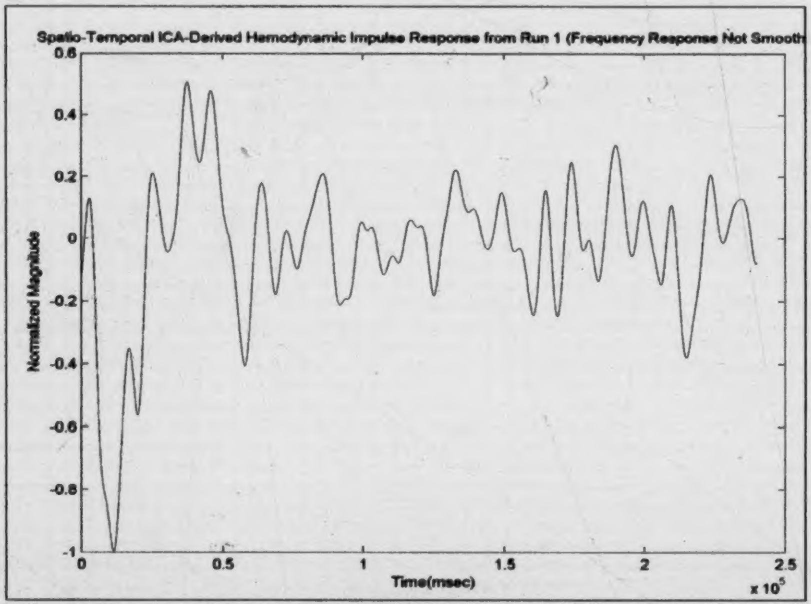

Figure 3.26. Spatio-Temporal ICA-Derived Impulse Response from Run 1 (Unsmoothed Frequency Response)

The magnitude spectra that were generated after convolving the frequency spectra of the spatio-temporal ICA-derived impulse responses with a 133-point Hamming window are shown in Figure 3.27, Figure 3.28 and Figure 3.29. These magnitude spectra are much smoother than the unsmoothed versions in Figure 3.23, Figure 3.24 and Figure 3.25.

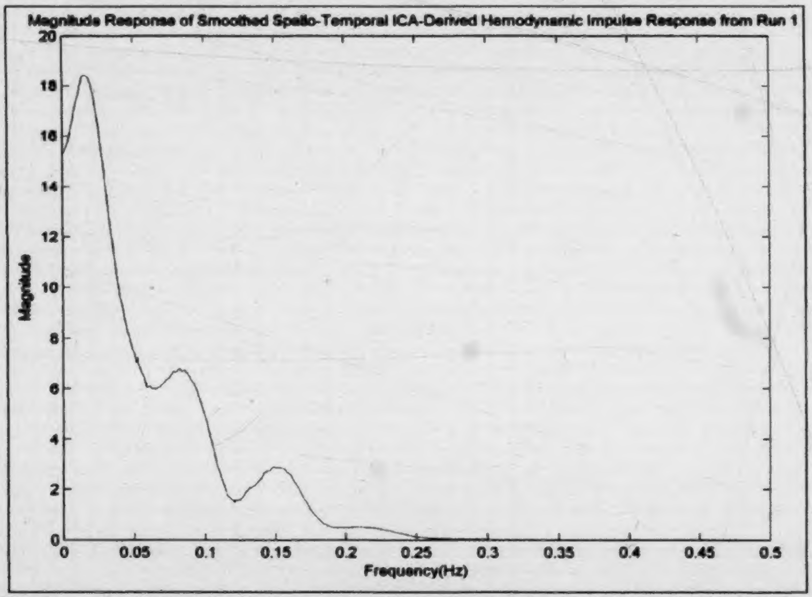

Figure 3.27. Smoothed Magnitude Spectrum of Spatio-Temporal ICA-Derived Impulse Response (Run 1)

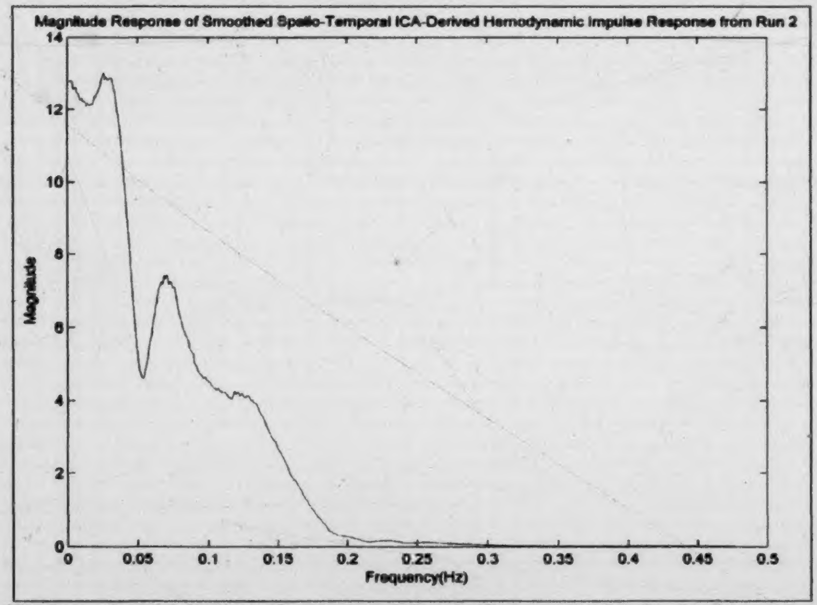

Figure 3.28. Smoothed Magnitude Spectrum of Spatio-Temporal ICA-Derived Impulse Response (Run 2)

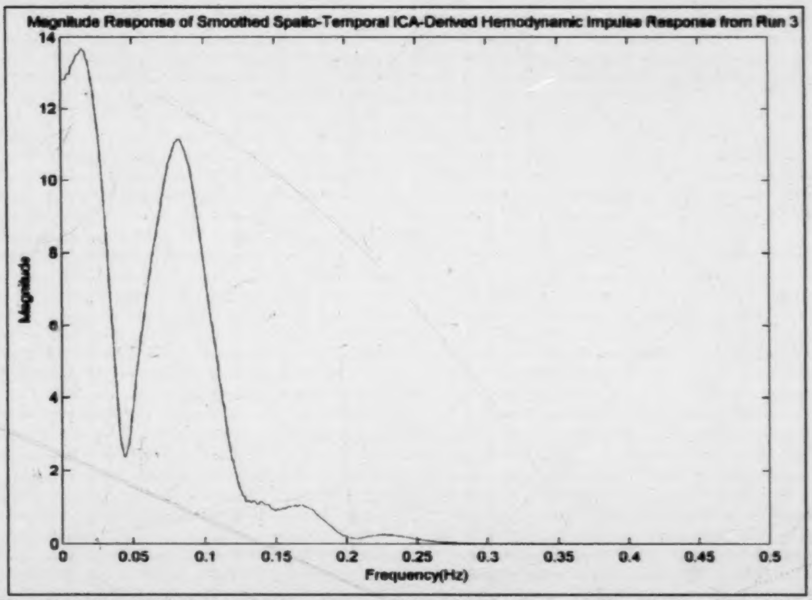

Figure 3.29. Smoothed Magnitude Spectrum of Spatio-Temporal ICA-Derived Impulse Response (Run 3)

The inverse Fourier transforms of the smoothed frequency spectra of the spatio-temporal ICA-derived impulse responses were performed. The resulting spatio-temporal ICA-derived impulse responses are shown in Figure 3.30, Figure 3.31 and Figure 3.32. The canonical impulse response is shown in Figure 1.9 for comparison.

The time that elapsed for each spatio-temporal ICA-derived impulse response to reach its most negative peak was recorded. The duration measured for the impulse response from run 1 was 10.6 seconds. The duration measured for the impulse response from run 2 was 7.3 seconds. The duration measured for the impulse response from run 3 was 6.7 seconds.

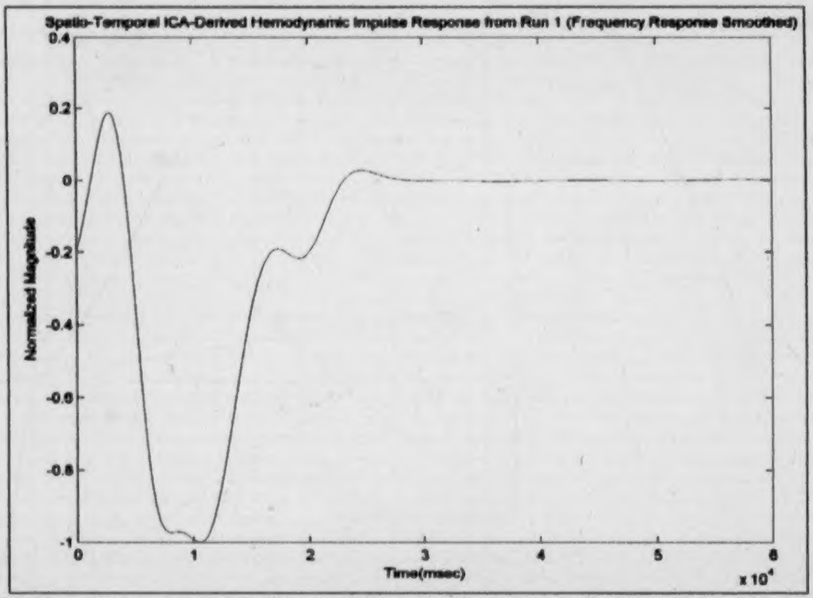

Figure 3.30. Spatio-Temporal ICA-Derived Impulse Response from Run 1 (Smoothed Frequency Spectrum)

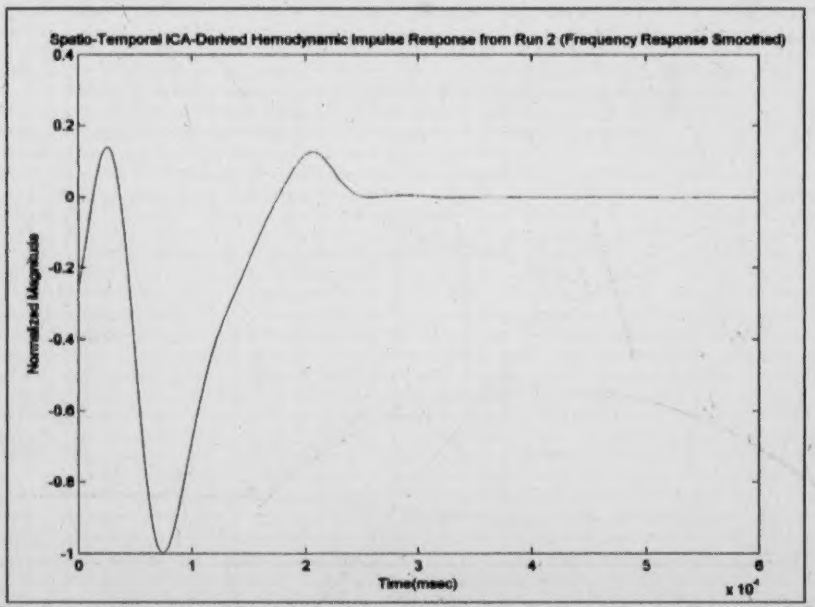

Figure 3.31. Spatio-Temporal ICA-Derived Impulse Response from Run 2 (Smoothed Frequency Spectrum)

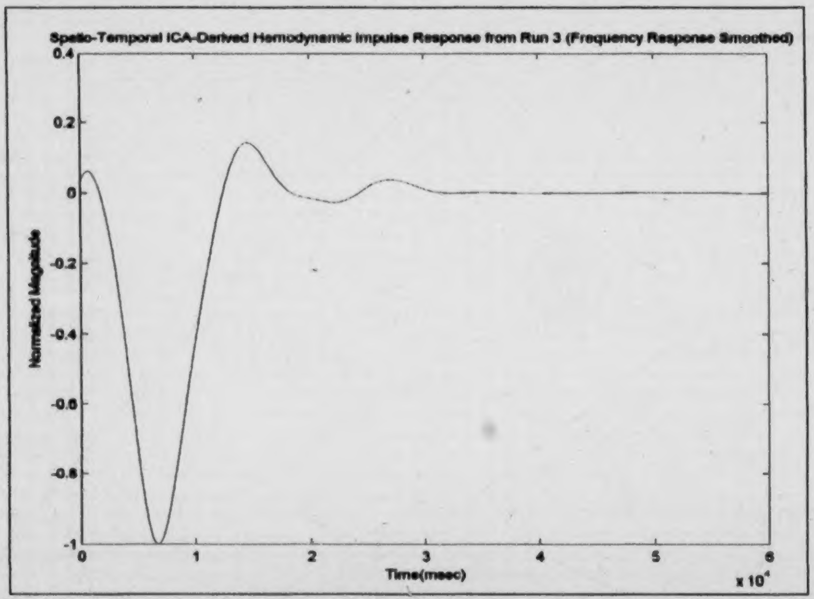

Figure 3.32. Spatio-Temporal ICA-Derived Impulse Response from Run 3 (Smoothed Frequency Spectrum)

Finally, the spatio-temporal ICA-derived hemodynamic responses were generated. To create the hemodynamic responses, each spatio-temporal ICA-derived impulse response was convolved with the interictal event pulse train from the same run. The resulting signals were then decimated with a sampling rate of 0.67 Hz to obtain hemodynamic responses that were 800 time samples each. The spatio-temporal ICA-derived responses were then used as regressors in the statistical analyses of the fMRI measurements. The spatio-temporal ICA-derived hemodynamic responses are superimposed on the spatio-temporal components that were used to derive them as shown in Figure 3.33, Figure 3.34 and Figure 3.35. These figures are provided to compare the spatio-temporal ICA-derived hemodynamic responses with their corresponding spatio-temporal component time courses.

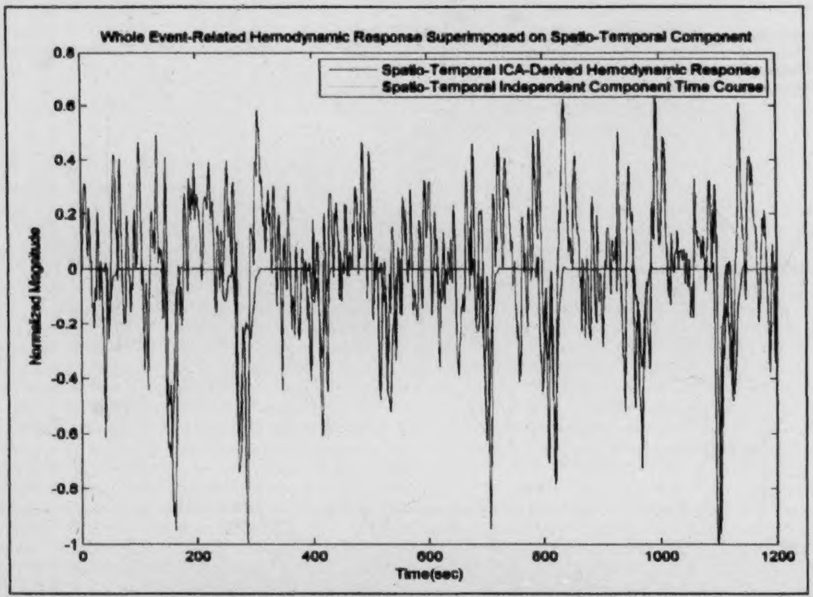

Figure 3.33. Spatio-Temporal ICA-Derived Hemodynamic Response Superimposed on Spatio-Temporal Component Time Course (Run 1)

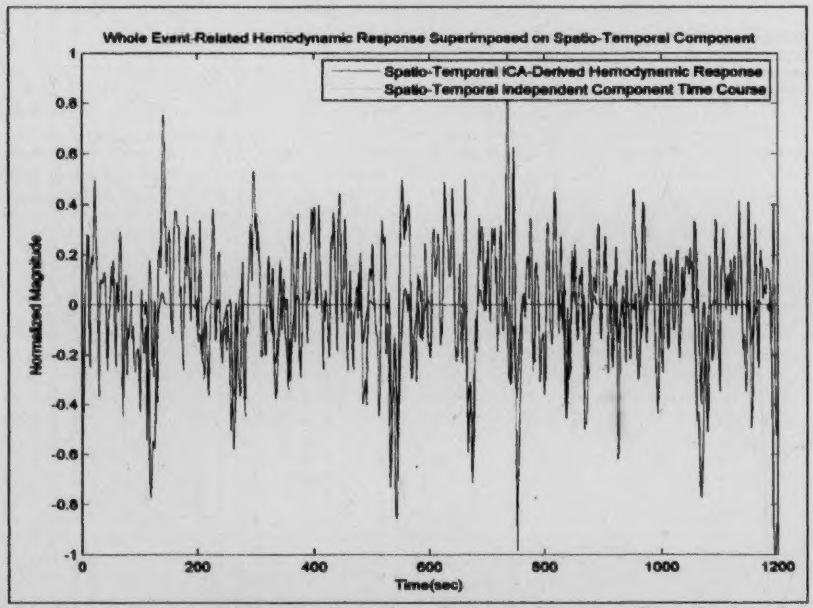

Figure 3.34. Spatio-Temporal ICA-Derived Hemodynamic Response Superimposed on Spatio-Temporal Component Time Course (Run 2)

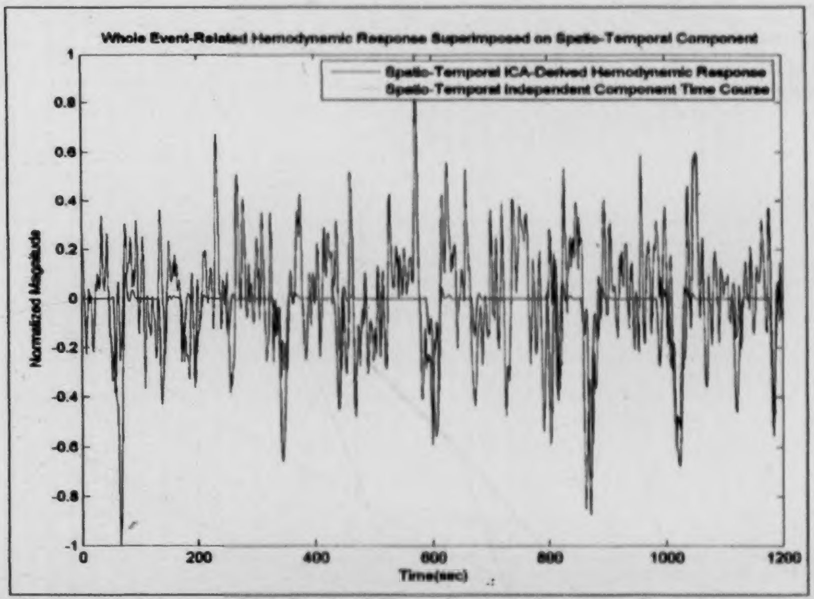

Figure 3.35. Spatio-Temporal ICA-Derived Hemodynamic Response Superimposed on Spatio-Temporal Component Time Course (Run 3)

3.2.2 fMRI Measurement Statistical Analyses

After the spatio-temporal ICA-derived hemodynamic responses were produced, the canonical hemodynamic response signals, inverted canonical hemodynamic response signals and the spatio-temporal ICA-derived hemodynamic response signals were placed into separate design matrices. The parameters were estimated and the residuals were calculated for each GLM. Afterward, t-tests were performed on the parameter estimates corresponding to each interictal event-related regressor for each run. The active voxels were determined from the t-test results. The brain maps that show the active voxels computed from the t-tests in which the canonical hemodynamic responses were used in the GLMs are shown in Figure 3.36, Figure 3.39 and Figure 3.42. The brain maps that show the active voxels computed from the t-tests in which the spatio-temporal ICA-derived responses were used in the GLMs are shown in Figure 3.37, Figure 3.40 and Figure 3.43. The brain maps that show the active voxels computed from the t-tests in which the inverted canonical hemodynamic responses were used in the GLMs are shown in Figure 3.38, Figure 3.41 and Figure 3.44.

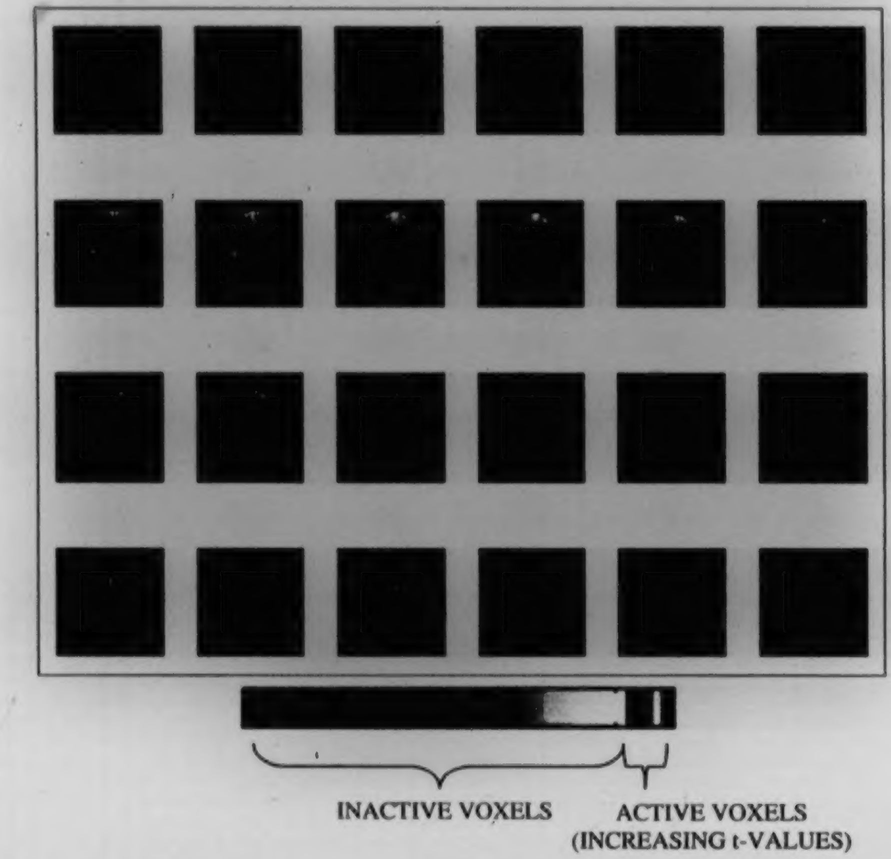
INACTIVE VOXELS
ACTIVE VOXELS
(INCREASING t-VALUES)

Figure 3.36. Brain Map Showing Active Voxels Determined by t-test using Canonical Hemodynamic Response Regressor (Run 1; Images are in Radiological Orientation)

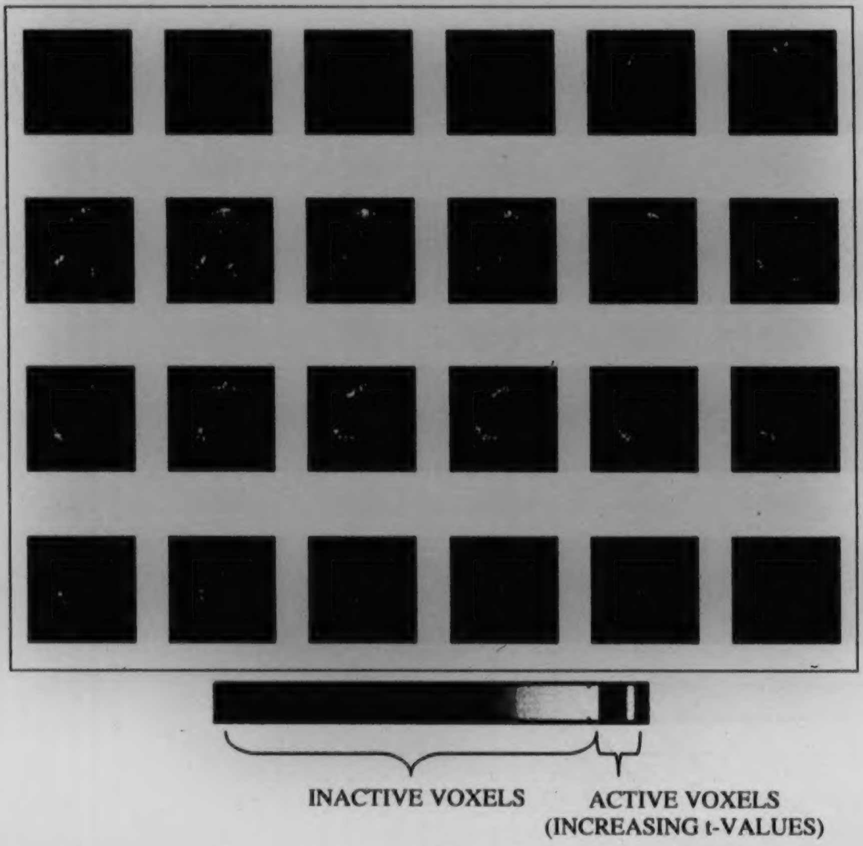
INACTIVE VOXELS
ACTIVE VOXELS
(INCREASING t-VALUES)

Figure 3.37. Brain Map Showing Active Voxels Determined by t-test using Spatio-Temporal ICA-Derived Hemodynamic Response Regressor (Run 1; Images are in Radiological Orientation)

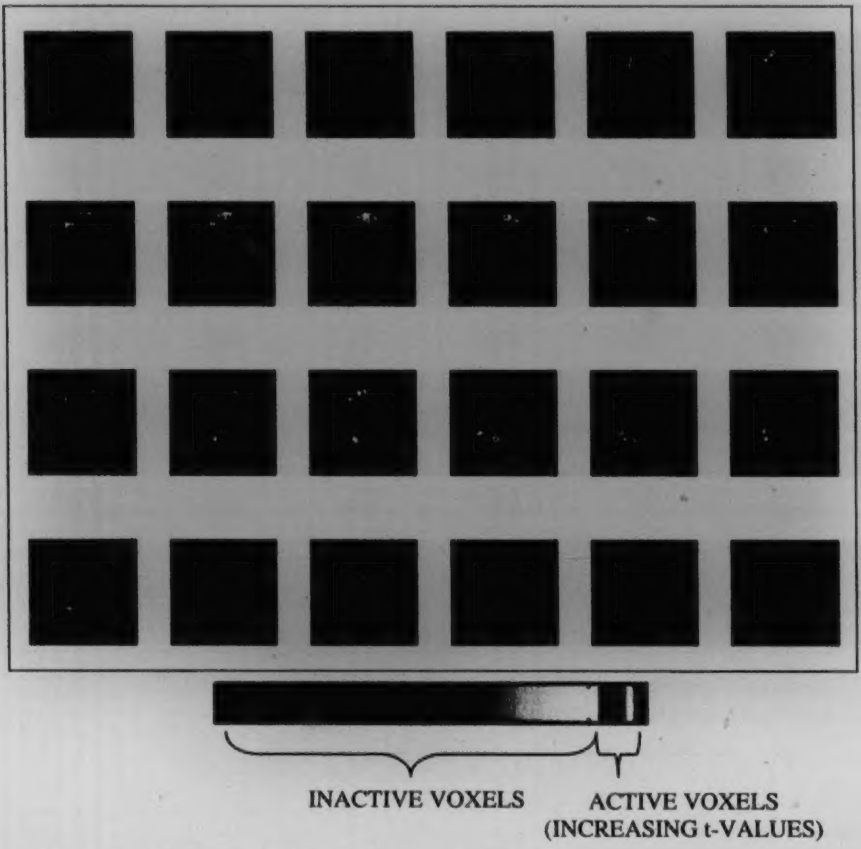
INACTIVE VOXELS
ACTIVE VOXELS
(INCREASING t-VALUES)

Figure 3.38. Brain Map Showing Active Voxels Determined by t-test using Inverted Canonical Hemodynamic Response Regressor (Run 1; Images are in Radiological Orientation)

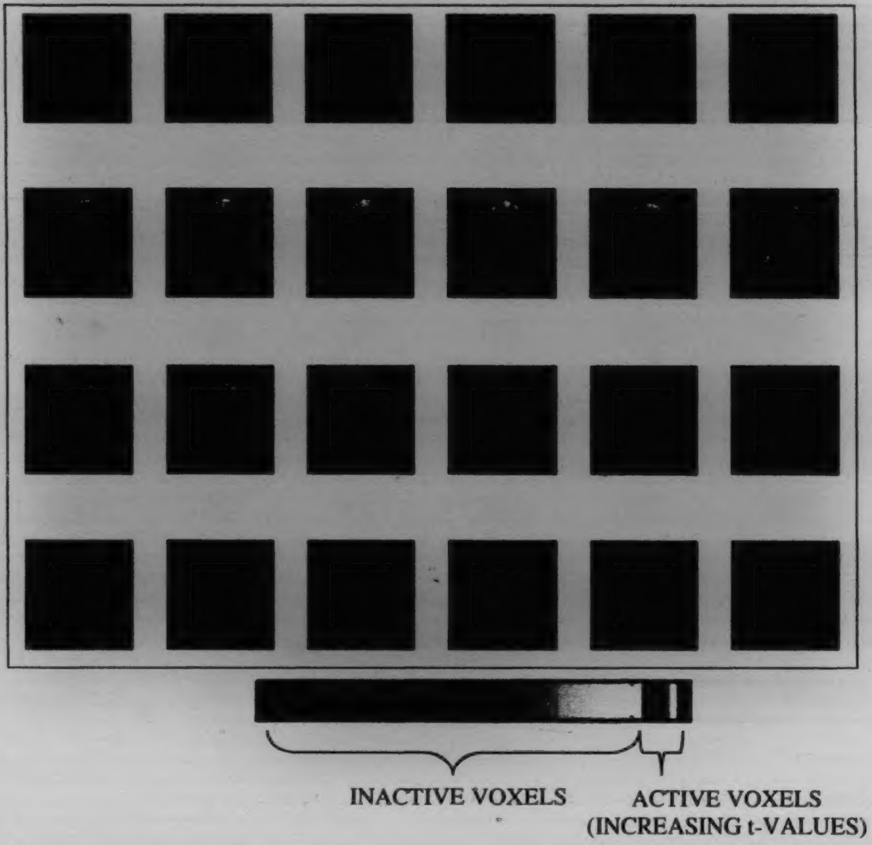
INACTIVE VOXELS
ACTIVE VOXELS
(INCREASING t-VALUES)

Figure 3.39. Brain Map Showing Active Voxels Determined by t-test using Canonical Hemodynamic Response Regressor (Run 2; Images are in Radiological Orientation)

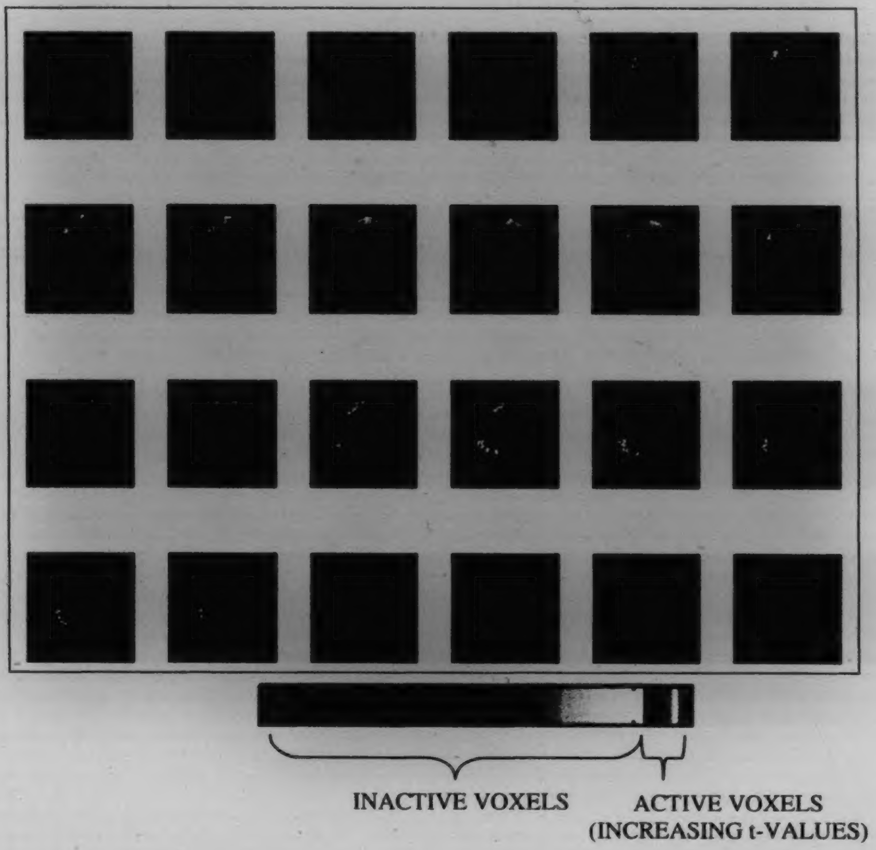
INACTIVE VOXELS
ACTIVE VOXELS
(INCREASING t-VALUES)

Figure 3.40. Brain Map Showing Active Voxels Determined by t-test using Spatio-Temporal ICA-Derived Hemodynamic Response Regressor (Run 2; Images are in Radiological Orientation)

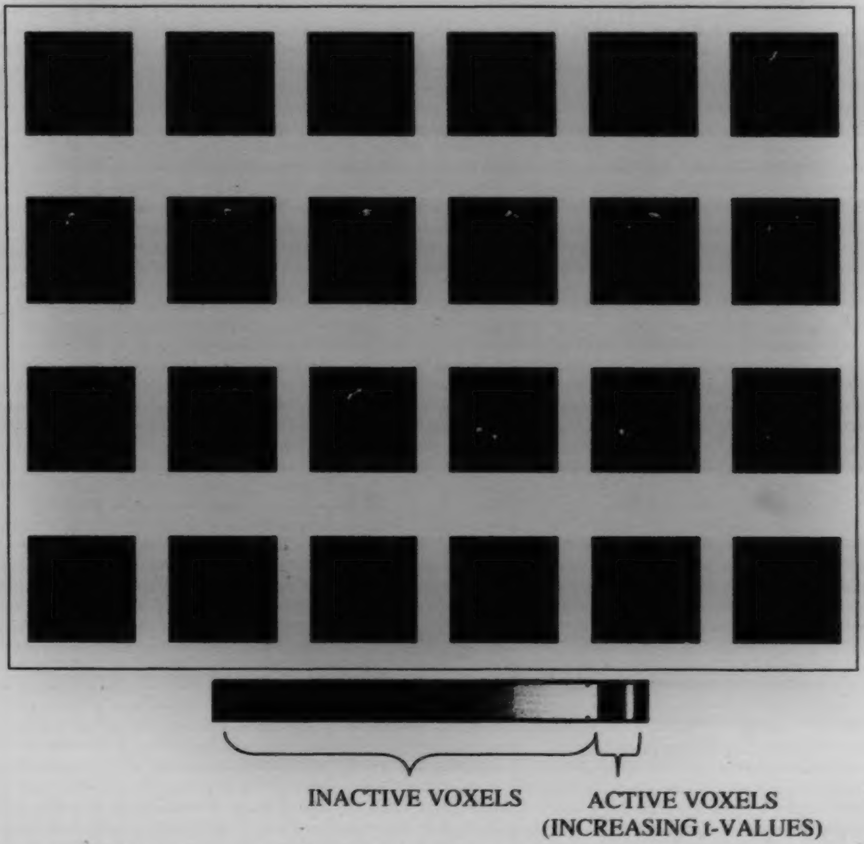
INACTIVE VOXELS
ACTIVE VOXELS
(INCREASING t-VALUES)

Figure 3.41. Brain Map Showing Active Voxels Determined by t-test using Inverted Canonical Hemodynamic Response Regressor (Run 2; Images are in Radiological Orientation)

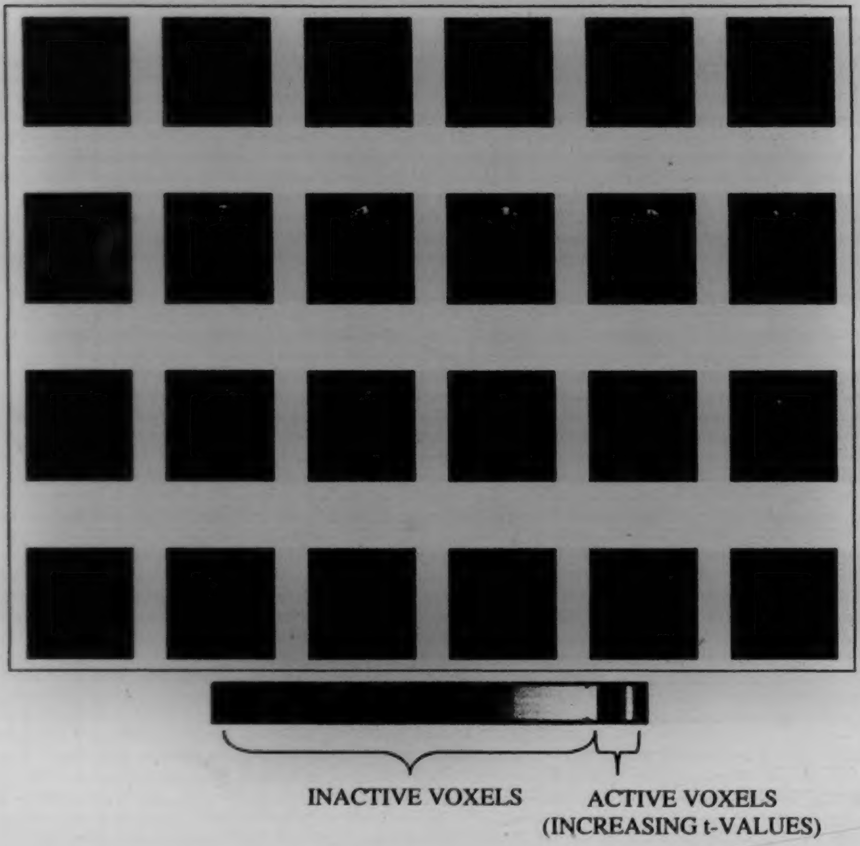
INACTIVE VOXELS
ACTIVE VOXELS
(INCREASING t-VALUES)

Figure 3.42. Brain Map Showing Active Voxels Determined by t-test using Canonical Hemodynamic Response Regressor (Run 3; Images are in Radiological Orientation)

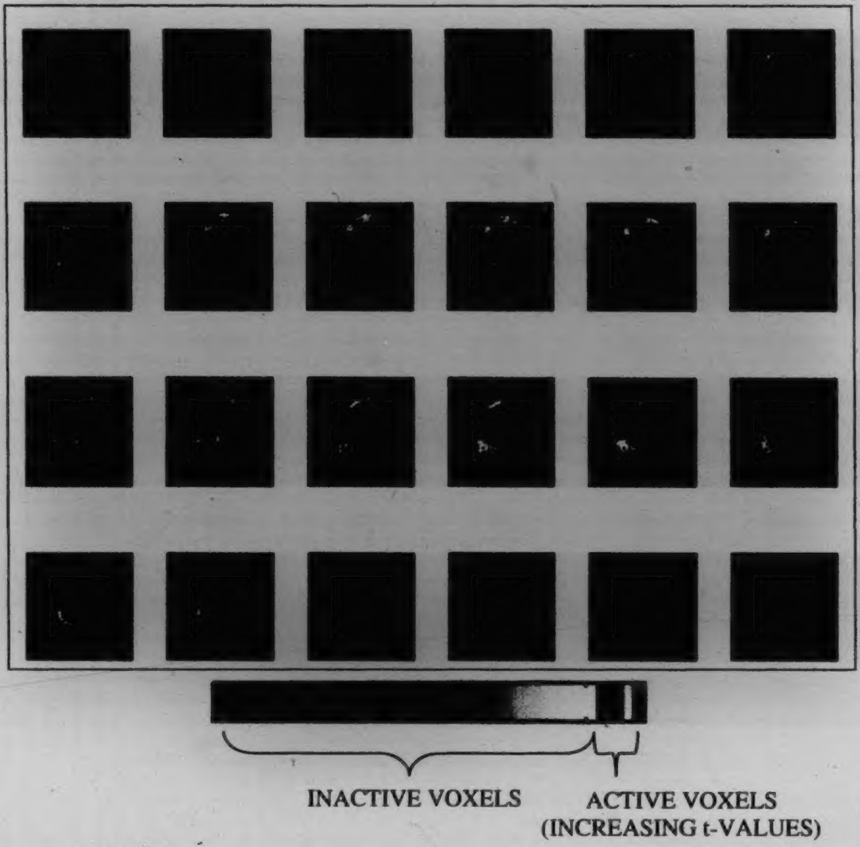
INACTIVE VOXELS
ACTIVE VOXELS
(INCREASING t-VALUES)

Figure 3.43. Brain Map Showing Active Voxels Determined by t-test using Spatio-Temporal ICA-Derived Hemodynamic Response Regressor (Run 3; Images are in Radiological Orientation)

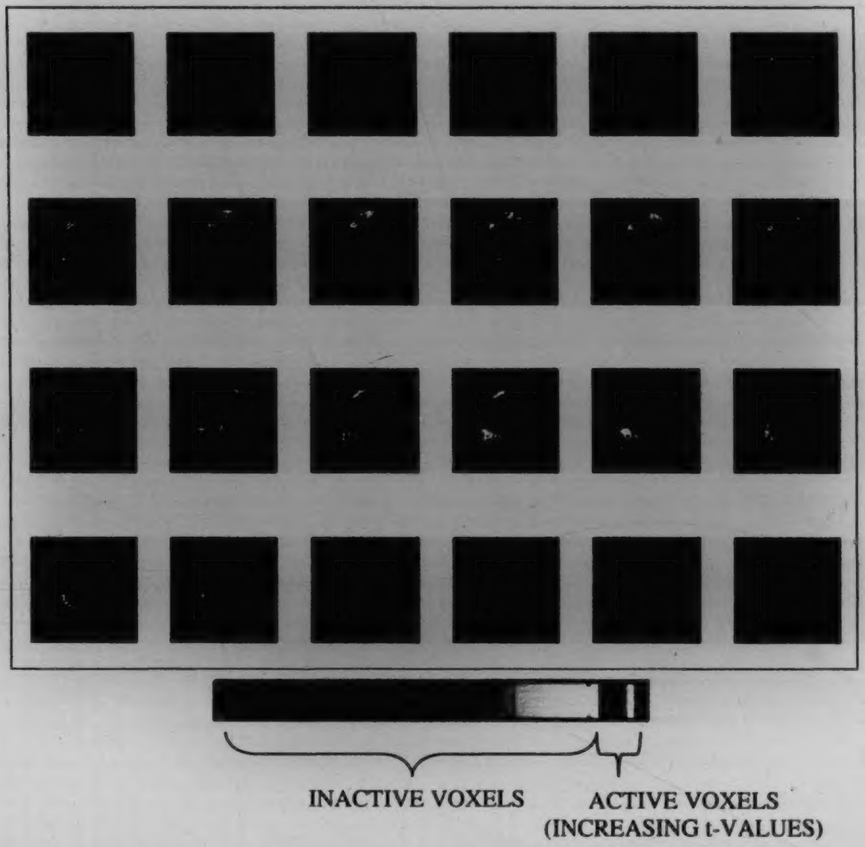

Figure 3.44. Brain Map Showing Active Voxels Determined by t-test using Inverted Canonical Hemodynamic Response Regressor (Run 3; Images are in Radiological Orientation)

The correlation coefficients between the spatio-temporal ICA-derived hemodynamic response regressors and the corresponding inverted canonical hemodynamic response regressors were acquired as another means of comparing the signals. The correlation coefficient between the spatio-temporal ICA-derived hemodynamic response regressor and the inverted canonical response for run 1 is 0.76. The correlation coefficient between the spatio-temporal ICA-derived hemodynamic response regressor and the inverted canonical response for run 2 is 0.93. The correlation coefficient between the spatio-temporal ICA-derived hemodynamic response regressor and the inverted canonical response for run 3 is 0.99. These correlation coefficients are high, but the correlation coefficient for run 1 is much less than the correlation coefficient for each of the other two runs.

3.2.3 HR Model Comparisons

In the final phase of this study, the HR models were compared using various measures and statistics. The voxels that were active according to the t-test results were subjected to the CR, DW statistics and F-statistics calculations. The active voxels that reached the F-statistic threshold were used for the R_a^2 calculations. First, the total number of voxels that were analyzed and the number of active voxels found using each HR model for each run are listed in Table 3.3. Next, the CRs that compare the active voxel locations between the spatio-temporal ICA-derived response brain maps and the canonical response brain maps are 0.0 %. Thus, there is no active voxel overlap. The CRs that compare the active voxel locations between the inverted canonical response brain maps and the canonical response brain maps are also 0.0 %. The CR that compares the active voxel locations between the spatio-temporal ICA-derived response brain map and the inverted canonical response brain map is 71.5 % for run 1, 89.9 % for run 2 and 98.6 % for run 3. The ranges, means and standard deviations of the sets of active voxel t-values and the sets of active voxel DW statistics are also listed in Table 3.3. The number of active voxels that had a DW p-value (probability of uncorrelated residuals) of at least 0.50 is listed in Table 3.3 as well. The number of active voxels that reached the F-value threshold is also listed in Table 3.3. Finally, the range, mean and standard deviation of the R_a^2 measures for the active voxels that reached the F-value threshold are listed in Table 3.3.

Table 3.3. Comparison of HR Models

Test/ Model	Canonical HR Model			Spatio-Temporal ICA-Derived HR Model			Inverted Canonical HR Model		
Run	1	2	3	1	2	3	1	2	3
Voxels Analyzed	15, 899	16, 059	15, 900	15, 899	16, 059	15, 900	15, 899	16, 059	15, 900
Active Voxels	74	206	61	2, 548	2, 720	2, 956	2, 310	2, 641	2, 956
t-value Range	4.9 – 9.8	4.9 – 14.4	5.0 – 11.0	4.9 – 16.7	4.9 – 21.6	4.9 – 20.8	4.9 – 21.4	4.9 – 26.0	4.9 – 21.2
Mean t	6.2	6.5	6.4	7.4	8.2	8.0	7.9	8.4	8.1
t-value SD	1.6	1.6	1.2	2.0	2.7	2.6	2.5	3.0	2.6
DW p-value Range	0.00 – 0.82	0.00 – 0.91	0.00 – 0.41	0.00 – 0.99	0.00 – 0.99	0.00 – 0.96	0.00 - 0.99	0.00 – 1.00	0.00 - 0.97
Mean DW p	0.045	0.025	0.0083	0.027	0.019	0.0071	0.028	0.019	0.0071
DW p SD	0.16	0.11	0.053	0.12	0.099	0.065	0.12	0.10	0.065
Voxels with DW $p \geq 0.50$	3	4	0	52	42	17	52	42	17
Voxels with $F \geq 1.80$	18	68	18	1, 372	1, 715	1, 756	1, 370	1, 688	1, 770
R_a^2 Range	0.027 – 0.082	0.026 – 0.19	0.026 – 0.11	0.024 – 0.24	0.024 – 0.36	0.025 – 0.34	0.025 - 0.35	0.024 - 0.45	0.025 - 0.35
Mean R_a^2	0.045	0.051	0.043	0.063	0.082	0.079	0.075	0.087	0.080
R_a^2 SD	0.014	0.034	0.021	0.034	0.052	0.049	0.048	0.058	0.050

Chapter 4

Discussion

4.1 Study 1: Block Design Paradigm

The spatial ICA-derived regressors and temporal ICA-derived regressors were compared with each other and with the canonical response regressor in several different ways.

4.1.1 Regressors

The "unaveraged" fMRI data spatial and temporal independent components that are identified as consistently task-related components exhibit several features that indicate the components are related to the motor task. The spatial independent component brain map and the temporal independent component brain map show high spatial weights in regions that are expected to be active during the motor task. Both component maps have high spatial weights in the left hemisphere motor cortex and the supplementary motor cortex. Neural activity that is involved in allowing and controlling movement of the fingers of the right hand takes place in the left hemisphere motor cortex. Hence, it is expected that task-related independent component brain maps acquired from fMRI measurements in which subjects perform finger movement tasks during the scan have high spatial weights in the left hemisphere motor cortex [28, 86]. The supplementary motor cortex is also involved in controlling movement. The spatial component brain map also has high spatial weights in the right cerebellum. Finger movement requires dexterity and fine control, which are aspects of finger movement governed by the ipsilateral cerebellum [86].

The unaveraged fMRI data task-related temporal component time course and the unaveraged fMRI data task-related spatial component ROA+ average time course also indicate that the components are consistently task-related. The correlation coefficients of both independent component time courses with the canonical hemodynamic response are greater than 0.78. The timing of the peaks and troughs in the time courses are concordant with the timing of the task-and-rest cycles. Both time courses look similar to a sinusoid, much like the canonical response does for this experiment.

The amplitudes of the unaveraged fMRI data task-related independent component time courses indicate that the BOLD responses varied in amplitude across trials. Signal increases up to a maximum of about 1% above baseline activity are in the task-related ROA+ average time course of the spatial component (Figure 3.4). This per cent change in signal amplitude is a little low for a task-related BOLD signal that is usually recorded at 3.0 T. Typically, per cent changes in BOLD signal amplitudes of 0.5 - 5% are recorded in fMRI studies [17, 22-24]. Lower per cent changes in BOLD signal amplitudes are recorded at lower static magnetic field strengths (e.g. $B_0 = 1.5$ T). A baseline BOLD signal level was not computed to find the per cent change in the signal amplitude of the temporal component. The baseline BOLD signal has to be computed manually to analyze the temporal ICA results. The work required to determine the baseline BOLD signal did not seem necessary because the amplitude per cent change measurement is not a major result that needs to be found. In addition, the temporal component is similar to the ROA+ average spatial component time course, so the work required to obtain the per cent change in amplitude seems even more unnecessary.

The maximum per cent change in the task-related ROA+ average spatial component time course signal level is lower than the 2.2% average BOLD signal increase that was recorded in a finger tapping study completed in [87]. A comparison is made between this study and the study in [87] to compare typical task-related BOLD response magnitudes acquired in MR scanners with similar static magnetic field strengths. In the study in [87], a 3.0 T scanner was used to record BOLD signals from 6 patients that performed a finger tapping task. The difference in magnitude between the signals from both studies may be attributable to the differences in subjects. Another explanation for the difference in magnitudes between the signals may be that a comparison is being made between an ROA+ average time course signal from one patient and signals that are averaged over several voxels in 6 patients. These signals are derived differently, so a difference in their magnitudes is expected. There may be significantly different amounts of additive noise in the BOLD signals measured in each experiment. The additive noise may have caused the amplitude of the signals to be higher in the experiment performed in [87]. Alternatively, other spatial components that were found in this study may contain task-related BOLD responses or they may contain a significant portion of the additive noise in the fMRI measurements. If more than one spatial component was included in the derivation of a task-related regressor, then the difference in signal magnitudes between the experiments may be decreased. Any differences in the amplitude per cent changes of the task-related temporal independent component from this study and the average BOLD signals measured in [87] may have been caused by the same factors.

The fMRI recordings acquired in this study were averaged over each trial to accomplish some important objectives. First, averaging the measurements improves the SNR. Furthermore, at least one task-related component was identified in temporal ICA and spatial ICA of the unaveraged fMRI measurements, so averaging the fMRI measurements and then performing ICA provides the opportunity to identify independent component time courses that accurately represent the subject's average BOLD response during one trial. When an average task-related BOLD response over one trial is concatenated together in time over the duration of the scan, a signal may be produced that is more appropriate to use as a regressor than the canonical response. Averaging takes the variation of the BOLD response across different trials into account. Averaging also reduces the statistical bias that is present in this study. Using independent component time courses calculated with the unaveraged fMRI data as regressors would introduce a more significant statistical bias when performing statistical tests on parameter estimates [4, 10]. fMRI measurements from one subject must be used in some way to produce subject-specific and brain-region specific hemodynamic responses that will subsequently be used to analyze the same fMRI measurements or different fMRI measurements acquired from the same subject in order to detect active voxels. Thus, some statistical bias is inevitable.

The spatial and temporal independent components selected from spatial ICA and temporal ICA of the averaged fMRI data, respectively, showed similarities between the corresponding components from spatial ICA and temporal ICA of the unaveraged fMRI data. Spatial component brain maps acquired using either the averaged or unaveraged fMRI data showed high spatial weights in the left hemisphere motor cortex, the supplementary motor cortex and the right side of the cerebellum. The brain maps of the averaged fMRI data temporal component and the unaveraged fMRI data temporal component were nearly identical. The averaged fMRI data temporal component time course and the ROA+ average time course from the averaged fMRI data spatial independent component were similar in shape to one cycle of the corresponding unaveraged fMRI data independent component time courses.

The averaged fMRI data spatial component did show some differences from the corresponding unaveraged fMRI data spatial component. There were a few more regions with high spatial weights in the averaged fMRI data task-related spatial component brain map than in the unaveraged fMRI data task-related spatial component brain map. These regions include areas in the parietal and occipital lobes. The extra regions of high spatial weights may be present because there may be task-related BOLD signal contributions from these regions that become more prominent when the fMRI measurements are averaged together. With regard to the high spatial weights in the occipital lobe, the region of the brain that is involved in processing visual information is located in the occipital lobe [86]. The subject viewed a checkerboard during the task periods of the fMRI scan, so some regions of high spatial weights in the occipital lobe are expected.

The averaged fMRI data temporal component time course and the averaged fMRI data spatial component ROA+ average time course showed similarities and differences with respect to a single cycle of the canonical response. First, the correlation coefficients between the averaged fMRI data independent component time courses and a single cycle of the canonical response were above 0.86, which means all three signals are very similar in shape. However, the spatial component ROA+ average time course reached its peak earlier and it has lower values during the subject's rest period than a single cycle of the canonical response. The temporal component also peaked earlier than both the single cycle canonical response and the spatial component ROA+ average time course. The temporal component also had a sharper peak than the single trial canonical response.

The differences the averaged fMRI data independent component time courses showed with respect to a single cycle of the canonical response may be very important when statistical tests are performed on fMRI measurements. The independent component time courses are subject-specific and brain region-specific. Voxels that are truly active during the task period according to the t-tests done using the independent component regressors may otherwise be labeled inactive if the canonical response is used instead. Voxels that are falsely labeled inactive may be involved in the motor task; these voxels may have important clinical or research implications. Thus, using an assumed hemodynamic response regressor, like the canonical response, in a GLM for statistical analysis of a subject's fMRI measurements when the regressor is not specific to the subject may not yield an accurate assessment of the active regions in the subject's brain [4, 5, 10, 16, 52, 56]. The unaveraged fMRI data independent component time courses varied in shape and amplitude; these variations may not have been taken into account properly by the canonical hemodynamic response regressor. This could result in false positive and/or false negative activations.

4.1.2 Activation Maps

The brain activation maps that show the t-test results from each statistical analysis of the fMRI measurements present some interesting findings. The activation map derived from the t-test using the canonical HR model showed the fewest number of activations. In all three brain activation maps, the highest t-values were in the left motor cortex region. In addition, there were extensive areas of activation in the cerebellum, bilateral regions of the posterior frontal lobe, parietal lobe, temporal lobes and in the supplementary motor cortex. The task-related spatial independent component brain maps and the task-related temporal independent component brain maps (calculated using both the original and averaged fMRI data) had high spatial weights in most of the same regions as the activation maps.

The substantial degree of overlap between the active regions of all three activation maps yielded the high CRs between each pair of activation maps. The activation maps from the t-tests using the ICA-derived HR models were the most similar as the CR between these two maps was the highest by a substantial margin. Only a few areas of activation were unique to the ICA-derived HR model brain maps. Many of the active regions found in this study were also considered active in fMRI studies done in [28] and [87]. The fMRI measurements from the study done in [28] were examined with ICA only.

Despite the large amount of overlap between the active voxels in the brain maps, using the ICA-derived regressors for the t-tests resulted in higher active voxel t-values, on average, than the active voxel t-values found from the t-test in which the canonical response regressor was used. The active regions of the ICA-derived regressor brain maps also covered a larger portion of the brain. The active regions in the spatial and temporal ICA-derived regressor brain maps that were not active in the canonical regressor brain maps were largely in agreement. These regions included parts of the cerebellum and regions near the thalamus and putamen [28]. These regions were also active in the study in [28]. The regions that were active according to the ICA-derived HR model t-tests only were identified because the ICA-derived regressors more accurately represent the subject's task-related BOLD responses than the canonical response regressor. The active regions that were unique to the ICA-derived regressor brain maps may be important in finger tapping task performance. Furthermore, the appearance of unique active regions illustrates that using canonical HR models to perform statistical tests may not be ideal.

4.1.3 Performance of the HR Models

The DW statistics, F-statistics and R_a^2 values that were calculated using the t-test results yielded some interesting findings. These variables provided information to compare the HR models directly.

First, DW statistics were calculated for the active voxels from each t-test. The average DW p-value for active voxels in each of the t-tests was about 0.02, which is very low. Since BOLD signals exhibit a significant amount of autocorrelation due to the way they are measured and preprocessed and the AR(1) model was not used to compensate for the autocorrelation between residuals, it is difficult to pinpoint an acceptable DW threshold p-value that can be used to determine if an HR model is valid at a particular voxel. However, the DW p-values calculated from the ICA-derived HR model t-test results showed higher p-values, on average, than the DW p-values calculated from the canonical HR model t-test results. The number of active voxels that had a probability of having statistically independent errors of at least 50% in the ICA-derived HR model brain maps was larger than the same measurement for the canonical HR model brain map

(Table 3.1). Therefore, the ICA-derived HR models showed improved validity over the canonical HR model. The high degree of correlation among the residuals indicates that there may be several phenomena in the fMRI measurements that are not being adequately accounted for by the HR models [48].

The F-statistic and R_a^2 measures were also useful indicators of the quality of the HR models. First, the F-statistics indicated that each HR model accounted for a statistically significant amount of variance in the BOLD signals measured from active voxels. As for the R_a^2 values, an average of 32 % of the variance of the active voxel BOLD signals was accounted for by the canonical HR model. The ICA-derived models showed slight improvements as they both accounted for an average of 36% of the variance of the active voxel BOLD responses. These somewhat low average values are another indication that some important effects that are present in the BOLD signals are not being accounted for properly. The R_a^2 calculation results indicate that the ICA-derived HR models are a more accurate representation of the BOLD responses in voxels that are active during a finger tapping task.

With regard to the voxels that were active according to the ICA-derived HR model t-tests only, the SNR may not be adequate for the same voxels to be labeled active when a canonical HR model is used for the t-test [5]. Voxels that are falsely labeled inactive may be important in the neural processing required to allow subjects to move their fingers. Conversely, voxels that are falsely labeled active may be misleading when results from motor control fMRI studies are examined.

4.2 Study 2: Event-Related Paradigm

The spatio-temporal ICA-derived regressors were compared with each other and with the canonical response regressor in several different ways.

4.2.1 Regressors

By combining methods in [35, 51, 83] to select interictal event-related independent components, the spatio-temporal components that were chosen show they are related to the interictal events. First, the spatial independent components have high spatial weights in the right temporal lobe, which is the region of the brain that is suspected of causing the patient's seizures. Electrodes placed over the right temporal lobe area recorded interictal epileptic events, so there is spatial agreement between the EEG and ICA findings. In addition, the spatial component time courses and the temporal components show significant BOLD signal changes that are concordant with the onset of interictal events. The magnitudes of the BOLD responses (in the independent component time courses) following interictal events are roughly proportional to the number of interictal events that occurred during a short time period preceding the BOLD responses (Figure 3.18, Figure 3.19 and Figure 3.20).

The interictal event-related BOLD responses in the chosen spatio-temporal components were negative. Negative BOLD responses have been examined in recent studies, but positive BOLD responses have received far more attention because they are more common in all types of fMRI studies [25]. Negative BOLD responses have been reported in studies completed in [10, 25, 26, 88] where the majority of patients showed both positive and negative or only negative BOLD responses to interictal epileptiform events [10, 25, 26]. An interesting finding mentioned in [88] is that there were a lot of negative BOLD responses measured from patients suffering from temporal lobe epilepsy. The findings in this study are consistent with the findings reported in [88].

Positive BOLD responses are expected to occur more often than negative responses [25]. If event-related positive BOLD responses are expected and event-related negative BOLD responses occur, then using the canonical response in an HR model to detect event-related BOLD responses may yield results that are not ideal. Many important active voxels could go undetected and/or many voxels may be falsely labeled active. A significant advantage of ICA is that it is useful if little is known or little can be assumed about a patient's BOLD response [51]. ICA may be used to reveal the shape of a patient's BOLD response. Thus, ICA may prevent erroneous assumptions from being made about patient BOLD responses.

Some attempts have been made to explain the physiology of a negative BOLD response. Since positive BOLD responses have been studied more than negative BOLD responses, the physiological nature of positive BOLD responses is better understood [25]. One proposed explanation of the physiology of a negative BOLD response is that the neural activity preceding the response is inhibitory. There is some evidence that inhibitory neural events require a lot less energy than positive BOLD responses, so there is little need for an increase in blood flow and blood volume to the affected brain area. Hence, the proportion of deoxyhemoglobin increases in regions near the site of neural activity, causing the BOLD response to decrease.

Wiener filtering and smoothing with a Hamming window were useful for deriving spatio-temporal ICA-derived impulse responses. By manipulating the constant term

$S_{vv}(f)/S_{hh}(f)$ in the denominator of equation (2.34)(a), a reasonable low-pass Wiener filter was generated. The Wiener filter is reasonable because when it is multiplied by the frequency spectra of the zeroed spatio-temporal independent components, the resulting frequency spectra of the spatio-temporal ICA-derived impulse responses contain frequency components in a similar band of frequencies as the pass band of the frequency spectrum of the canonical impulse response. A precise frequency spectrum of the patient's interictal event-related hemodynamic impulse response is not known, so the canonical impulse response frequency spectrum is an appropriate guide. A large Hamming window was used for smoothing in order to dampen the oscillations to amplitudes of 0 at approximately 30 seconds. Since little is known about the duration of the interictal event-related impulse response, a 30-second impulse response seems appropriate. The canonical impulse response used in SPM5 lasts approximately 30 seconds and this impulse response was derived using fMRI measurements in a past study [40]. The spatio-temporal ICA-derived impulse responses calculated in this study using Wiener filtering and Hamming window smoothing may contain irrelevant hemodynamic activity (i.e. be too long) or may not capture the entire BOLD response to a single interictal event (i.e. be too short). However, most of the important hemodynamic activity following interictal events is present in the spatio-temporal ICA-derived impulse responses.

An initial transient BOLD signal increase was observed in all three spatio-temporal ICA-derived impulse responses. The transient signal increase in the spatio-temporal ICA-derived impulse response from run 3 was substantially smaller than the same transient signal increases in the spatio-temporal ICA-derived impulse responses in runs 1 and 2. Perhaps the impulse response signals increase for a short time after interictal events because fMRI signal samples considered in the deconvolution process were acquired too soon after the interictal event. Alternatively, some of the interictal events may not have caused a BOLD response, but hemodynamic activity that followed shortly after these interictal events was still involved in the deconvolution process. Perhaps the transient signal increases may not be caused by errors in the impulse response derivation process at all. The transient signal increases may indeed be a part of the patient's interictal event-related BOLD hemodynamic impulse responses. Initial small amplitude signal dips are present in many positive BOLD responses that have been measured from past studies [32, 40]. Small amplitude dips occur so often in positive BOLD responses that they have been modeled in regressors too. Thus, transient amplitude increases may be valid in negative BOLD responses.

The periods of time that elapsed before the spatio-temporal ICA-derived impulse responses from runs 2 and 3 reached their negative peaks fell in the range of 5-8 s. This is the range of time it takes for a positive BOLD response to reach its peak as mentioned in Section 1.2.2.2.2 [17]. The time elapsed before the spatio-temporal ICA-derived impulse response from run 1 reaches its most negative peak is somewhat higher. Coincidentally, the duration of the initial transient positive BOLD signal increase is the longest for the impulse response from run 1. The reason for the difference in durations is not known. However, the differences may be attributed to the inclusion of too much or too little interictal event-related hemodynamic activity in the deconvolution process in run 1 or runs 2 and 3.

The smoothing procedure resulted in three spatio-temporal ICA-derived impulse response frequency spectra that are smooth in appearance just like the canonical impulse response frequency spectrum. The pass bands in all of the impulse response frequency spectra were similar to one another.

Despite some noticeable differences, the shapes of each of the spatio-temporal ICA-derived impulse responses are similar. Hence, the patient had interictal event-related BOLD responses that showed some consistency. Furthermore, when each spatio-temporal ICA-derived impulse response is convolved with its respective pulse train event signal, the resulting hemodynamic response signal is very similar in timing and shape to the corresponding spatio-temporal component during short time periods that followed interictal events. This also suggests that the patient's BOLD responses to interictal events were somewhat consistent. Thus, the hemodynamic response signals that were produced from the convolution process can be used as regressors in GLMs for statistical testing of the fMRI measurements.

Lastly, the comparisons between the spatio-temporal ICA-derived hemodynamic response, the canonical hemodynamic response and the inverted canonical hemodynamic response (from the same run) yielded interesting findings. The spatio-temporal ICA-derived responses and the canonical responses are very different. Hence, if the patient's BOLD responses were not examined first and the canonical response was used as the assumed hemodynamic response for each run, the resulting active voxel locations acquired in this study are likely incorrect. Since the spatio-temporal ICA-derived responses and the canonical responses are very different, the resulting activation maps are very different (discussed in the next two sections). The inverted canonical responses and the spatio-temporal ICA-derived responses, however, are very similar according to the high correlation coefficients between the signals. The correlation coefficient between the spatio-temporal ICA-derived response and the inverted canonical response for run 1 is the lowest, but the signals are still moderately similar. The reason for the difference is likely attributed to the significant transient positive BOLD signal increase that is present in the spatio-temporal ICA-derived response and absent in the inverted canonical response. On the other hand, the spatio-temporal ICA-derived responses and the inverted canonical responses from runs 2 and 3 are very similar. The differences between each of the responses, whether they are small or large, may lead to differences in active voxel locations that have important clinical and research implications.

4.2.2 Activation Maps

Since the spatio-temporal ICA-derived hemodynamic response and the positive canonical response in each run are very different, the t-tests resulted in brain maps that have very different active voxel locations. First, brain maps corresponding to the spatio-temporal ICA-derived response (spatio-temporal ICA-derived response brain maps) have a much higher number of active voxels than the brain maps corresponding to the canonical response (canonical response brain maps). Most of the active voxels in the spatio-temporal ICA-derived response brain maps are in the right hemisphere temporal lobe, which agrees with the spatial ICA brain maps and the EEG recordings. To a lesser extent, some left hemisphere temporal lobe activations are present, which also agrees with the spatial ICA brain maps. However, the spatio-temporal ICA-derived response brain maps also yield strong activations in the right hemisphere frontal lobe, cerebellum and activations that extend upward into the right parietal and right occipital lobes. It is not known why these regions were active during the scan. However, the results suggest that each of these regions may also be involved in generating interictal epileptiform activity. The active voxels in the canonical response brain maps are somewhat inconsistent from run to run. Active voxels in the canonical response brain maps are in the right hemisphere anterior temporal lobe and right hemisphere parietal lobe. None of the canonical response brain map active voxel locations matched the spatio-temporal ICA-derived response brain map active voxel locations. Yet, in some cases, regions of active voxels in the spatio-temporal ICA-derived response brain maps and canonical response brain maps are adjacent.

There are other important discrepancies between the spatio-temporal ICA-derived response brain maps and the canonical response brain maps. The average t-values in the active voxels of the spatio-temporal ICA-derived response brain maps are slightly higher than the t-values in the active voxels of the canonical response brain maps. Since there are not many active voxels in the canonical response brain maps, the average t-value may not be an adequate way of comparing the two brain maps. However, the maximum t-values in the active voxels of the spatio-temporal ICA-derived response brain maps are much higher than the maximum t-values in the active voxels of the canonical response brain maps. Thus, voxels have a higher probability of being active under the assumption that the task-related regressor is the spatio-temporal ICA-derived response regressor rather than the canonical response regressor.

On the other hand, the spatio-temporal ICA-derived response brain maps and the inverted canonical response brain maps from corresponding runs have very similar active voxel locations. The increased CRs between the activation maps coincide with increased correlation coefficients between the spatio-temporal ICA-derived responses and inverted canonical responses. The mean and maximum active voxel t-values from the inverted canonical response brain maps are a little higher than the same measurements from the spatio-temporal ICA-derived brain maps. However, the differences between the t-values of these activation maps are not remarkable.

The results provide evidence that a patient-specific HR model like the spatio-temporal ICA-derived HR model allows the statistical analysis to be more sensitive to detecting active areas where the SNR is low. These findings suggest that care must be taken to choose a proper HR model in similar fMRI studies. Even though the inverted canonical response brain maps and the spatio-temporal ICA-derived response brain maps are very similar, the differences in active voxel locations may be significant in fMRI studies. Precise details about the locations of neural activity in the brain are important when patients are being considered for surgery. If the patient's fMRI measurements were not examined prior to choosing an interictal event-related hemodynamic response regressor, an improper interictal event-related hemodynamic response regressor may have been chosen. An improper hemodynamic response regressor would result in activation maps that are not optimal. An HR model must be prudently chosen to accurately locate brain regions involved in generating epileptic activity. This idea can be extended to any fMRI study such as sensorimotor studies where variable BOLD responses have been found [16]. ICA is a tool that can be used to help develop improved HR models.

4.2.3 Performance of the HR Models

The DW statistics, F-statistics and R_a^2 values that were calculated resulted in some interesting findings.

The mean DW statistics that were calculated to measure residual autocorrelation between the residuals indicate that all HR models have very low validity at the active voxels. The mean DW p-values corresponding to the active voxels in their respective brain maps range from approximately 0-0.05. A very small number of active voxels from all of the brain maps have DW p-values of at least 0.50. The high probability of autocorrelation between residuals indicates that the HR models are not accounting for some important hemodynamic activity that is present in the BOLD signals. Much like the first study, the AR(1) model was not used to account for the autocorrelation between the residuals in this study. Since the AR(1) model was not used and BOLD signal samples exhibit a significant amount of autocorrelation due to the way they are measured and preprocessed, it is difficult to determine an acceptable DW threshold p-value that can be used to decide if an HR model is valid at a particular voxel.

Regarding the differences in the DW p-values between brain maps, the average DW p-values calculated from the canonical HR model t-test results are higher than the average DW p-values calculated from the spatio-temporal ICA-derived HR model t-test results. However, there are very few active voxels in the canonical model brain maps, so the difference in average DW p-values between the different brain maps may not be significant. In contrast to the average DW p-values, the spatio-temporal ICA-derived response brain maps and the inverted canonical response brain maps have higher maximum DW p-values than the canonical response brain maps in corresponding runs.

This result, when combined with the observation that most of the active voxels in the spatio-temporal ICA-derived response brain maps are in the expected regions (right hemisphere temporal lobe), provides evidence that the spatio-temporal ICA-derived HR model shows improved validity over the canonical HR model. There is very little difference in validity between the inverted canonical HR model and the spatio-temporal ICA-derived HR model.

The F-tests revealed interesting results. In all cases, the BOLD signal variance from 36 % or more of the active voxels is not statistically significantly accounted for by the HR models. These results are significantly different from the results found in the first study. In Study 1, all HR models surpassed the F-value threshold at their respective active voxels. These findings allude to the point made earlier that the HR models are not accounting for some important hemodynamic activity that is present in the BOLD signals, especially in this interictal event-related study.

Despite the low DW p-values and the F-test results, the spatio-temporal ICA-derived HR models showed a better fit to their active voxel BOLD signals than did the canonical HR models. The R_a^2 values calculated using the spatio-temporal ICA-derived HR model t-test results are much higher than the R_a^2 values calculated using the canonical HR model t-test results. The R_a^2 values for the spatio-temporal ICA-derived HR models are still low, ranging from maximum values of 0.24-0.34. The ICA-derived HR models are patient-specific and brain region-specific, therefore, they are more likely to yield accurate active voxel locations when used in a statistical test.

The maximum R_a^2 values for the inverted canonical HR models (0.35–0.45) are somewhat higher than the maximum R_a^2 values for the spatio-temporal ICA-derived HR models, but the inverted canonical HR models still do not account for a substantial amount of variance in the BOLD signals.

To account for an increased amount of variance in the BOLD signals, perhaps a spatio-temporal ICA-derived HR model should be used in the GLM in combination with the AR(1) model. Alternatively, multiple spatio-temporal component time courses may be used in the HR model to account for several different phenomena that are present in the BOLD signals. Care must be taken not to use too many spatio-temporal components as regressors with this approach because there may not be enough degrees-of-freedom left to perform a proper t-test.

Chapter 5

Conclusions and Future Work

5.1 Conclusions from Studies 1 and 2

Developing an appropriate hemodynamic response to use as a task-related or stimulus-related regressor in the GLM for a statistical test on fMRI data is a complicated task. Assuming a subject's (or patient's) task-related or stimulus-related BOLD responses will be similar to the canonical response may not yield optimal results. If task-related or stimulus-related BOLD responses are different than the assumed response, false positives and false negatives may result. False positives and false negatives can lead to incorrect conclusions about the nature of a patient's neural and hemodynamic activity.

There is evidence in the two studies of this work that ICA can be used to produce patient-specific and brain-region specific hemodynamic responses that can be modified to make regressors to use in the GLM. The ICA-derived hemodynamic responses take the unique shape of each subject's task-related or stimulus-related BOLD responses into account. The similarities and differences between ICA and the statistical analysis of fMRI measurements using the GLM allow the methods to be combined successfully.

In the right handed finger tapping block design paradigm motor study, time courses were produced using spatial ICA and temporal ICA separately. These time courses were used as regressors in the GLM for a t-test on the fMRI measurements. The largest regions of active voxels that were found from the t-tests using the ICA-derived regressors are in the left hemisphere motor cortex, supplementary motor cortex and ipsilateral cerebellum. All of these regions are involved in processing neural information related to finger movement. Compared to the canonical HR model, the ICA-derived HR models are more valid and they account for a higher amount of variance in the BOLD signal measurements. Despite these differences, the locations of active voxels in all of the brain maps are mostly in agreement.

In the interictal event-related paradigm study, spatial ICA and temporal ICA were combined to produce spatio-temporal ICA-derived interictal event-related hemodynamic impulse responses. After the spatio-temporal ICA-derived hemodynamic impulse responses were filtered and smoothed in the frequency domain, they were convolved with their respective stimulus functions (interictal event pulse train signals) to produce spatio-temporal ICA-derived regressors. Large regions of active voxels were found from the t-tests using the spatio-temporal ICA-derived regressors. These regions are in the right temporal lobe, which agrees with the patient's EEG and the patient's diagnosis of refractory right temporal lobe epilepsy. The spatio-temporal ICA-derived response brain maps show far more active voxels in the expected locations than the canonical response brain maps. The canonical response brain maps are not very useful, because there are very few small active regions. It can be concluded that the canonical hemodynamic response is not an appropriate interictal event-related regressor to use for this study.

Since the fMRI measurements in Study 2 were examined with ICA before statistical tests were performed, the ICA results showed that the patient had negative interictal event-related BOLD responses. Negative interictal event-related BOLD responses have been recorded in patients suffering from temporal lobe epilepsy in past studies [5, 25, 88]. Since negative BOLD responses were observed, the values of the canonical response were multiplied by -1 (inverted) to produce a third event-related regressor to use in another t-test. The inverted canonical HR models and the spatio-temporal ICA-derived HR models are similar in terms of the number of active voxels in their respective brain maps, validity and goodness-of-fit to the BOLD signals.

Hemodynamic responses that are generated based on a patient's own fMRI measurements are more appropriate signals to use as regressors when performing statistical tests. Patient-specific and brain-region specific regressors allow the statistical tests to be more sensitive to the detection of active voxels. Active voxels in which the SNR is low are more easily detected using patient-specific and brain-region-specific regressors [5]. Thus, more accurate brain maps may be produced for researchers and physicians to use. For instance, when epileptic patients are being considered for surgery, accurate brain maps are required in order to do a proper excision of the brain regions causing seizures.

On the other hand, statistical test results will be biased if a patient's fMRI measurements are used to generate a task-related or stimulus-related regressor which is then used to statistically test the measurements from which the regressor was developed. Attempts were made in both studies to reduce the statistical bias; the fMRI measurements were averaged over each trial in the first study and hemodynamic impulse responses were generated in the second study. Another way to reduce statistical bias and produce useful statistical test results with fMRI measurements would be to acquire many measurements from a single patient over several runs (sessions), use some of the measurements to generate a subject-specific hemodynamic response regressor and then use the regressor in statistical tests on the remaining fMRI measurements.

The validity and goodness-of-fit of all the HR models used in the two studies of this work are not optimal. BOLD signals are acquired at a rapid rate and are extensively preprocessed, so there is a substantial amount of autocorrelation between the signal samples. More work needs to be done to account for the various phenomena that are present in the BOLD signals by using more regressors or other methods.

ICA was shown to be a useful tool for providing insight into the task or stimulus-related BOLD responses of a subject before any assumptions are made about the shape of a subject's BOLD responses. From the ICA results, appropriate task-related and stimulus-related regressors were produced to use in the GLM for a statistical analysis of the fMRI measurements.

5.2 Future Directions

There are several ways to develop the ideas presented in this work. For instance, if ICA is performed on the fMRI measurements, several independent component time courses may be used to develop one or more task-related or stimulus-related hemodynamic responses to use as regressors. Subjects may generate a single task-related or stimulus-related BOLD response that is comprised of more than one independent component. On the other hand, subjects may have several different task-related or stimulus-related BOLD responses that are represented by several independent components. Furthermore, several independent component time courses can be used to produce several regressors to account for several different types of phenomena that are present in the fMRI measurements. For instance, several ICA-derived regressors may be used to account for noise or physiological activity other than task-related or stimulus-related BOLD activity. If more regressors are included, the validity and goodness-of-fit of the HR models may improve. When using ICA, a more systematic method of selecting independent components would be helpful. There was some ambiguity in the component selection in the studies of this work, so more well-defined rules to choose components would be useful.

There is a need for more studies that focus on measuring and improving the quality of HR models. There are not enough studies that focus on obtaining valid HR models that fit the BOLD signals well. A lot of studies measure the quality of an HR model by the number of active voxels that are found when the model is used in a statistical test [48]. This method of assessing HR model quality is not ideal. DW statistics, F-statistics and R_a^2 measures are useful ways of assessing the quality of HR models, but there may be other ways of measuring model quality that would be easier to implement. Most of the DW statistics, F-statistics and R_a^2 measures calculated for the HR models in the studies of this work are not adequate. One change that may improve these calculations is to use ICA-derived hemodynamic responses in combination with AR(1) models when conducting parameter estimations.

Lastly, more work can be done to improve interictal event fMRI studies. For instance, different interictal events that occur in the EEG can be separated by type or the brain region from which the interictal events originate. ICA can be used on the fMRI measurements that are separated according to different interictal event types or locations.

Alternatively, EEG measurements can be used as constraints when performing statistical analyses on fMRI measurements to locate active voxels.

References

[1] M. J. Brodie and S. C. Schachter, *Fast Facts - Epilepsy*. Oxford, UK: Health Press Limited, 1999.

[2] T. R. Browne and G. L. Holmes, *Handbook of Epilepsy*, Third ed. Philadelphia, PA, USA: Lippincott Williams & Wilkins, 2004.

[3] E. Wyllie, A. Gupta, and D. K. Lachhwani, "The Treatment of Epilepsy: Principles & Practice," Fourth ed. Philadelphia, PA, USA: Lippincott Williams & Wilkins, 2006.

[4] J. K. Kang, C.-G. Bénar, A. Al-Asmi, Y. A. Khani, G. B. Pike, F. Dubeau, and J. Gotman, "Using Patient-Specific Hemodynamic Response Functions in Combined EEG-fMRI Studies in Epilepsy," *NeuroImage*, pp. 1162-1170, 2003.

[5] A. P. Bagshaw, Y. Aghakhani, C.-G. Bénar, E. Kobayashi, C. Hawco, F. Dubeau, G. B. Pike, and J. Gotman, "EEG-fMRI of Focal Epileptic Spikes: Analysis with Multiple Haemodynamic Functions and Comparison with Gadolinium-Enhanced MR Angiograms," *Human Brain Mapping*, vol. 22, pp. 179-192, 2004.

[6] J. Baudewig, H. J. Bittermann, W. Paulus, and J. Frahm, "Simultaneous EEG and Functional MRI of Epileptic Activity: a Case Report," *Clinical Neurophysiology*, vol. 112, pp. 1196 -1200, 2001.

[7] S. Ogawa, T.-M. Lee, A. S. Nayak, and P. Glynn, "Oxygenation-Sensitive Contrast in Magnetic Resonance Image of Rodent Brain at High Magnetic Fields," *Magnetic Resonance in Medicine*, vol. 14, pp. 68 - 78, 1990.

[8] J. Hennig, O. Speck, M. A. Koch, and C. Weiller, "Functional Magnetic Resonance Imaging: a Review of Methodological Aspects and Clinical Applications," *Journal of Magnetic Resonance Imaging*, vol. 18, pp. 1 - 15, 2003.

[9] P. M. Matthews, "An Introduction to Functional Magnetic Resonance Imaging of the Brain," in *Functional MRI: An Introduction to Methods*, P. Jezzard, P. M. Matthews, and S. M. Smith, Eds. New York, NY, USA: Oxford University Press, 2001, pp. 3-34.

[10] J. Gotman, C.-G. Bénar, and F. Dubeau, "Combining EEG and fMRI in Epilepsy: Methodological Challenges and Clinical Results," *Journal of Clinical Neurophysiology*, vol. 21, pp. 229-240, 2004.

[11] R. B. Buxton, *Introduction to Functional Magnetic Resonance Imaging: Principles & Techniques*. New York, NY, USA: Cambridge University Press, 2002.

[12] P. Jezzard and S. Clare, "Principles of Nuclear Magnetic Resonance and MRI," in *Functional MRI: An Introduction to Methods*, P. Jezzard, P. M. Matthews, and S. M. Smith, Eds. New York, NY, USA: Oxford University Press, 2001, pp. 67-92.

[13] R. A. Jones, J. A. Brookes, and C. T. W. Moonen, "Ultra-Fast MRI," in *Functional MRI: An Introduction to Methods*, P. Jezzard, P. M. Matthews, and S. M. Smith, Eds. New York, NY, USA: Oxford University Press, 2001.

[14] E. Han, G. Gold, J. Stainsby, G. Wright, C. Beaulieu, and J. Brittain, "In Vivo T1 and T2 Measurements of Musculoskeletal Tissue at 3T and 1.5T," presented at 11th Annual Meeting of the International Society of Magnetic Resonance in Medicine, Toronto, ON, Canada, 2003.

[15] K. Friston, "Introduction: Experimental Design and Statistical Parametric Mapping," in *Human Brain Function, Second Edition*, J. Ashburner, K. Friston, and W. Penny, Eds., Second ed. San Diego, CA, USA: Academic Press, 2003.

[16] G. K. Aguirre, E. Zarahn, and M. D'Esposito, "The Variability of Human BOLD Hemodynamic Responses," *NeuroImage*, vol. 8, pp. 360-369, 1998.

[17] R. D. Hoge and G. B. Pike, "Quantitative Measurement Using fMRI," in *Functional MRI: An Introduction to Methods*, P. Jezzard, P. M. Matthews, and S. M. Smith, Eds. New York, NY, USA: Oxford University Press, 2001, pp. 159-174.

[18] J. J. Pekar, "A Brief Introduction to Functional MRI: History and Today's Developments," in *IEEE Engineering in Medicine and Biology*, vol. 25, 2006, pp. 24-26.

[19] R. S. Menon and B. G. Goodyear, "Spatial and Temporal Resolution in fMRI," in *Functional MRI: An Introduction to Methods*, P. Jezzard, P. M. Matthews, and S. M. Smith, Eds. New York, NY, USA: Oxford University Press, 2001, pp. 145-158.

[20] S. C. Strother, "Evaluating fMRI Preprocessing Pipelines," in *IEEE Engineering in Medicine and Biology*, vol. 25, 2006, pp. 27-41.

[21] J. Ashburner, G. Flandin, R. Henson, S. Kiebel, J. Kilner, J. Mattout, W. Penny, K. E. Stephan, and C. Hutton, "SPM5 Manual," London, UK 2005.

[22] V. Della-Maggiore, W. Chau, P. R. Peres-Neto, and A. R. McIntosh, "An Empirical Comparison of SPM Preprocessing Parameters to the Analysis of fMRI Data," *NeuroImage*, vol. 17, pp. 19-28, 2002.

[23] L. Lemieux, A. Salek-Haddadi, and K. Krakow, "The Nature of MR Signal Changes (letter)," *Radiology*, vol. 226, pp. 922-923, 2003.

[24] P. A. Bandettini, "Selection of the Optimal Pulse Sequence for Functional MRI," in *Functional MRI: An Introduction to Methods*, P. Jezzard, P. M. Matthews, and S. M. Smith, Eds. New York, NY, USA: Oxford University Press, 2001, pp. 123-143.

[25] E. Kobayashi, A. P. Bagshaw, C. Grova, F. Dubeau, and J. Gotman, "Negative BOLD Responses to Epileptic Spikes," *Human Brain Mapping*, vol. 27, pp. 488-497, 2006.

[26] C.-G. Bénar, C. Grova, E. Kobayashi, A. P. Bagshaw, Y. Aghakhani, F. Dubeau, and J. Gotman, "EEG-fMRI of Epileptic Spikes: Concordance with EEG Source Localization and Intracranial EEG," *NeuroImage*, vol. 30, pp. 1161-1170, 2006.

[27] K. J. Friston, P. Fletcher, O. Josephs, A. Holmes, M. D. Rugg, and R. Turner, "Event-Related fMRI: Characterizing Differential Responses," *NeuroImage*, vol. 7, pp. 30-40, 1998.

[28] C. H. Moritz, V. M. Haughton, D. Cordes, M. Quigley, and M. E. Meyerand, "Whole-Brain Functional MR Imaging Activation from a Finger-Tapping Task Examined with Independent Component Analysis," *American Journal of Neuroradiology*, vol. 21, pp. 1629-1635, 2000.

[29] D. L. Donaldson and R. L. Buckner, "Effective Paradigm Design," in *Functional MRI: An Introduction to Methods*, P. Jezzard, P. M. Matthews, and S. M. Smith, Eds. New York, NY, USA: Oxford University Press, 2001, pp. 177-195.

[30] S. M. Smith, "Overview of fMRI Analysis," in *Functional MRI: An Introduction to Methods*, P. Jezzard, P. M. Matthews, and S. M. Smith, Eds. New York, NY, USA: Oxford University Press, 2001, pp. 215-227.

[31] C. Mulert, L. Jäger, R. Schmitt, P. Bussfeld, O. Pogarell, H.-J. Möller, G. Juckel, and U. Hegerl, "Integration of fMRI and Simultaneous EEG: Towards a Comprehensive Understanding of Localization and Time-Course of Brain Activity in Target Detection," *NeuroImage*, vol. 22, pp. 83-94, 2004.

[32] R. Henson, "Analysis of fMRI Time Series: Linear Time-Invariant Models, Event-Related fMRI and Optimal Experimental Design," in *Human Brain Function, Second Edition*, J. Ashburner, K. Friston, and W. Penny, Eds., Second ed. San Diego, CA, USA: Academic Press, 2003.

[33] J. A. Mumford and T. E. Nichols, "Modeling and Inference of Multisubject fMRI Data," in *IEEE Engineering in Medicine and Biology*, vol. 25, 2006, pp. 42-51.

[34] K. E. Stephan, L. M. Harrison, W. Penny, and K. J. Friston, "Biophysical Models of fMRI Responses," *Current Opinion in Neurobiology*, vol. 14, pp. 629-635, 2004.

[35] M. J. McKeown, S. Makeig, G. G. Brown, T.-P. Jung, S. S. Kindermann, A. J. Bell, and T. J. Sejnowski, "Analysis of fMRI Data by Blind Separation into Independent Spatial Components," *Human Brain Mapping*, vol. 6, pp. 160-188, 1998.

[36] K. J. Worsley, C. H. Liao, J. Aston, V. Petre, G. H. Duncan, F. Morales, and A. C. Evans, "A General Statistical Analysis for fMRI Data," *NeuroImage*, vol. 15, pp. 1-15, 2002.

[37] C. Büchel, A. P. Holmes, G. Rees, and K. J. Friston, "Characterizing Stimulus-Response Functions Using Nonlinear Regressors in Parametric fMRI Experiments," *NeuroImage*, vol. 8, pp. 140-148, 1998.

[38] K. Hamandi, A. Salek-Haddadi, D. R. Fish, and L. Lemieux, "EEG/Functional MRI in Epilepsy: The Queen Square Experience," *Journal of Clinical Neurophysiology*, vol. 21, pp. 241-248, 2004.

[39] B. Bai and P. Kantor, "A Shape-Based Finite Impulse Response Model for Functional Brain Images," in *IEEE International Symposium on Biomedical Imaging*. Washington, DC, USA, 2007, pp. 1-4.

[40] K. J. Friston, O. Josephs, G. Rees, and R. Turner, "Nonlinear Event-Related Responses in fMRI," *Magnetic Resonance in Medicine*, vol. 39, pp. 41-52, 1998.

[41] R. A. Adams, *Calculus: A Complete Course*, Third ed. Don Mills, ON, Canada: Addison-Wesley Publishers Limited, 1995.

[43] T. E. Lund, K. H. Madsen, K. Sidaros, W.-L. Luo, and T. E. Nichols, "Non-White Noise in fMRI: Does Modelling Have an Impact?," *NeuroImage*, vol. 29, pp. 54-66, 2006.

[44] K. J. Friston, S. Williams, R. Howard, R. S. J. Frackowiak, and R. Turner, "Movement-Related Effects in fMRI Time-Series," *Magnetic Resonance in Medicine*, vol. 35, pp. 346-355, 1996.

[45] J.-B. Poline, F. Kherif, and W. Penny, "Contrasts and Classical Inference," in *Human Brain Function, Second Edition*, J. Ashburner, K. Friston, and W. Penny, Eds.: Academic Press, 2003.

[46] R. E. Kirk, *Elementary Statistics*, Second ed. Belmont, CA, USA: Brooks/Cole Publishing Company, 1984.

[47] K. J. Worsley, "Statistical Analysis of Activation Images," in *Functional MRI: An Introduction to Methods*, P. Jezzard, P. M. Matthews, and S. M. Smith, Eds. New York, NY, USA: Oxford University Press, 2001, pp. 251-270.

[48] M. Razavi, T. J. Grabowski, W. P. Vispoel, P. Monahan, S. Mehta, B. Eaton, and L. Bolinger, "Model Assessment and Model Building in fMRI," *Human Brain Mapping*, vol. 20, pp. 227-238, 2003.

[49] A. Hyvärinen and E. Oja, "Independent Component Analysis: Algorithms and Applications," *Neural Networks*, vol. 13, pp. 411-430, 2000.

[50] A. Hyvärinen, "Survey on Independent Component Analysis," *Neural Computing Surveys*, vol. 2, pp. 94-128, 1999.

[51] V. D. Calhoun, T. Adali, G. D. Pearlson, and J. J. Pekar, "Spatial and Temporal Independent Component Analysis of Functional MRI Data Containing a Pair of Task-Related Waveforms," *Human Brain Mapping*, vol. 13, pp. 43-53, 2001.

[52] J.-R. Duann, T.-P. Jung, W.-J. Kuo, T.-C. Yeh, S. Makeig, J.-C. Hsieh, and T. J. Sejnowski, "Single-Trial Variability in Event-Related BOLD Signals," *NeuroImage*, vol. 15, pp. 823-835, 2002.

[53] D. Hu, L. Yan, Y. Liu, Z. Zhou, K. J. Friston, C. Tan, and D. Wu, "Unified SPM-ICA for fMRI Analysis," *NeuroImage*, vol. 25, pp. 746-755, 2005.

[54] M. A. Quigley, V. M. Haughton, J. Carew, D. Cordes, C. H. Moritz, and M. E. Meyerand, "Comparison of Independent Component Analysis and Conventional Hypothesis-Driven Analysis for Clinical Functional MR Image Processing," *American Journal of Neuroradiology*, vol. 23, pp. 49-58, 2002.

[55] Z. J. Koles, "Trends in EEG Source Localization," *Electroencephalography and Clinical Neurophysiology*, vol. 106, pp. 229-240, 1998.

[56] J. C. Rajapakse, F. Kruggel, J. M. Maisog, and D. Y. v. Cramon, "Modeling Hemodynamic Response for Analysis of Functional MRI Time-Series," *Human Brain Mapping*, vol. 6, pp. 283-300, 1998.

[57] R. Henson, M. D. Rugg, and K. J. Friston, "The Choice of Basis Functions in Event-Related fMRI," *NeuroImage*, vol. 13, pp. S149, 2001.

[58] F. Schmitt, M. K. Stehling, and R. Turner, *Echo-Planar Imaging: Theory, Technique and Application*. Berlin, Germany: Springer, 1998.

[59] S. M. Smith, "Preparing fMRI Data for Statistical Analysis," in *Functional MRI: An Introduction to Methods*, P. Jezzard, P. M. Matthews, and S. M. Smith, Eds. New York, NY, USA: Oxford University Press, 2001, pp. 229-241.

[60] M. J. Brammer, "Head Motion and its Correction," in *Functional MRI: An Introduction to Methods*, P. Jezzard, P. M. Matthews, and S. M. Smith, Eds. New York, NY, USA: Oxford University Press, 2001, pp. 243-250.

[61] T. Johnstone, K. S. O. Walsh, L. L. Greischar, A. L. Alexander, A. S. Fox, R. J. Davidson, and T. R. Oakes, "Motion Correction and the Use of Motion Covariates in Multiple-Subject fMRI Analysis," *Human Brain Mapping*, vol. 27, pp. 779-788, 2006.

[62] S. M. Smith, "BET: Brain Extraction Tool," Oxford, UK TR00SMS2b.

[63] M. Brett, W. Penny, and S. Kiebel, "An Introduction to Random Field Theory," in *Human Brain Function, Second Edition*, J. Ashburner, K. Friston, and W. Penny, Eds.: Academic Press, 2003.

[64] K. J. Worsley and K. J. Friston, "Analysis of fMRI Time-Series Revisited - Again," *NeuroImage*, vol. 2, pp. 173-181, 1995.

[65] K. J. Friston, O. Josephs, E. Zarahn, A. P. Holmes, S. Rouquette, and J.-B. Poline, "To Smooth or Not to Smooth? Bias and Efficiency in fMRI Time-Series Analysis," *NeuroImage*, vol. 12, pp. 196-208, 2000.

[66] V. D. Calhoun, T. Adali, L. K. Hansen, J. Larsen, and J. J. Pekar, "ICA of Functional MRI Data: An Overview," presented at 4th International Symposium on Independent Component Analysis and Blind Signal Separation, Nara, Japan, 2003.

[67] K. J. Friston and W. Penny, "Classical and Bayesian Inference," in *Human Brain Function, Second Edition*, J. Ashburner, K. J. Friston, and W. Penny, Eds.: Academic Press, 2003.

[68] J. Diedrichsen and R. Shadmehr, "Detecting and Adjusting for Artifacts in fMRI Time Series Data," *NeuroImage*, vol. 27, pp. 624-634, 2005.

[69] A. C. Harvey, *The Econometric Analysis of Time Series*, Second ed. Hertfordshire, UK: Philip Allan, 1990.

[70] N. E. Savin and K. J. White, "The Durbin-Watson Test for Serial Correlation with Extreme Sample Sizes or Many Regressors," *Econometrica*, vol. 45, pp. 1989-1996, 1977.

[71] K. Krakow, D. Messina, L. Lemieux, J. S. Duncan, and D. R. Fish, "Functional MRI Activation of Individual Interictal Epileptiform Spikes," *NeuroImage*, vol. 13, pp. 502-505, 2001.

[72] C. M. Michel, M. M. Murray, G. Lantz, S. Gonzalez, L. Spinelli, and R. G. d. Peralta, "EEG Source Imaging," *Journal of Clinical Neurophysiology*, vol. 115, pp. 2195-2222, 2004.

[73] G. Srivastava, S. Crottaz-Herbette, K. M. Lau, G. H. Glover, and V. Menon, "ICA-Based Procedures for Removing Ballistocardiogram Artifacts from EEG Data Acquired in the MRI Scanner," *NeuroImage*, vol. 24, pp. 50-60, 2005.

[74] V. D. Calhoun, T. Adali, and G. D. Pearlson, "Independent Component Analysis Applied to fMRI Data: A Generative Model for Validating Results," in *IEEE Signal Processing Society Workshop*. Piscataway, NJ, USA, 2001.

[75] J. V. Stone, *Independent Component Analysis: A Tutorial Introduction*. Cambridge, MA, USA: Bradford Books, 2004.

[76] D. Cordes and R. R. Nandy, "Estimation of the Intrinsic Dimensionality of fMRI Data," *NeuroImage*, vol. 29, pp. 145-154, 2006.

[77] T.-P. Jung, S. Makeig, M. J. McKeown, A. J. Bell, T.-W. Lee, and T. J. Sejnowski, "Imaging Brain Dynamics Using Independent Component Analysis," *Proceedings of the IEEE*, vol. 89, pp. 1107-1122, 2001.

[78] R. E. Ziemer and W. H. Tranter, *Principles of Communications*, Fourth ed. New York, NY, USA: John Wiley & Sons, 1995.

[79] A. J. Bell and T. J. Sejnowski, "An Information Maximisation Approach to Blind Separation and Blind Deconvolution," *Neural Computation*, vol. 7, pp. 1129-1159, 1995.

[80] S. Makeig, "Frequently Asked Questions about ICA applied to EEG and MEG data," Swartz Center for Computational Neuroscience, 2002.

[81] "F Distribution Calculator: Online Statistical Table," Stat Trek.

[82] R. E. Walpole, R. H. Myers, and S. L. Myers, *Probability and Statistics for Engineers and Scientists*, Sixth ed. Upper Saddle River, NJ, USA: Prentice-Hall, 1998.

[83] H. Chen, D. Yao, G. Lu, Z. Zhang, and Q. Hu, "Localization of Latent Epileptic Activities Using Spatio-Temporal Independent Component Analysis of fMRI Data," *Brain Topography*, vol. 19, pp. 21-28, 2006.

[84] P. Valenti, E. Cazamajou, M. Scarpettini, A. Aizemberg, W. Silva, and S. Kochen, "Automatic Detection of Interictal Spikes Using Data Mining Models," *Journal of Neuroscience Methods*, vol. 150, pp. 105-110, 2006.

[85] R. C. Gonzalez and P. Wintz, *Digital Image Processing*, Second ed. Don Mills, ON, Canada: Addison-Wesley Publishing, 1987.

[86] E. P. Widmaier, H. Raff, and K. T. Strang, *Vander, Sherman & Luciano's Human Physiology: The Mechanisms of Body Function*, Ninth ed. New York, NY, USA: McGraw-Hill, 2004.

[87] G. Krüger, A. Kastrup, and G. H. Glover, "Neuroimaging at 1.5 T and 3.0 T: Comparison of Oxygenation-Sensitive Magnetic Resonance Imaging," *Magnetic Resonance in Medicine*, vol. 45, pp. 595-604, 2001.

[88] E. Kobayashi, A. P. Bagshaw, C.-G. Bénar, Y. Aghakhani, F. Andermann, F. Dubeau, and J. Gotman, "Temporal and Extratemporal BOLD Responses to Temporal Lobe Interictal Spikes," *Epilepsia*, vol. 47, pp. 343-354, 2006.